LASER-INDUCED BREAKDOWN SPECTROSCOPY (LIBS) FOR DETECTING

METAL PARTICLES RELEASED FROM ENERGETIC REACTIONS

A Thesis

by

MORGAN PATRICK O'NEIL

Submitted to the Office of Graduate and Professional Studies of
Texas A&M University
in partial fulfillment of the requirements for the degree of

MASTER OF SCIENCE

Chair of Committee,   Waruna Kulatilaka
Committee Members,   Eric Petersen
                        Adonios Karpetis
Head of Department,   Andreas Polycarpou

May 2017

Major Subject: Mechanical Engineering

ABSTRACT

The objective of this work is to characterize emissions from solid propellants using a non-intrusive optical diagnostic method, primarily focusing on the release of the metallic species of aluminum (Al), copper (Cu), lead (Pb), and mercury (Hg) during energetic reactions. The primary motivation for developing such diagnostic methods is that particulate matter released to the air from energetic reactions can cause adverse health effects, such as pulmonary and cardiovascular disease, particulate matter-induced allergy, and cancer. The enabling technology used for this research study is Laser-Induced Breakdown Spectroscopy (LIBS), which is an elemental, analytical technique that uses high-intensity laser pulses to generate a plasma in a medium where the composition is to be detected. Light emitted from this plasma is then collected and dispersed using a spectrometer onto a CCD array. The elemental composition can be determined based on characteristic spectral lines detected and their relative intensities. Two LIBS schemes were used during the current experiments: one using a 10-nanosecond (ns) pulse-duration, 10-Hz repetition-rate, neodymium-doped yttrium aluminum garnet (Nd:YAG) laser and the other using an 80-femtosecond (fs) pulse-duration, 1-kHz repetition-rate, amplified Ti:Sapphire laser system.

Before attempting to detect the metallic species in the gas-phase exhaust region during the combustion of laboratory-scale propellant sticks, initial experiments of laser pulse energy dependence and plasma decay time were performed using solid target plates of Al, Cu and Pb. These initial experiments were conducted to determine the optimum

laser parameters and signal collection conditions. Subsequent experiments were conducted during combustion events of hydroxyl-terminated polybutadiene/ammonium perchlorate (HTPB/AP) propellant samples doped with known quantities of metals. The ns-LIBS scheme was capable of detecting Al LIBS signals corresponding to the samples with predetermined quantities of Al in the 5–16% range by mass. An aluminum metal concentration study was also performed, which showed that a propellant strand with a higher mass percentage of aluminum is more likely to have a LIBS signal until up to a point where the gas-phase reaction zone begins to act like a homogeneous medium. A comparison of LIBS detection between a ns Nd:YAG laser and fs Ti:Sapphire laser was also performed. While the LIBS scheme using the 10-ns, 10-Hz Nd:YAG laser pulses could not detect any other metal species besides aluminum, the 80-fs, 1-kHz Ti:Sapphire laser was able to detect characteristic signals from the metallic additives: aluminum, copper, lead (from the base metal as well as from lead stearate [$(C_{17}H_{35}COO)_2Pb$], a common additive for altering the reaction rate), and mercury chloride (Hg_2Cl_2) at mass percentages in the range of 2–16% by mass in the initial propellant mix.

DEDICATION

I would like to dedicate this work to Ruby for her unconditional love and walks through the park.

ACKNOWLEDGEMENTS

I would like to thank my committee chair, Dr. Waruna Kulatilaka, and my committee members, Dr. Eric Petersen and Dr. Adonios Karpetis, for their guidance and support throughout the course of this research.

Thanks also go to my friends, colleagues, and the department faculty and staff for making my time at Texas A&M University a great experience.

Finally, thanks to my mother and father for their encouragement and to Ana for her patience and love.

CONTRIBUTORS AND FUNDING SOURCES

Contributors

This work was supervised by a thesis committee consisting of Dr. Waruna Kulatilaka and Dr. Eric Petersen of the Department of Mechanical Engineering and Dr. Adonios Karpetis of the Department of Aerospace Engineering.

All work for the thesis was completed by the student, in collaboration with Nicholas Niemiec, Andrew Demko, Yejun Wang, Kevin Campbell, and John Stallings of the Department of Mechanical Engineering.

Funding Sources

NOMENCLATURE

Al	Aluminum
AP	Ammonium perchlorate
CEA	Chemical equilibrium application
Cu	Copper
Fs	Femtosecond (10^{-15} seconds)
h	Planck's constant
HgCl	Mercury chloride
HTPB	Hydroxyl-terminated polybutadiene
Hz	Hertz (s^{-1})
ICCD	Intensified charge-coupled device
LIBS	Laser-induced breakdown spectroscopy
Nd:YAG	Neodymium-doped yttrium aluminum garnet
nu (ν)	Frequency
Pb	Lead
PbSt	Lead stearate [$(C_{17}H_{35}COO)_2Pb$]
SNR	Signal-to-noise ratio
Ti:Sapphire	Titanium sapphire

TABLE OF CONTENTS

LIST OF FIGURES

LIST OF TABLES

1. INTRODUCTION

1.1. Background

Energetic formulations, such as gunpowder, explosives, and solid propellants, typically have metallic powders added to them, which enhance and tailor their properties such as heat release, density, and the specific impulse [1-4]. Other metallic particles can also be found as contaminants in these formulations or added from hardware used to handle them. When these formulations are combusted, the metallic particles can be released into the air. When this particulate matter is inhaled, it can lead to adverse health effects, such as pulmonary and cardiovascular disease, particulate matter-induced allergy, and cancer [5, 6]. People in the defense sector are particularly susceptible to these health threats because they operate and/or are in close contact with devices that employ energetic formulations. The goal of this work is to develop a real-time, robust sensing scheme that can detect the particulate matter, specifically metallic particles, in the air to determine the origin of the threat and safe operating distances from said threat where no safety equipment is needed. The scheme chosen as a candidate for this type of detection is the laser-based remote sensing system, laser-induced breakdown spectroscopy (LIBS).

LIBS is an elemental, analytical technique primarily used for determining the atomic constituents of a sample [7-10]. A high-energy laser pulse is focused onto a sample, generating a plasma in the region where an unknown material presents. The light emitted from this plasma is then collected and sent through a spectrometer, which disperses the light onto a CCD array. Based on the spectral lines detected and their relative intensities,

the composition can be determined [11-13]. LIBS is an adaptable technique that can be used on matter in any phase: solid, liquid, or gas [14]. LIBS has also been shown to be able to detect particles in aerosols or flames, which further demonstrates the versatility of this technique [15-25]. LIBS experiments can be performed in the field with little to no sample preparation [26, 27]. They are robust and relatively easy to set up. Fundamentally, LIBS can detect any element if the laser can supply sufficient energy and the collection device is sensitive enough in the region of the element's characteristic spectral emission. Because of these advantages, LIBS has already been employed in the defense sector, specifically for detecting chemical, biological, radiological, nuclear, and explosive (CBRNE) threats [8]. Hence, the objective of this work is to explore LIBS for characterization of explosive materials, specifically to detect the release of the metallic elements of aluminum (Al), copper (Cu), lead (Pb), and mercury (Hg) into the air.

1.2. Outline of Related Work

LIBS is a proven technique for detecting elemental species, including the aforementioned metallic particles [28-40]. There have also been LIBS studies of detecting these particular elements in aerosols [41-46]. Carranza, et al. demonstrated LIBS detecting Al in ambient air, and they observed an increase around the Fourth of July holiday, which they attributed to fireworks going off in the lower atmosphere [41]. This literature shows that LIBS can detect species at low concentrations and in the ambient environment, which suggests LIBS to be suitable and effective for the present objective. It is important to note, however, that the characteristics of plasma vary rapidly in its early stages of formation.

Several mechanisms such as Bremsstrahlung, Stark, Doppler, and pressure effects can broaden specific spectral lines resulting from the plasma [47]. After several hundred nanoseconds, the plasma transitions from being nearly opaque to being transparent to incident radiation [16]. Therefore, an optimal delay time with respect to the laser pulse is sometime after these effects have disappeared and the continuum background reaches minimal levels. Many published papers have described this temporal characteristic of LIBS with varying delay times from 150 ns to 6 µs [47-51]. The optimal delay time, as shown by these papers, depends on the system's specific parameters such as the laser energy, wavelength, pulse duration, the target characteristics, and the surrounding atmosphere. Therefore, to begin the investigation, a laser energy dependence and plasma decay study for our set up was performed with solid targets of Al, Cu, and Pb. A decision was made to investigate two schemes: one with a nanosecond (ns) pulse-duration laser and the other with a femtosecond (fs) pulse-duration laser. Fs-LIBS has been shown to improve the LIBS signal compared to ns-lasers, mainly by decreasing background signals [49, 52-54]. Once a better understanding of the plasma characteristics and an optimal signal-to-noise ratio (SNR) was achieved, the next study was conducted using propellant strands with various metallic additives at predetermined quantities. These propellant strands were burned, releasing the metallic additives into the air, where the LIBS signal is detected. This method of using propellant strands as a way to release metallic particles into the air was chosen to simulate the real environment as closely as possible, where metallic particles are released from high energy reactions of propellants and explosives.

1.3. Significance of the Thesis Research

The objective of this work is to explore LIBS for detecting harmful, metallic particles of aluminum, lead, copper, and mercury in the air released during the combustion reactions of HTPB/AP composite solid propellants, simulating real world environments. While LIBS has been used extensively for detecting elemental particles including metals during numerous previous studies, application of LIBS in the gas-phase reaction zone to characterize the emissions of metals near the source is very unique and challenging. Quantitative, spatially and temporally resolved information about metals released can provide critical information to design better and safer-to-operate propellants and explosive formulations with tailored energy release characteristics. Such measurements however, become particularly challenging because of the low number densities in the high-temperature gas-phase medium and the harsh chemical environment present in the region of interest. Although the present study is performed in a controlled laboratory setting with higher resolution devices than what would currently be able to be easily used in the field, such investigations will form the foundation for developing enhanced capabilities for future applications. This research will give a better understanding of how to use LIBS for this type of detection, which will enable and ease the transitioning of LIBS to an actual field environment. Being able to build upon an already proven technique such as LIBS is a major advantage for such applications. It has been shown that LIBS can be deployed in the field in the form of low resolution handheld devices as well as being shown to be field deployable by being used in the ChemCam instrument on the Mars Curiosity rover. Achieving this type of deploy-ability for this type of detection, in the field using compact,

easily transportable devices, is the ultimate goal of the present study [8]. The ability to detect these harmful particles will also enable establishing proper operating distances and ensure areas are safe for personnel. Hence the present work has laid the foundation for future field-based measurements by better understanding the fundamentals of this type of LIBS-based detection scheme.

1.4. Thesis Outline

LIBS is a proven technique for detection of elemental species, including the specific metallic particles being studied here. A comprehensive literature review of related LIBS developments and applications are presented in Section 2. Section 3 describes the present experimental apparatus, including how the preliminary solid target and propellant strand experiments are set up, the sample preparation, combustion and experimental diagnostics procedure. Subsequently presented are the results of the initial study with solid targets, which consists of a general wavelength detection as well as the laser pulse energy and gate delay optimization, and the propellant strand study, which includes a general detection study and a concentration study. For these studies, both ns and fs duration laser pulses are investigated. The finding of these studies are presented in detail in Section 4, Results and Discussion. Section 5 contains a summary, conclusions drawn, and an outline of future works.

2. LITERATURE REVIEW

Selected papers are reviewed that cover the fundamentals of LIBS, as well as what has been accomplished in the field of LIBS in terms of detecting the metallic elements of aluminum, copper, lead, and mercury in solid, liquid, and gaseous media. Also reviewed are papers that cover LIBS hardware of lasers and detectors.

2.1. Fundamentals of LIBS

2.1.1. LIBS Technique Basics

LIBS is both a qualitative and quantitative elemental technique. LIBS starts with a pulsed laser that is focused onto a sample whose elemental composition is to be determined. The focusing of this pulsed laser pulse generates a local assembly of atoms, ions, molecules, and free electrons, also known as plasma. The laser is pulsed due to the high amount of peak power required to generate this plasma. The white light from this plasma is collected and passed through a device that separates the light into its wavelengths. This separated light is then collected on a device that can record the intensity of each wavelength. The intensity versus wavelength can then be plotted and displayed as a spectrum [8, 55]. Figure 1 shows an example of a LIBS experimental apparatus using a spectrograph to disperse light onto a photodiode array (PDA).
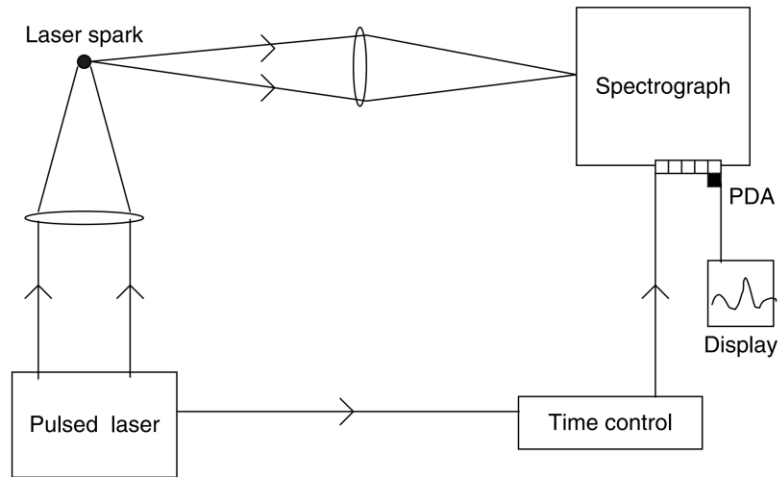
Figure 1. A typical LIBS apparatus for spectral analysis of a laser-induced plasma with a time-gated photodiode array (PDA) [55].

An example of a LIBS spectrum can be seen in Figure 2. LIBS is qualitative in that specific spectral peaks can be correlated with specific elements. For example, Figure 2 shows that LIBS was able to identify elements such as sodium, lithium, potassium, titanium, iron, aluminum, silicon, magnesium, oxygen, and calcium. LIBS can also be used quantitatively in that the intensity of each elemental species can be correlated to the number density of that element.
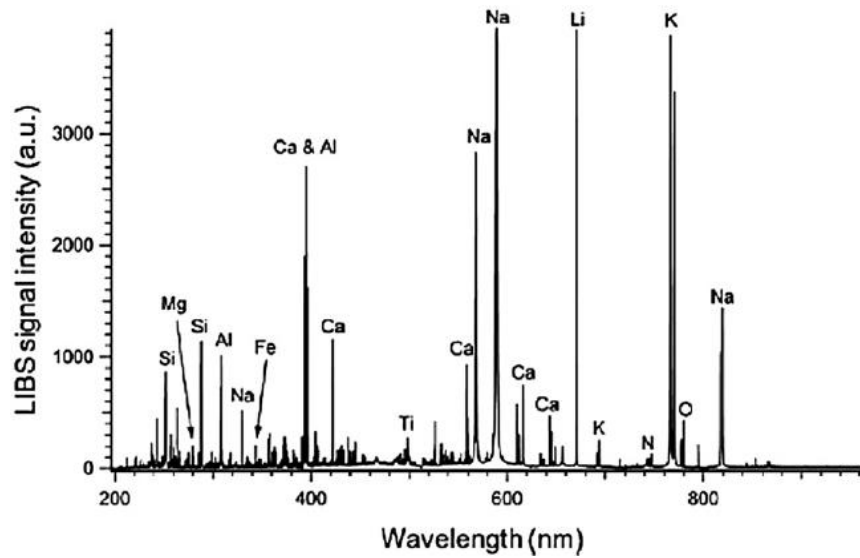
Figure 2. A typical LIBS spectrum from a solid sample of geomaterial containing multiple elements [56].

2.1.2. Plasma Generation and Effects

While it is clear that, in LIBS, the laser is generating the plasma, there are many processes on a wide range of time scales that occur during this laser ablation process. Figure 3 summarizes these processes and lists their typical time scale of occurrence. To generate the plasma in elemental LIBS, the laser photons must have enough energy to breakdown bonds in molecules, in some cases, and ionize the atoms.

8

Plasma ignition
fs laser (10^{12} – 10^{17} W/cm^2)

Electronic excitation and ionization
(10^{-15}–10^{-13} s)
Coulomb explosion (10^{-13} s)
Electron–lattice heating (10^{-12} s)

ns laser (10^7 – 10^{11} W/cm^2)

Thermal vaporization (10^{-9}–10^{-8} s)
Non-thermal ablation (10^{-9}–10^{-8} s)
Plasma shielding (10^{-9}–10^{-8} s)

Plasma expansion
and cooling

Shockwave propagation
Plasma expansion (10^{-11}–10^{-6} s)
Plasma radiation cooling (10^{-6}–10^{-4} s)

Particles ejection
and condensation

Nano particles formation (10^{-4}–10^{-3} s)
Ejection of liquid droplet (10^{-8}–10^{-6} s)
Solid exfoliation (10^{-6}–10^{-5} s)

Figure 3. Schematic illustration of the process of laser ablation during the LIBS process [55]

The light emitted from this plasma during the radiation cooling period is produced by the recombination or de-excitation of atoms and ions. These mechanisms are summarized with Equations 1, 2, and 3, where X is the target element [55].

$$X^+ + e^- \rightarrow X + h\nu \text{ (recombination)} \tag{1}$$

$$X^{+*} \rightarrow X^+ + h\nu \text{ (de-excitation of ions)} \tag{2}$$

$$X^* \rightarrow X + h\nu \text{ (de-excitation of atoms)} \tag{3}$$
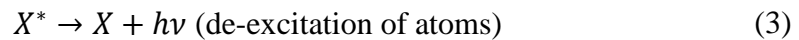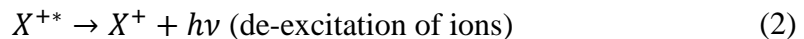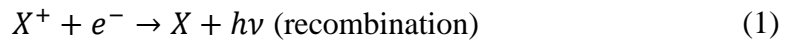
Figure 4 further demonstrates some of these transitions. From left to right, the first is a free-free transition, often referred to as Bremsstrahlung, next is bound-bound, then

free-bound, which is the recombination shown in Equation 1. Following that is an example of ionization from an excited state, and the final line is an example of ionization from the ground state. The continuum is mainly from the Bremsstrahlung and recombination processes. The Bremsstrahlung process is when free electrons emit a photon due to accelerating or decelerating as a result of colliding with other particles in the plasma or atmosphere. This process leads to a large amount of noise in the spectrum at early time periods. Therefore, the gate of the collection device must be delayed to avoid this emission in most cases, as was previously discussed.
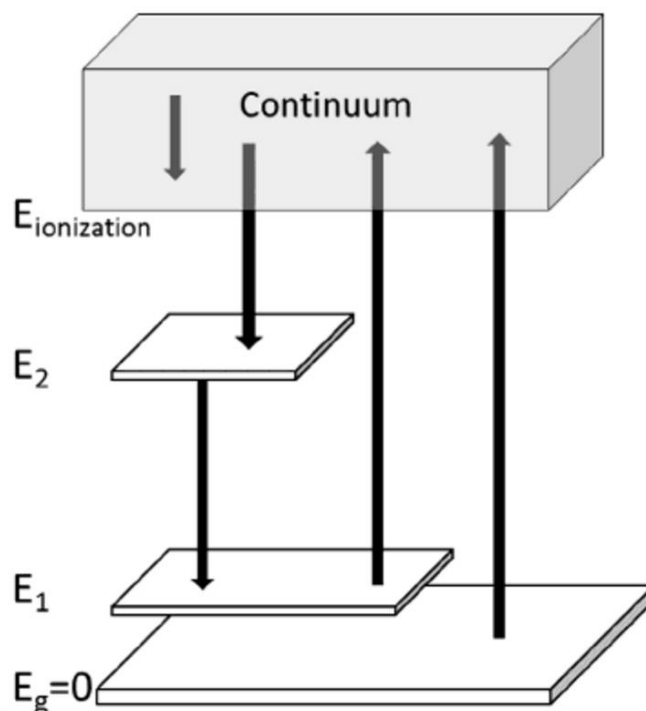
Figure 4. Illustration of energy transitions between specific levels of an atom or an ion during LIBS process [8].

2.1.3. Combination of LIBS and Complementing Techniques

While LIBS is a powerful elemental tool by itself, the combination of LIBS with a complementing technique, such as Raman spectroscopy or laser-induced fluorescence (LIF), would lead to improving the probability of detecting and identifying the correct substances [57, 58]. This technique of combining LIBS with specifically Raman has been shown by Moros et al. [59], Matroodi et al. [60], Gottfried et al. [57], and Miziolek et al. [58] with different setups, which are discussed below.

Raman spectroscopy is a technique that uses inelastic scattering of a laser beam to identify molecules in the substance being studied. This inelastic scattering occurs due to the rotational and vibrational transitions caused by the laser energy exciting the molecules to an elevated state [60]. While LIBS provides information on relative elemental content, Raman signal is related to the mass or size of the molecules as well as individual bonds in that molecule [57]. Another difference between LIBS and Raman is in the time scale of collection in order to get the best signal. While LIBS plasma and signal collection can typically last several microseconds, Raman signal coming from the re-emission of scattered photons from the molecules occurs almost simultaneously with the initial interaction of the photons with the molecule. In other words, when a nanosecond duration laser pulse is used, the Raman signal lifetime stays in this nanosecond regime [59].

Moros et al. used a combined LIBS-Raman device that consisted of an Nd:YAG laser to generate the signal and a homemade Cassegrain telescope. They focused the light collected by the telescope onto a fiber optic cable, and then they passed the light through two spectrometers (Shamrock sr-303i) onto a ICCD camera (Andor iStar). The only

difference between the two spectrometers is that the Raman spectrometer has a 300 g/mm grating with an observable wavelength range from 534 to 825 nm, while the LIBS spectrometer has a 150 g/mm grating with an observable wavelength range from 235 to 828 nm [59].

Matroodi et al. also used a combined LIBS-Raman device with an Nd:YAG laser as the excitation source. They then passed the laser through a Glan-Taylor prism to split the beam in two. The beams are then directly to the sample surface, where the plasma and scattering occur. The light from the scattering and plasma was then mixed and sent through a Echelle spectrograph onto an ICCD camera [60].

Miziolek et al. [58] and Gottfried et al. [57] used the same setup for Raman and LIBS detection. They used two separate systems for their work. The LIBS system uses a dual-pulsed Nd:YAG laser at 1064 nm while the Raman system uses both a Nd:YAG laser at 532 nm and a KrF laser at 248 nm. They were able to successfully demonstrate the technique for explosive detection [57, 58].

2.1.4. Pulse Widths and Their Effects

Papers by Angel et al. [52], Barthelemy et al. [49], Le Drogoff et al. [53], and Eland et al. [61] were selected for this review of laser pulse widths and their effects on the LIBS plasma and collection.

Angel et al. used a dual-pulsed ns-duration laser and then a single shot picosecond (ps) and fs-laser excitation times for copper LIBS and compared the results from different pulse durations. The result was that the shorter pulses showed a much lower background

signal compared to the nanosecond pulses. They also showed that the atomic emission decayed much more rapidly in the shorter pulse scheme. They suggested that, for the ps- and fs-schemes, a non-gated detector for LIBS was effective due to the relatively low background signal. They also found that the higher the repetition rate, the better the LIBS signal would be for a given measurement time [52].

Barthelemy et al. demonstrated similar results using an aluminum plate. More about their experiment can be found in the aluminum LIBS section [49]. Le Drogoff et al.'s work continued to support the trend of faster decay of continuum and atomic emission, again with an aluminum alloy [53, 54]. Eland et al. showed in their work that the material ablation was much less in the lower pulse duration lasers than in the longer pulse, comparing 1.3 ps duration to 7 ns [61].

2.2. LIBS in Solid and Liquid Media

LIBS has become a proven elemental detection technique for over the past 30 years, so there is extensive literature on the use of LIBS in solid and liquid media for the elements of aluminum, copper, lead, and mercury. A few papers focusing on each element are outlined in their respective sections to highlight some techniques for detection. The important experimental details for each paper, such as laser wavelength and pulse energy, collection settings, such as gate delay, and hardware, are outlined along with some experimental results.

2.2.1. Aluminum

Papers by Fichet et al. [32], Cremers et al. [31], Sabsabi et al. [50], Rieger et al. [37], Stravropolous et al. [38], and Barthelemy et al. [49] were selected for the aluminum LIBS in solid and liquid media review.

Fichet et al. in 2001 focused on doing a quantitative elemental analysis for a wide range of elements in both water and oil due to the nuclear industry needing a method for detecting trace metals to control processes or effluence. Fichet used a Nd:YAG laser (Quantel YG 580) operating at 532 nm with a pulse duration of 14 ns. The laser beam with a pulse energy of 60 mJ/pulse at 1 Hz produced a plasma on the surface of the two liquids. A 1 m spectrometer (THR 1000) was used with a 2400 g/mm grating along with an ICCD camera (Princeton Instruments EEV). They took 100 spectra and summed them together to get their results. A time delay of 500 ns and a gate width of 25 µs was used. They could detect aluminum lines of 309.27 and 396.152 nm down to 10 µg/mL in water, and the aluminum line of 396.15 nm down to 10 µg/mL in oil [32].

Cremers et al. in 1984 focused on detecting chemicals in water. Using a Nd:YAG laser (Quanta Ray DCR) at the fundamental frequency of 1064 nm, with a pulse width of 15 ns, 45 mJ/pulse, a time delay of 0.5 µs, and a gate width of 1 µs, they could detect aluminum in water down to 20 µg/mL [31].

Sabsabi et al. in 1995 performed a quantitative analysis of aluminum alloys and characterized the plasma generated by their laser. They noted that the optimal time delay is related to the energy of the laser, its wavelength, the target characteristics, and the surrounding atmosphere, so it is extremely dependent on an experiment's setup. They

recorded the Al II line of 281.6 nm at various time delays from 50 ns to 3 µs, showing that at around 500 ns the signal began to clean up for this specific peak. For their experiments they used a Nd:YAG laser (Surelite I 10) at the fundamental wavelength of 1064 nm. They also varied the power from the threshold of generating plasma up to 500 mJ/pulse. The laser operates at maximum 10 Hz, but for most experiments they ran it at single shot, with an 8-ns pulse duration. They used a 2/3-m spectrometer with a 2400 g/mm grating blazed for 300 nm for data collection with a photodiode array as the detector [50].

Rieger et al. used a KrF laser at 248 nm with 10 ns and 50 ps pulses with an energy range of 0.1 to 100 µJ for investigating silicon and aluminum plasmas. Above 3 µJ, there was very little difference between the two pulse lengths in their setup. They conducted their experiments with an aluminum plate in air and focused on the 394.4 and 396.2 nm lines monitored by an interference filter (400 nm, 25 nm FWHM) and PMT (RCA 7265) that has a high sensitivity at 400 nm [37].

Stravropolous et al. studied the calibration measurements using Nd:YAG, 1064 nm, ns- and ps-lasers with pulse durations of 5 ns and 35 ps respectively. They used aluminum, manganese, iron, and silicon targets. They found the optimal time delay, gate width, and laser energy for their setup. They reported detecting aluminum down to 3.5 ppm with the nanosecond scheme and 15 ppm with the picosecond scheme [38].

Barthelemy et al. studied aluminum laser plasma produced in air with time and space resolved measurements of electron density and temperature. They used a Nd:YAG laser at 1064 nm, 532 nm, and 266 nm, which had a pulse duration of 6 ns, as well as a Ti:Sapphire laser at 800 nm with a pulse duration of 80 fs. The laser energy was set to 40

15

mJ and the repetition rate was held at 2 Hz. They collected their spectra with a 0.55 m Jobin-Yvon Triax 550 spectrometer with a 3600 g/mm grating. They used an ICCD camera (Andor Technologies) as their detector and stepped through various time delays with respect to the laser, ranging from 50 ns to 3 µs. They also noted that in the Nd:YAG case, the wavelength didn't seem to effect the result [49].

2.2.2. Copper

Papers by Fichet et al. [32], Fichet et al. [62], Autin et al. [48], Nemet et al. [47], and Le Drogoff et al. [54] were selected to showcase some copper LIBS work in solid and liquid media.

Fichet et al. studied trace metals in both water and oil for nuclear applications. Their experimental setup is described in the previous section. They reported being able to detect the 324.75 nm line down to 7 µg/mL in water and 5 µg/mL in oil [32]. In 2003, Fichet, et al. decided to use ab Echelle spectrometer coupled with an ICCD camera. In this study, they could detect copper down to 2 µg/g in an aluminum alloy [62].

Autin et al. (1999) produced plasma from a copper target using a nitrogen laser (SOPRA-type 804C) at 337 nm in atmospheric air. The laser had a pulse energy of 3 mJ, a 10-ns pulse duration, and a repetition rate of 25 Hz. They reported detecting down to 1-10 ppm. They used two detection schemes. The first used a 0.6 m Jobin-Yvon HRS monochromator with a 2400 g/mm grating with a PMT (Hamamatsu R928) as the detector. The second was a 0.5 m Dilor spectrometer, also with a 2400 g/mm grating, equipped with a multichannel, photodiode, gate-able, intensified detector array (Hamamatsu V 3063U

with Reticon 1024 SF diodes). A gate width of 100 ns was used. A range of time delays was used from 100 ns to 1000 ns [48].

Nemet et al. in 1995 used a Nd:YAG laser at 1064 nm, 1 Hz, 15 mJ/pulse and 15 ns pulse duration to produce plasma from copper targets. They showed that emission lines appeared after 10-300 ns, and they superimposed them on the continuum background. They noted that these lines were severely broadened by Doppler, pressure, and Stark effects. With a gate width of 100 ns, they determined that the gate delay that gave them the maximum signal was 160 ns after the laser pulse for the 324 and 327 nm lines. They varied the delay from 40 ns to 1000 ns [47].

Le Drogoff et al. used 100 femtosecond laser pulses from a Ti:Sapphire laser to generate plasma from an aluminum alloy and detected the minor elements of magnesium, iron, silicon, manganese, and copper. The laser was set at 50 mJ/pulse, 800 nm wavelength, and 10 Hz. They used a 1 m Czerny-Turner spectrometer (Spectra Pro 500i, Acton Research Company) with a 3600 g/mm grating blazed for 300 nm. The spectra were recorded by an ICCD camera (Andor ICCD). They showed a faster decay of continuum and spectral lines, and a shorter plasma lifetime with the femtosecond pulses compared to longer pulse times. They stated that plasma generated from femtosecond pulses exhibited a faster thermalization compared to plasmas generated by nanosecond pulses. They could detect the 324.75 nm line of copper down to 7 ppm and the 521.82 nm line down to 204 ppm [54].

17

2.2.3. Lead

Once again Fichet et al. [32] and Fichet et al. [62] made the list of papers, but this time for LIBS conducted in solid and liquid media trying to detect lead. Also selected were papers by Vander Wal et al. [39], Theriault et al. [63], and Zhang et al. [46], which all focused on lead detection using LIBS.

Fichet et al. (2001) with the experimental setup discussed above, detected the 405.87 nm line down to 100 µg/mL in water and 90 µg/mL in oil [32]. In the Fichet et al. (2003) experiment using the Echelle spectrometer and aluminum alloy as the target, lead was detected at 15 µg/g of aluminum [62].

Vander Wal et al. used trace metals evaporated onto amorphous graphite. A Nd:YAG laser (Continuum, Model 8030 Powerlite) with a fundamental wavelength of 1064 nm and 8 ns pulse duration was used to generate the plasma. A 0.25 m spectrograph (Acton Research, Model SpectraPro 275S) with an ICCD (Princeton Instruments, Model ICCD-576-S/RB-T) was used to collect the data from the light of the plasma. They used a gate width of 1 µs and gate delays of 1 µs, 5 µs, and 10 µs. They detected lead down to 2 ppm with the 261.37, 261.47, 280.2, and 283.31 nm lines, and down to 10 ppm with the 405.78 and 406.21 nm peaks [39].

2.2.4. Mercury

For the detection of mercury in solid and liquid media using LIBS, the papers by Vander Wal et al. [39] and Stepputat et al. [64] were selected.

Vander Wal et al., once again, used the experimental methods discussed above for the detection of mercury as an evaporated solution on a graphite surface. They reported detection limits of 10 ppm using the 253.65 nm Hg line [39].

Stepputat et al. used LIBS for detection of mercury in polymers. They used a Nd:YAG laser (Powerlight PL8030, Continuum), which was operated in single and double pulse mode with a wavelength of 1064 nm, pulse energy of 350 mJ/pulse, pulse duration of 7 ns, and a repetition rate of 30 Hz. The plasma radiation was passed through an Echelle spectrometer (ESA 3000EV/I, LLA Instruments GmbH) and imaged onto an ICCD megapixel full frame camera (Kodak KAF 1001). A time delay of 1.5 µs and an integration time of 9.5 µs was used. The reported limit of detection was 18 µg/g of polymer [64].

2.3. LIBS in Gas-Phase Media

While many papers demonstrate LIBS detection of aluminum, copper, lead, and mercury in solid and liquid media, the number density drops drastically for gas. Therefore, the LIBS signal drops and is harder to detect. Although Radziemski demonstrated that LIBS would work for aerosols in 1983, there wasn't a lot of work in this area until about the year 2000 [18]. The papers selected for LIBS detection in a gas media are Caranza et al. [41], Mukherjee et al. [44], Essien et al. [43], Cheng [42], Neuhauser et al. [45], and Gleason et al. [65].

Caranza et al. demonstrated the use of LIBS in ambient air to detect aluminum. They used a 1064 nm Nd:YAG laser, with a 10 ns pulse duration, 375 mJ/pulse and a 5 Hz repetition rate. Their time delay was 30-40 µs and their gate width was 40-150 µs.

19

They were able to detect an increase in the ambient air in their lab around the Fourth of July holiday, which they attributed to fireworks being fired in the lower atmosphere [41].

Mukerjee et al. demonstrated the use of LIBS for detecting aluminum nanoparticles in an aerosol. They found an optimal delay time of 46.7 µs with a gate width of 15.5 µs. They used a Nd:YAG laser at 1064 nm operating at 350 mJ/pulse and 10 Hz, with a pulse width of 4 ns. For detection, they used a 0.5 m spectrometer (Acton SpectraPro 500i) with a 1200-g/mm grating and an ICCD camera (Princeton Instruments PI-MAX; Thomson 512 x 512 CCD) [44].

Essien et al. in 1988 demonstrated LIBS as a technique for detecting lead in an aerosol. They used a Nd:YAG laser (Laser Photonics YQL-102) at 1064 nm, 15 ns pulse duration, 100 mJ/pulse, and a repetition rate of 10 Hz. For detection, they used a 0.5 m monochromator (Jarrell-Ash 82-020) with a PMT (Hamamatsu 1P28) with a delay of 20-40 µs and a gate width of 1 µs. With this setup, they were able to detect lead at 0.21 mg/m^3 [43].

Cheng demonstrated a detection of mercury in an aerosol down to 9.8 ng/m^3 using LIBS. They used a Nd:YAG laser at 532 nm, 10 Hz, 100-150 mJ/pulse, and 7 ns pulse duration to generate the plasma. They then passed the light from the plasma through a spectrometer and ICCD combination. They showed that delay time changed when using helium versus air, so they had a varying time delay throughout [42].

Neuhauser et al. demonstrated the use of LIBS to detect both Cu and Pb in an aerosol, although they actually performed the study on a filter placed in an aerosol. They did this study for health reasons, which is similar to the goals of this study. They used a

Nd:YAG laser (SL282, Spectron) at 532 nm, with an energy of 70 mJ/pulse, 6 ns pulse duration, and a repetition rate of 10 Hz. They used a 0.275 m spectrometer (Spectra Pro 275, Acton Research Company) with a 2400 g/mm grating with a gate-able, intensified diode array (OMA-System, SI). They reported detection limits of 0.01 µg/cm^2 (which was assumed to be 0.03 µg/m^3) for copper and 0.06 µg/cm^2 (which was assumed to be 0.18 µg/m^3) for lead [45].

Gleason et al. presents a study of mercury atomic emission and the interactions between oxygen and mercury. Using a Nd:YAG laser at 1064 nm, 10 ns pulse duration, 300 mJ/pulse, and at 5 Hz repetition rate, they showed that at long delay times (10-100 µs), oxygen significantly reduced the 253.7 nm mercury line. This decrease was due to the recombination of atomic oxygen. A 0.275 m spectrometer with a 2400 g/mm grating was used along with an ICCD camera with a detector array of 1024 x 256 [65].

Table 1 summarizes all lines used in the sources reviewed here for the reader's convenience.

Table 1. Summary of LIBS spectral lines used in gaseous media

Element	LIBS Emission Line(s) (nm)	Source	Used in this work
Al I	396.152	Carranza [41]	Yes
	394.4		
Al I	396.152	Mukherjee [44]	Yes
Pb I	405.8	Essien [43]	Yes
Hg I	435.8	Cheng [42]	Yes
Cu I	324.8	Neuhauser [45]	Yes
Pb I	405.8	Neuhauser [45]	Yes
Hg I	253.7	Gleason [65]	No

2.4. LIBS Hardware

2.4.1. Laser Sources

Cremers and Radziemski give a comprehensive overview of some laser systems used in LIBS applications in their book "Handbook of Laser-Induced Breakdown Spectroscopy" [8]. In general, lasers work by pumping a medium with energy, which produces stimulated emission in the medium that is further amplified. For a Nd:YAG laser, the medium is a Nd:YAG crystal that is pumped using flashlamps. The flashlamps pump broadband light into the lasing medium where a small portion of the light is absorbed by the Nd^{3+} ions doped in the YAG matrix. If the flashlamps dump enough energy into the Nd:YAG crystal, a population inversion occurs, where the upper electronic level of the

lasing atomic transition is more populated then the ground state. When this happens, photons that have the same frequency as the lasing transition will experience amplification by inducing stimulated emission, which is the decay of some of the Nd^{3+} ions from the upper level to the lower level. Placing two mirrors at the wavelength of this stimulated emission creates a resonant cavity, where the light will pass back through the medium, amplifying it further, which results in the highly monochromatic and polarization properties of a laser. For LIBS applications, a high laser power is needed to generate a plasma. The practical way to do this is to pulse the laser and employ a Q-switch. A Q-switch is an electro-optic switch shutter that is positioned in the lasing cavity such that it prevents photons at the laser wavelength from going through the entire path of the resonant cavity, which allows the population inversion to become very high. When the Q-switch is switched, it becomes transparent, which allows photons to travel the whole length of the resonant cavity and results in a high-power pulse of short duration. For a Nd:YAG laser, this is typically on the order of 5-10 ns. Repetition rates for Nd:YAG lasers typically range from single shot to 20 pulses per second (20 Hz). A fraction of this pulse energy leaves the cavity through an output coupler, which is a partially transmitting mirror. The fundamental wavelength for a Nd:YAG laser is 1064 nm, so the resonant cavity must be some integer multiple of this length. The 1064-nm beam can be used to generate plasma, or it can be frequency doubled, generating 532 nm, which is a bright green beam, or frequency quadrupled, generating 266 nm, by passing the beam through one or two birefringent crystals, typically KDP (potassium dihydrogen phosphate) or KD*P (potassium dideuterium phosphate), for the second harmonic generation (SHG) and fourth

harmonic generation (FHG) respectively. The third harmonic, 355 nm, can also be generated by taking 532 nm and mixing it with residual 1064 nm. Each harmonic generation typically has an energy conversion of approximately 50%. Different wavelengths may be needed for different types of LIBS. Generally, the laser wavelength either needs to be away from the spectral lines being observed due to the laser's high intensity, or the laser needs to be tuned to exactly the wavelength of one of the lines being studied, which can increase the LIBS signal of other spectral lines. Filters and polarizers can be used to block the laser beam wavelength, but it is generally easier to keep the laser away from the wavelength region being studied.

For femtosecond lasers, a Ti:Sapphire crystal is commonly used as the lasing medium that is pumped by other continuous-wave lasers, such as a Nd:YVO$_4$ laser, to produce a laser near 800 nm. Due to the short pulse width, the spectral content of the pulse is relatively broad. The actual method of these femtosecond lasers is quite complex and beyond the scope of this work. In the end, this laser has a very short pulse duration and can have a very high repetition rate. Femtosecond lasers have some advantages over their nanosecond counterparts for use in LIBS in that they have a different ablation mechanism, which results in less heating and melting of the sample around the ablation crater, increased accuracy and precision of quantitative measurements, and reduced fractionation of the ablated material, which better maintains the bulk material stoichiometry. The disadvantage of fs-lasers is that they are still relatively new, so they are not as robust and as easily field-deployable as Nd:YAG lasers. Therefore, for now, fs-lasers are still more laboratory-based instruments.

2.4.2. Detectors

Cremers and Radziemski give a good general overview of some detection schemes used in LIBS applications in their book "Handbook of Laser-Induced Breakdown Spectroscopy" [8]. The light from the plasma is passed through a device that separates the light by wavelength. Typically, either an Echelle spectrograph or a Czerny-Turner spectrograph are used. An Echelle spectrograph uses two dispersion stages to disperse the light in two orthogonal directions. The result is a two-dimensional ladder-like image where the spectral orders correspond to rungs of the ladder due to horizontal and vertical dispersion. Typically, there are no moving parts in an Echelle spectrograph, which makes it robust and portable. Because they have a two-dimensional output, Echelle spectrographs generally provide more information, for example, they are able to give near infrared (NIR), visible, and ultra-violet (UV) wavelengths and their intensities all in one frame. Czerny-Turner spectrographs, on the other hand, use a rotating grating that disperses the light in sections of wavelengths. The bandwidth of these wavelengths depends on the resolution of the grating. Once the light has been dispersed, a detector is needed to detect the counts of photons at each wavelength. The types of detectors include photomultiplier tubes (PMT), avalanche photodiodes (APD), photodiode arrays (PDA), intensified PDA (IPDA), charge-coupled devices (CCDs), and intensified CCDs (ICCDs). Each has specific reasons why it may or may not be used. These reasons might include cost, sensitivity, and whether it detects in a one-dimensional or two-dimensional array. In this work, a CCD and ICCD are used. These chips are varying array sizes of pixels and are generally two-dimensional. These pixels convert incoming photons to electrons, which are

stored in potential wells. CCD chips can collect multiple frames of photons and stack the converted electrons in single-electron wells, leading to an increase in signal. The wells are then read off in a conveyor belt fashion, by shifting each row down to the read-off row, and then shifting the columns in the read-out row over to a convertor, which converts the electrons to a digital signal. An intensifier placed in front of a CCD chip consists of three aspects: a photocathode, a micro-channel plate (MCP), and a phosphor screen. The photocathode converts incoming photons to electrons. Those electrons are then amplified over the MCP by applying a voltage across it. When the electrons go through the micro-channels and get enough energy, they generate secondary electrons from the walls, which is the amplification. The phosphor screen then turns these electrons back into photons, which are then sent to the CCD chip. ICCDs can allow high time resolution by gating, which is done by removing the applied voltage to the MCP and effectively blocking any light from coming through. ICCDs can obviously also detect much lower intensities than regular CCDs, but they are more expensive.

3. EXPERIMENTAL APPARATUS AND PROCEDURE

3.1. Experimental Apparatus

The nanosecond scheme experimental apparatus, seen in Figure 5, has a 10 Hz, Nd:YAG, nanosecond pulse duration laser, which operates at 1064 nm. This 1064-nm beam is then frequency doubled, so the beam on the optical table is 532 nm, which is a bright green color. The beam is directed by mirrors (RX-532-45-B-1025, Lattice Electro Optics (LEO)) and then passed through a half waveplate (CWO-532-02-10, LEO) and polarizer (TP-532-B-2025, LEO) combination. This combination of half waveplate and polarizer allows for adjustment of the laser pulse energy by turning the waveplate. Then, the approximately 10-mm diameter laser beam is focused using a 200-mm focal length, BK7, planar convex lens (B-PX-25.4-200, LEO), which produces a beam waist of approximately 66 microns. The focal region of the laser is where the plasma is produced. In Figure 5, a propellant strand's flame is shown in this focal region. The propellant strands are placed on a vertically adjustable platform, which allows for the same placement of the focal region for each sample. The propellant platform can also be switched out for a vertical plate holder, which was used for the preliminary LIBS investigation. The light from the plasma, whether from the propellant strand combustion zone or plate, is then collected using a collection optic (84-UV-25, Ocean Optics). It is worth noting that a polarizer (TP-532-B-2025, LEO) is placed in front of the collection optic to block the 532-nm signal. The collection optic then focuses the plasma light into a fiber optic cable (QP1000-2-SR, Ocean Optics). The fiber optic cable transmits the light to a spectrometer.

The spectrometer disperses the light onto a CCD array. The CCD array then counts the intensity and location, which is then transmitted to a computer, where a LIBS spectrum is produced. The spectrometer shown in Figure 5 is an Ocean Optics Flame S micro-spectrometer, which was used for general, low resolution, robust, initial surveying of the spectrum.
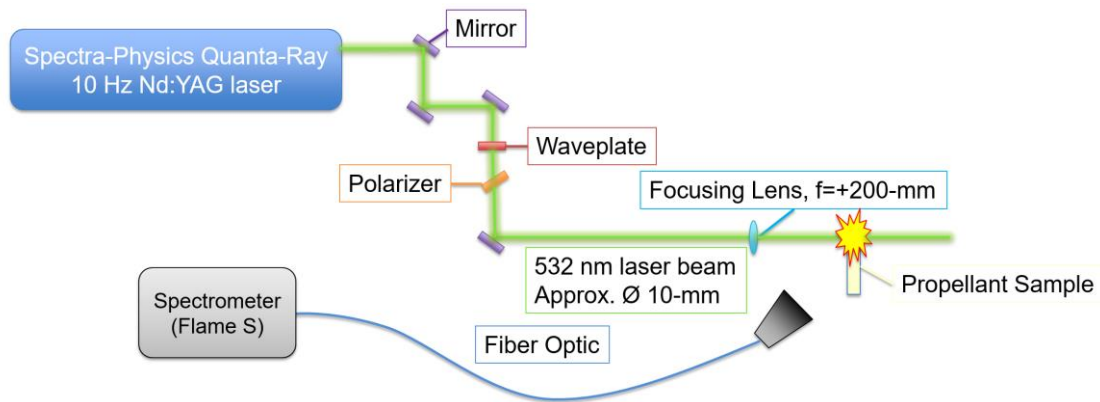
Figure 5. Nanosecond-laser experimental apparatus showing the approximate beam path and key optical components.

After the initial surveying is complete, and a more resolved signal is needed, the apparatus is switched to the configuration shown in Figure 6. The only difference in the configuration sequence is after the collection optic. The original fiber optic is switched to a new cable (LG-455-020-3, Princeton Instruments). The micro-spectrometer is switched to a Princeton Instruments 1/3-meter spectrometer/intensified CCD (IsoPlane 320/PI MAX 4) combination. The spectrometer has 3 gratings: 150g/mm, 1200g/mm, and 2400g/mm. The ICCD camera allows for better time gating than the micro-spectrometer, having nanosecond resolution compared to millisecond.
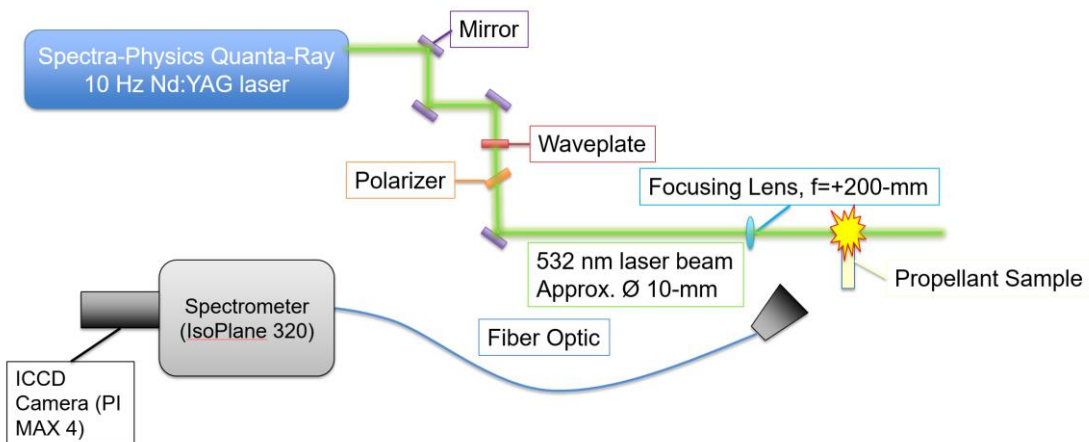
Figure 6. High-resolution detection experimental apparatus showing the approximate beam path and key optical components

The femtosecond switches the Nd:YAG laser for a Spectra Physics Solstice Ace, 80 fs pulse duration, 1-kHz repetition rate, Ti:Sapphire laser, which operates at 800 nm, which can be seen in Figure 7. The same basic principles remain from the nanosecond scheme. The only changes are the laser, the wavelength (so all optics are optimized for 800 nm instead of 532 nm), and the focusing lens has a +100-mm focal length opposed to +200-mm, which produces a beam waist of approximately 100 microns. The laser is also operated at a laser pulse energy of 4 mJ/pulse compared to ~100 mJ/pulse as with the Nd:YAG. Figure 8 shows an actual picture of the nanosecond scheme setup.
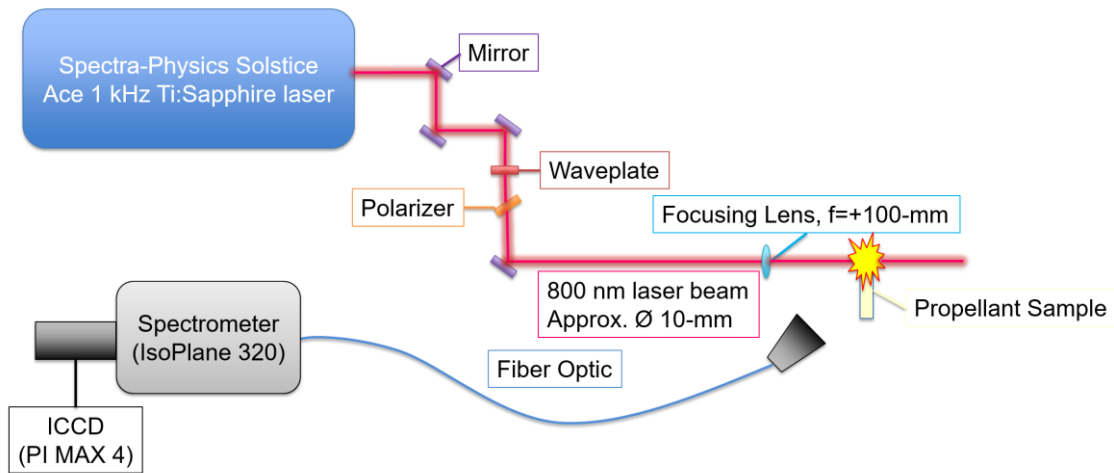
Figure 7. High resolution femtosecond-pulse-duration experimental apparatus showing the approximate beam path with important optical elements.
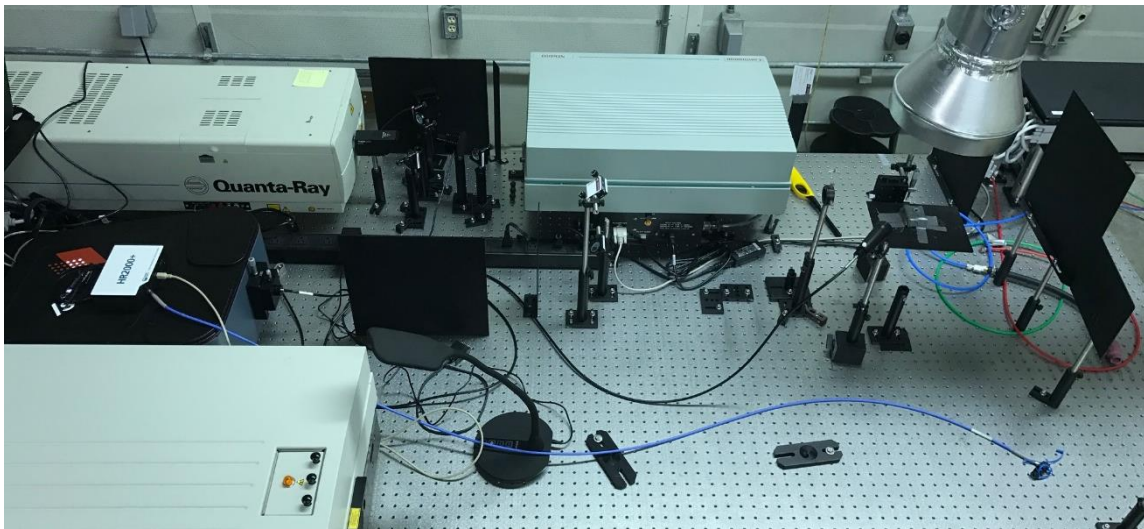
Figure 8. Photograph of the actual nanosecond-duration experimental apparatus in the Laser Diagnostics and Imaging Laboratory located at the TEES Turbomachinery Laboratory.

The propellant strands were prepared by Dr. Petersen's student Andrew Demko, who has many years of experience making these HTPB/AP composites. Propellants were mixed by hand for small, laboratory-scale mixtures of 20-g batches. Formulations were

mixed using a procedure that has been validated to produce consistent results and that are identical to a mechanical mixer in a previous work [4, 66]. The mixing takes place under a Labconco fume hood to reduce the chance of exposure to harmful chemicals. Each ingredient is weighed to within 0.01 g on a digital scale to maximize the repeatability of the formulation. The uncertainty of the mass percentages is ±0.25%. The metals were mixed into the HTPB first, ensuring that the metal particles were fully coated with HTPB. After the metals were well mixed, the AP was added followed by the IPDI curative. Vacuuming the mixture removed air pockets in the propellant. Each mixture was heated to 65 °C to lower the viscosity during mixing. The propellants were then cast into a Teflon tubing with a 4.76-mm diameter at a length of approximately 30 mm. Table 2 provides the mixture composition and particle size for each propellant sample tested in this study.

Table 2. HTPB/AP-based propellant mixtures used for LIBS detection of metals released to the gas phase.

Additive Name	Additive Chemical Formula	Particle Size*	% Additive (by mass)**
Aluminum	Al	24 µm	16
Aluminum	Al	24 µm	10
Aluminum	Al	24 µm	5
Lead	Pb	24 µm	16
Lead Stearate	$(C_{17}H_{35}COO)_2Pb$	24 µm	16
Copper	Cu	100 nm	2
Copper	Cu	100 nm	5
Copper	Cu	24 µm	20
Mercury Chloride	Hg_2Cl_2	24 µm	16

*as provided by the source of purchase

**Based on the sample preparation method described in the text

Figure 9 shows an example of what the propellant strands look like, with (left) and without (right) the Teflon tubing they are cured in.

Figure 9. Propellant strands with Teflon tubing (left) and without Teflon tubing (right) [67].

It is worth noting that although great care was taken in the sample preparation, including calculating the adiabatic flame temperatures with ProPEP, which uses the NASA chemical equilibrium application (CEA) to make sure the combustion temperatures were high enough to ignite the added metallic compounds, the flames of the different propellant types looked very different. Even from strand to strand within the same propellant type, the flame would sometimes act differently, burning in different geometries, etc. Figure 10 and Figure 11 demonstrate this difference. Figure 10 shows a still image of the burn of a 16% Al sample. The aluminum seems to fly off energetically and go all over, while in Figure 11, which shows a still image of a copper burn, the flame

plume seems to jet upwards without any copper particles flying off in the same way as the aluminum. While the aperture settings were not perfect for the copper settings, as Figure 11 is darker than Figure 10, it also demonstrates that the aluminum propellant strands give off a much more intense light than the copper.
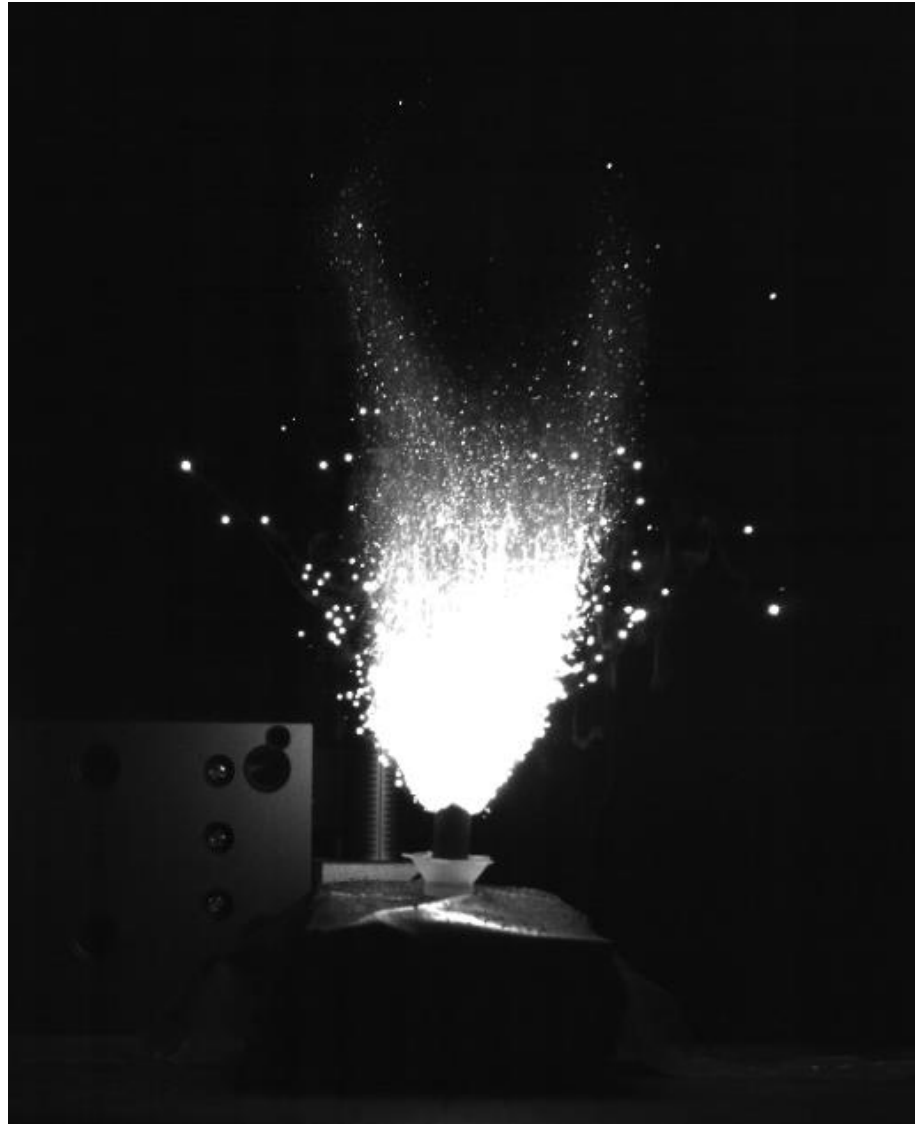
Figure 10. A photograph of a sample with 16% Al in AP/HTPB propellant strand burning on a vertically adjustable platform. This image is extracted from high-speed video recorded at 1 kHz during a complete burn.

Figure 11. 5% Copper propellant strand burned on vertically adjustable platform. Still image extracted from high seed video taken during burn.

3.2. Experimental Procedure

For all experiments, the Nd:YAG laser was allowed to warm up until the power level was at steady state. The power was measured with an Ophir power meter (7Z02724) and recorded using Ophir's StarLab software. The power was measured in front of the focusing lens, to negate any effects from losses through the mirrors. The power is then converted to laser pulse energy by multiplying by 10, due to the operating frequency of

the Quanta Ray being 10 Hz. The laser pulse energy is recorded before each experiment. If the pulse energy needs to be changed, the waveplate is turned such that the laser energy is correct.

For the preliminary experiments, solid plates of aluminum, copper, and lead were used as the targets. The plates were attached vertically to a pivot-able stand. The plates were placed at an approximately 45° angle relative to the incoming laser beam and approximately in the focal region of the laser. The plates were then rotated slightly until the plasma sound was approximately maximized, which was determined by ear. During a test run, a single-axis translation stage (LT1, Thorlabs) was used to move the plate around such that the laser would not ablate too much material at the same location, which would change the signal level. The collection optic was then adjusted until the spectrum was maximized, which was verified using the micro-spectrometer.

The first study performed was a wavelength study to ensure the spectra of the metals were being detected correctly. An approximate laser energy of 140 mJ/pulse was used. Initially, the micro-spectrometer was used for a large range survey of the wavelength. The micro-spectrometer was set with a 1,000-ms integration time and averaging 10 frames. Once a general idea of signal levels and highest intensity peaks was achieved, the high-resolution spectrometer/ICCD combination was used, which was first calibrated for wavelength with a Princeton Instruments neon-argon calibration lamp. The wavelength was then recorded using a 2,000-ns gate width, approximately 200 ns delay with respect to the incoming laser, the 150 g/mm grating with a blaze angle optimized for 300 nm to disperse the incoming light, 115 rows binned vertically on the CCD chip, 5

averaged exposures per frame, and the various gains and on CCD accumulations of 6, 50, and 3 for aluminum, copper, and lead plates respectively.

The next preliminary study was a laser energy dependence study, which was again performed with solid plates, specifically an aluminum foil plate. The micro-spectrometer was used for recording the spectra with an integration time of 300 ms, and 10 scans were averaged for each spectrum. The laser pulse energy was varied at 9 different levels, from as low as 12.4 mJ to 132.2 mJ, using the waveplate/polarizer combination.

The final preliminary study was the plasma decay scans. The study was performed on all three plates: aluminum, copper, and lead. The high-resolution spectrometer/ICCD combination was used, due to the higher time gating resolution. The gain was set at 2, 2 on CCD accumulations, or exposures, 150 rows binned, and a fixed gate width of 20 ns was used. The detection gate delay was varied from -40 ns before the laser pulse to 1000 ns after, in steps of 20 ns. A laser energy of 100 mJ/pulse was used.

Moving on to the propellant strand studies, the first propellant strand experiment performed aimed to detect the various metallic additives in the flame of the HTPB/AP base propellant. A laser pulse energy of 100 mJ/pulse was used. A candle holder was used to hold the propellant stick in place. The candle holder was placed in a foam block, which was attached to a vertically adjustable platform. The platform was raised or lowered to position the focal region of the laser at approximately 3 mm above the surface of each propellant strand. An exhaust vent approximately 10 inches above the propellant strands was used to transport the combustion products outside the lab. When ready, the propellant strand was lit with a handheld torch. The spectra were recorded slightly before lighting

and completed after the strand had completed its burn. The first burns were recorded with the micro-spectrometer which was triggered on the laser pulse and had a collection gate of 4 ms. Once a general idea of signal levels was achieved, the high-resolution spectrometer/ICCD combination was used. A delay with respect to the laser of 300 ns was used along with a collection gate width of 1000 ns, a gain of 5, 5 on CCD accumulations, 150 binned rows, the 150 g/mm grating with a blaze of 300 nm, and a center wavelength of 375 nm.

The next study with the propellant strands was a concentration study. The aluminum propellant strands with compositions of 5%, 10%, and 16% aluminum by mass were used. The same procedure as before was used in regards to burning the propellant strands. The only setting changed on the ICCD was only collecting 1 on CCD accumulation per spectrum. In other words, each spectrum corresponded to only one laser pulse.

After the nanosecond scheme had been tested, the femtosecond scheme was used. To get a general idea of what collection settings were needed, a quick aluminum plate test was conducted to set the initial collection settings. These settings, with a laser pulse energy of 4 mJ/pulse, a delay with respect to the laser of 100 ns along with a collection gate width of 1000 ns, a gain of 4, a center wavelength of 375 nm, 200 on CCD accumulations, 150 binned rows, and the 150 g/mm grating, were used for the initial aluminum propellant testing. For the aluminum sample, a bandpass filter of 335–610 nm was placed in front of the collection optics, which was removed for the other samples. When moving on to the other samples, the settings were tweaked by changing the gate width to 3000 ns and the

gain to 10. The center wavelengths used were 250 nm for copper, 280 nm for lead and lead stearate, and 315 nm for mercury chloride due to a high intensity, broad spectrum above 400 nm. The ICCD was saturated during the first lead stearate burn, so the gain was reduced to 6 for the subsequent burns.

After the detection testing in the femtosecond scheme, a concentration study similar to that with the nanosecond scheme was performed. Aluminum was once again used with settings of 1 on CCD accumulation per spectrum, a gain of 50, 150 vertical rows binned, a delay of 100 ns, and a gate width of 3000 ns. Peak intensities from the 396.15 nm Al line were recorded and then statistical analysis was performed.

4. RESULTS AND DISCUSSION

4.1. Nanosecond LIBS Detection Scheme

4.1.1. Solid Plate Experiments

Solid metal targets with known compositions of primarily Al, Cu, and Pb were ablated by the focused laser beam and the corresponding spectra were recorded to optimize the LIBS detection system and identify characteristic emission lines. Figure 12 shows the initial spectra collected from the plates after the Princeton Instruments IsoPlane 320/PI MAX 4 high-resolution spectrometer/ICCD combination was calibrated with a neon-argon wavelength calibration lamp. The data was taken with laser pulses of approximately 140 mJ/pulse. Compared with the NIST database, the peaks noted below closely align with tabulated values [68]. This study shows that the apparatus is detecting the spectral components correctly and therefore can be used with confidence.
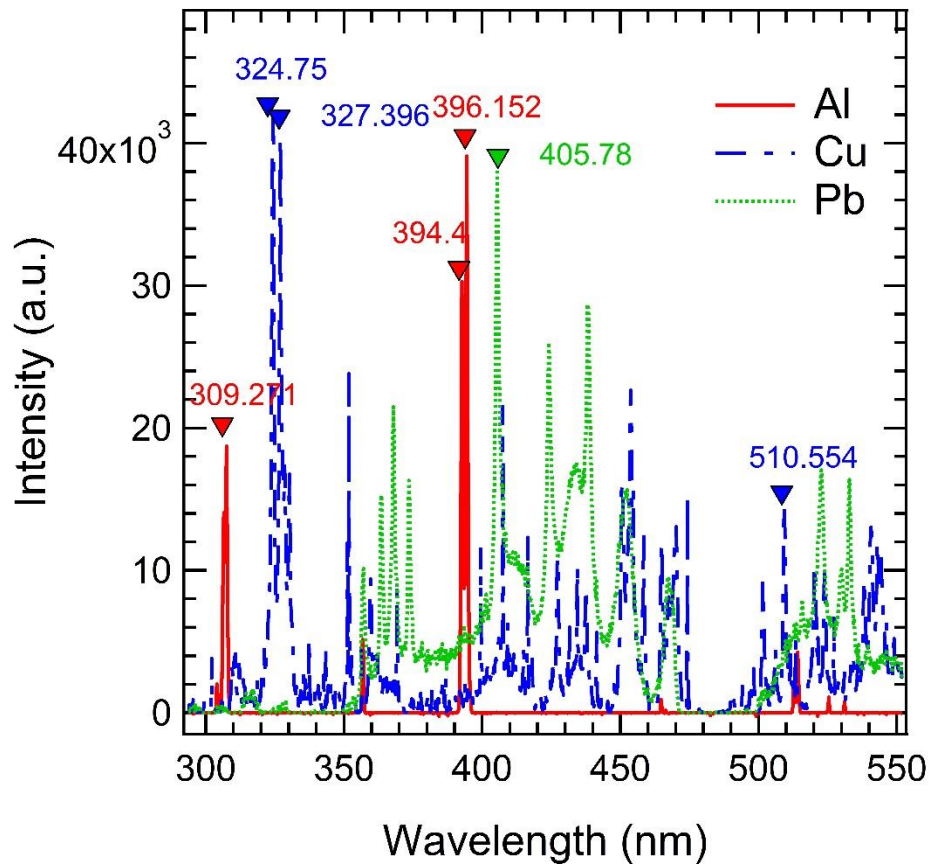
Figure 12. LIBS signals recorded using a high-resolution spectrometer/gated ICCD camera setup with a solid aluminum, copper, and lead plates. Spectra are red-shifted 0.4 nm to match the published values which are listed near each spectral peak.

After ensuring the spectrometer was finding the proper peaks corresponding to the metallic additives that will be present in the propellant strands, a laser energy study was conducted to select an energy level that produces an adequate SNR. Figure 13 shows the Al I 396.15-nm line's peak intensity versus the laser pulse energy, which were measured with a micro-spectrometer and an Ophir 20 W power meter, respectively. A linear trend between the two is observed. Although the overall intensity increases, the SNR may improve by limiting secondary reactions resulting from plasma-generated shockwaves by

using a lower laser pulse energy [69]. Therefore, a laser pulse energy of 100 mJ/pulse was selected because it provides an acceptable SNR while being relatively easy to achieve without significant air breakdown outside the probe region.
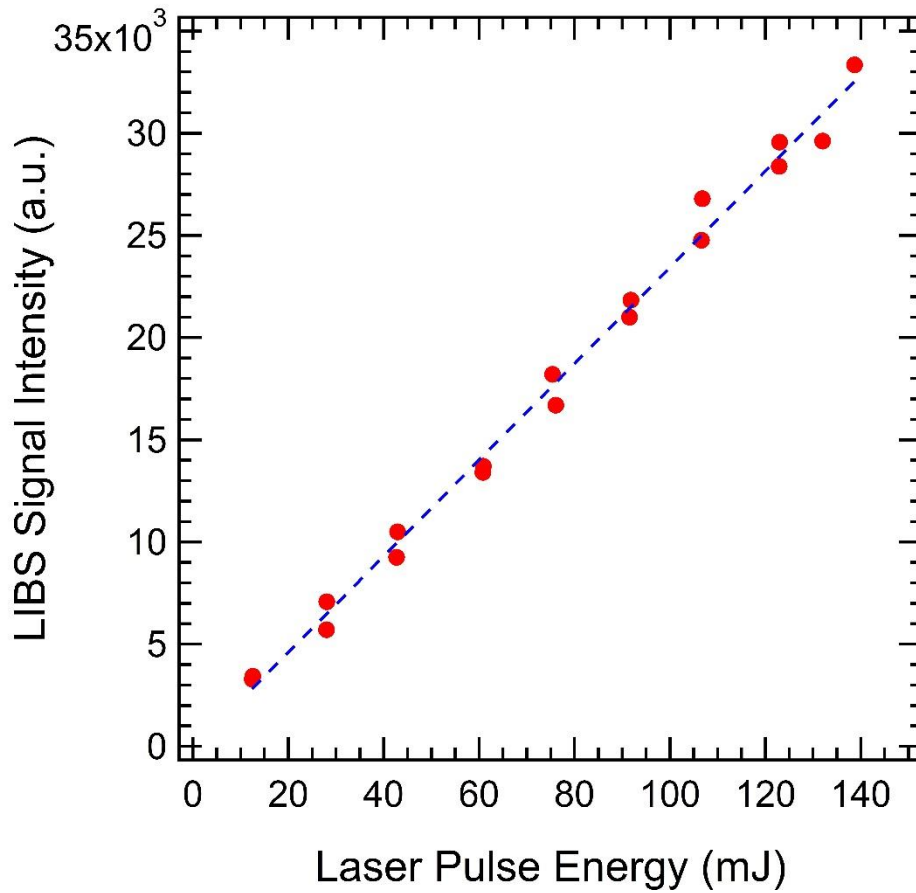
Figure 13. Laser energy dependence of the Al LIBS signal corresponding to the 396-nm emission line. The signals were recorded using the micro-spectrometer with 1000-ms integration time. Data from two repeated scans are shown.

The final preliminary study conducted was to investigate the plasma decay time. This was done by stepping the detection gate of the ICCD, which had a width of 20 ns,

through the incoming laser pulse ($t_{delay} = 0$ ns) until the signal was negligible ($t_{delay} \approx 3,000$ ns). If the data collection gate is set after the background continuum has decayed to a negligible level, the atomic emission signal becomes prominent and can be optimized, hence increasing SNR. If the delay is too long, however, the atomic emission signal also decreases. Figure 14 shows the aluminum emission signal of the 396.15 nm line versus the continuum emission, taken as an integrated average from 410-470 nm, as a function of gate delay. All collection settings were held constant, with a gain of 2, a gate width of 20 ns, 150 pixel rows binned vertically, and 2 on CCD accumulations per spectrum, except for gate delay during this study. Figure 15 shows the peak normalized plot of Figure 14, which emphasizes the point where the continuum emission is minimized. From the plots, it can be seen that the continuum emission decays to a negligible level after approximately 300 ns, so the optimal gate delay used for the rest of the experiments is 300 ns. Plasma decay studies for both Cu and Pb were also performed and lead to a similar result of 300 ns being the optimal delay.
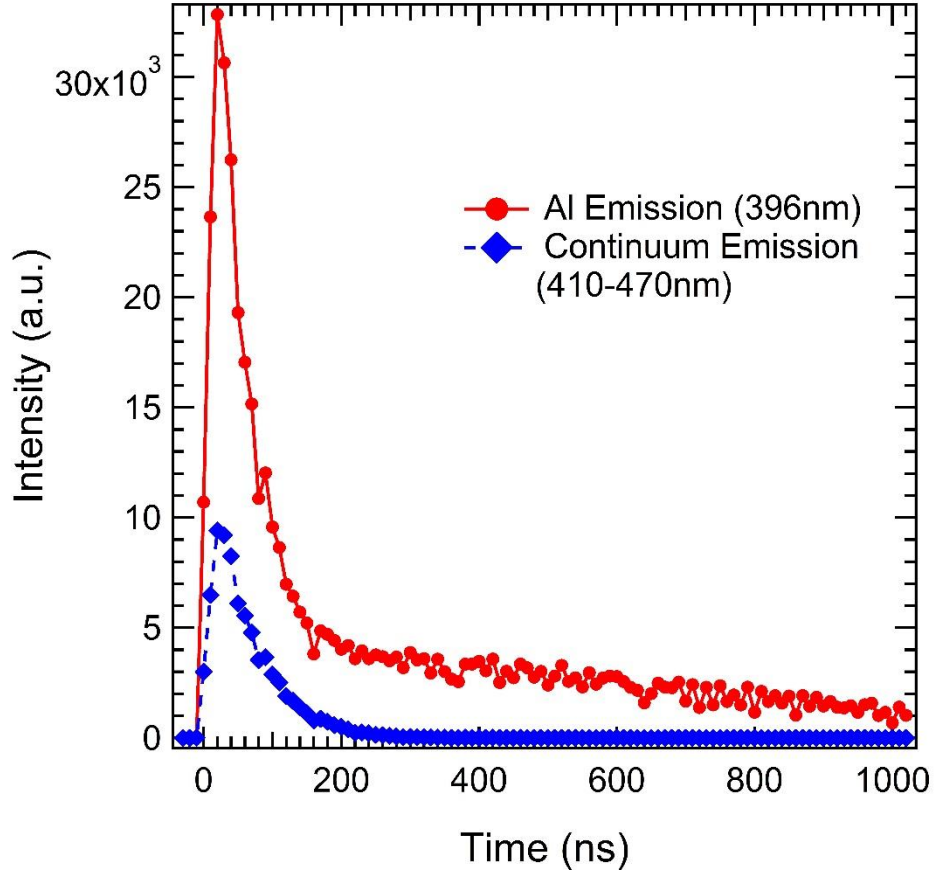
Figure 14. Aluminum emission signal of the 396-nm line and the continuum emission, as a function of ICCD gate delay.
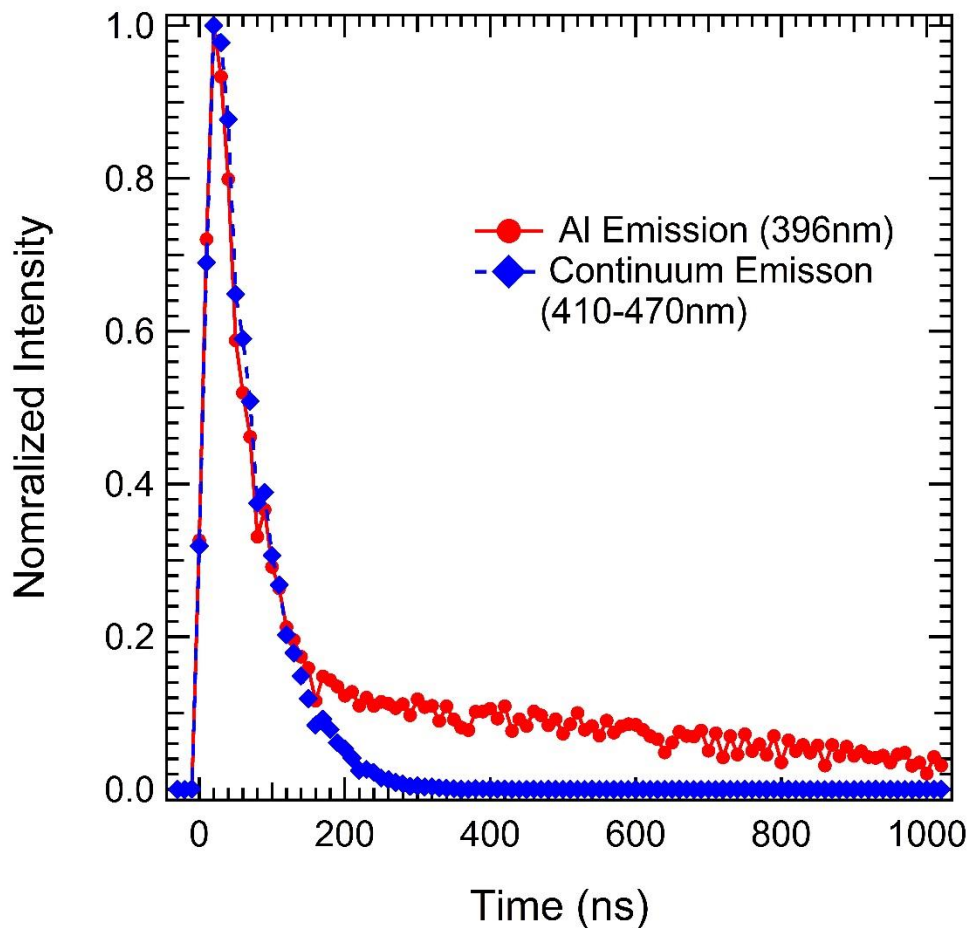
Figure 15. Normalized Al emission signal of the 396-nm line and continuum emission as a function of ICCD gate delay.

4.1.2. Propellant Strand Experiments

After the preliminary experiments of detecting signal, determining the proper energy level, and optimal gate delay are concluded, the propellant strand experiments can occur. The HTPB/AP strands provide a significant challenge compared to solid samples in that they only burn for a relatively short time (~20 seconds) and the number density of the metal particles in the hot gas-phase medium is extremely low.

44

The first task in the propellant strand experiments was simply to detect the metallic elements in the plume of the strands. Strands with 2%, 5%, and 20% by mass Cu, 5%, 10%, and 16% by mass Al, 16% by mass Pb, 16% Pb St, and 16% HgCl were all tested, but a signal was only detected in the 5%, 10%, and 16% Al samples. All the samples had particles with a mean diameter of 24 microns, except for the 2% Cu, which has a mean particle size of 5-10 nm. A spectrum of a 16% Al sample can be seen in Figure 16, with the 3 distinct peaks of 309, 358 and 396 nm. The spectra were collected using the high-resolution spectrometer/ICCD camera with a center wavelength of 400, a gain of 5, 5 on CCD accumulations, gate width of 1000-ns, and vertical binning of 150 rows. The laser pulse energy was set at 100 mJ/pulse.
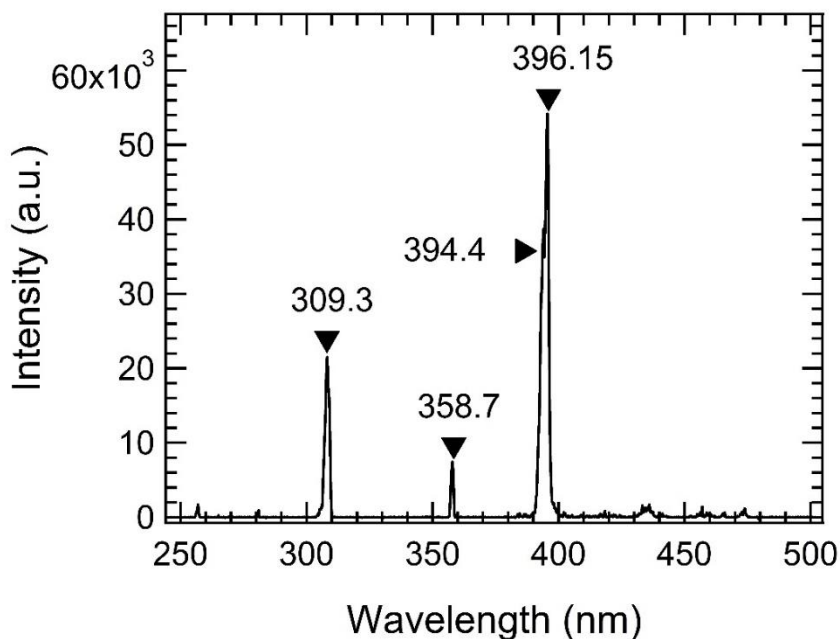
Figure 16. Aluminum emission spectrum recorded during a burning propellant strand. The peak values listed are from the NIST database. Experimental data has been red-shifted by approximately 0.5 nm to match with the NIST database.

45

After the aluminum signal was detected at the various mass percentages, a concentration study was performed to see if there was a correlation between mass percent present in the propellants and LIBS signal.

Commonly, LIBS signal is taken by averaging multiple spectra together, but with low number densities and non-homogeneous distribution of particles, such as in the propellant strand plume, this method does not work as well. Alvarez-Trujillo, et al. noted this problem and came up with an alternative statistical method for spectral data processing [70]. While the following concentration study didn't take the exact same approach as Alvarez-Trujillo, et al., a similar conclusion was drawn: averaging laser shots together would not work for this study. Initially, the data for this study was taken with the same settings as the general detection, namely with 5 on CCD accumulations per spectrum. This data can be seen in Figure 17, which shows the average peak intensity from the Al I 396.15 nm line versus the mass percent of aluminum present in the propellant strands. Due to particles passing through the plasma, not being hit by the plasma, different particle size, hitting multiple particles, etc., the intensity of the spectrum varies wildly between each individual laser shot. Due to this variation between the spectra, the standard deviation of the points is very large. It is worth noting that the sample number of each point in Figure 17 is relatively large, with each point consisting of 4 propellant strands, each with 130 frames, for a total of 520 frames per point, which corresponds to 2600 laser shots. While there is a slight increase in average intensity with increasing mass percent of aluminum present, the large standard deviation means that no reasonable conclusions can be drawn.
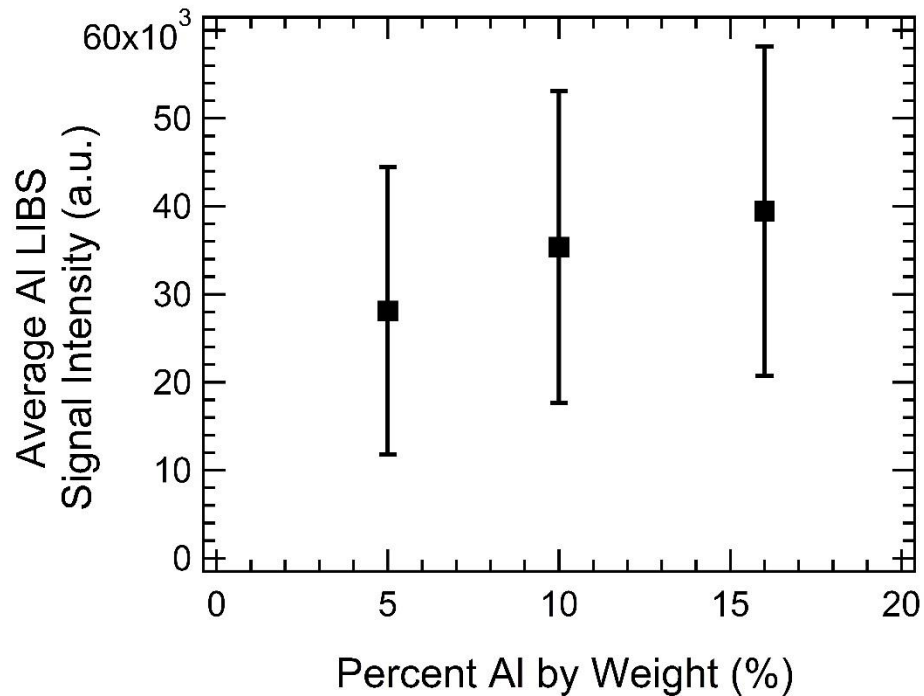
Figure 17. Average intensity of Al I 396.15 nm line versus weight percentage of aluminum present in the solid propellant strands. Error bars shown are the sample standard deviation calculated from the 520 signal acquisitions.

Therefore, instead of comparing average LIBS signal intensity between various mass percentages, a scheme of comparing a percentage of time seeing a LIBS signal was devised. The ICCD was set to collect data with 1 on-CCD accumulation, i.e. each spectrum is produced by a single laser shot. Figure 18 shows the peak intensity of Al I 396.15 nm line versus laser shot number for the full duration of 5 16%-Al-sample burns. The intensities of the strands have been offset vertically for clarity. The fluctuations in each sample correspond to the various size and number of aluminum particles drifting in and out of the laser probe volume. When no particles are present during the 10 Hz, 10 ns pulse time, the signal drops to a negligible level. Above this level, the intensity varies due to the

47

presence of either more particles or larger particles, which both correspond to a higher intensity. Taking only 100 shots from each sample, shown by the vertical lines at 50 and 150 laser shots, histograms can be generated that group similar intensity counts of the Al I 396.15-nm line together. An intensity count of 450 was determined to be the level at which there is a noticeable Al LIBS signal above and noise below. Figure 19, Figure 20, and Figure 21 show the resulting histograms for single samples of 5%, 10%, and 16% by mass Al samples, respectively. It is worth pointing out that these histograms seem to follow a Poisson distribution where the mean is shifting towards the right. For the samples shown, the sample mean of each is 2.98, 4.24, and 5.44, and the sample standard deviation is 1.70, 2.53, and 3.92 for 5%, 10%, and 16% respectively.

The blue, hashed columns correspond to intensity levels where no LIBS signal is detected, and the red columns correspond to intensity counts where LIBS signal is noticeable. In Figure 19, which shows a histogram for a 5% Al propellant strand, the number of shots seeing no signal is fairly large – 56 of the 100 laser shots compared to 44 seeing signal. Looking at the 10% and 16% histograms in Figure 20 and Figure 21, the columns seeing no signal, which again are the blue columns on the left, decrease and redistribute into the red, right columns that are representing seeing signal. For these two particular samples, the signal was detected in 71 and 79 of the 100 shots respectively. It is also worth noting that higher intensities seemed to occur more often in the 16% sample, which can be seen when comparing Figure 20 and Figure 21. This might be due to more particles being in the plasma, probe volume. This is somewhat consistent with Figure 17, which shows an increase in detected intensity with mass percent.

48
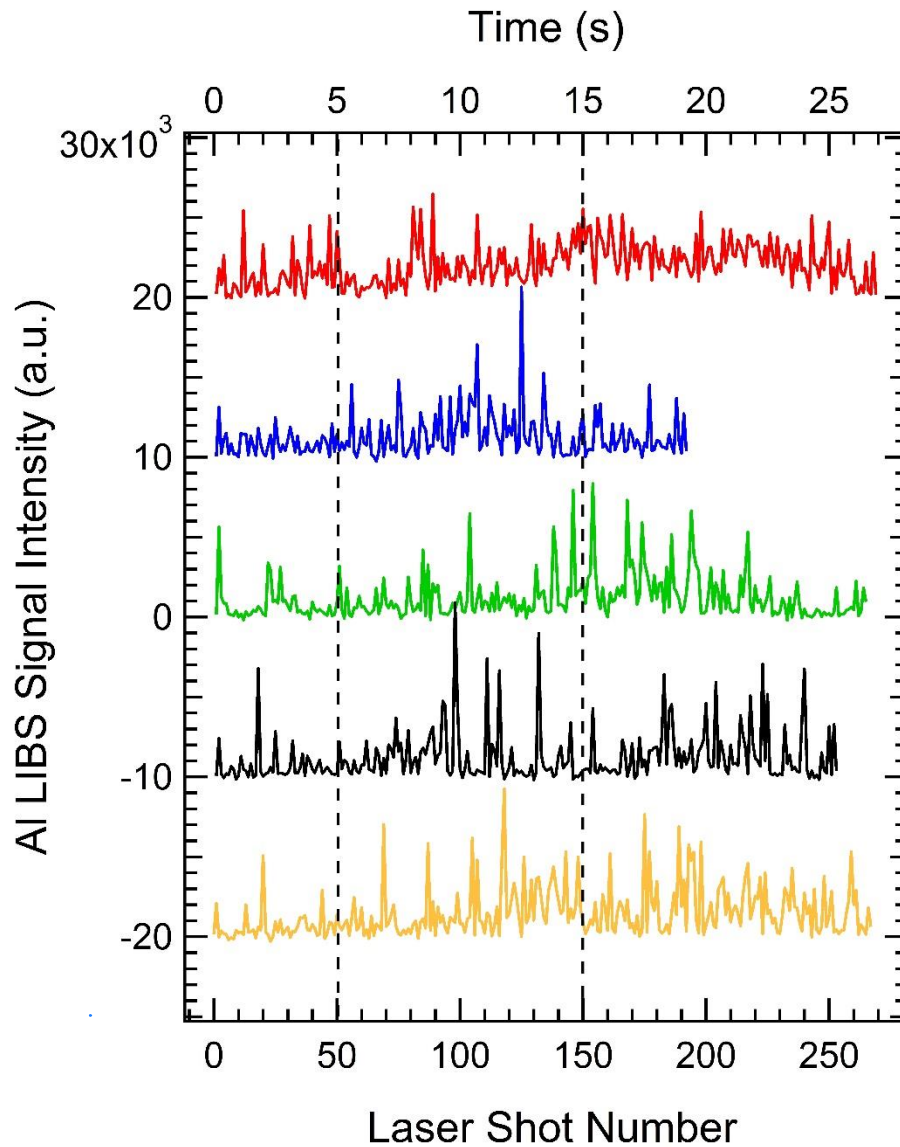
Figure 18. Intensity counts versus laser shot number of 5 full duration burns of 16% aluminum propellant strands. The vertical dotted lines represent the region of 100 laser shots taken from this batch for further analysis. The Al LIBS signal value is extracted from the 396.15 nm peak value.
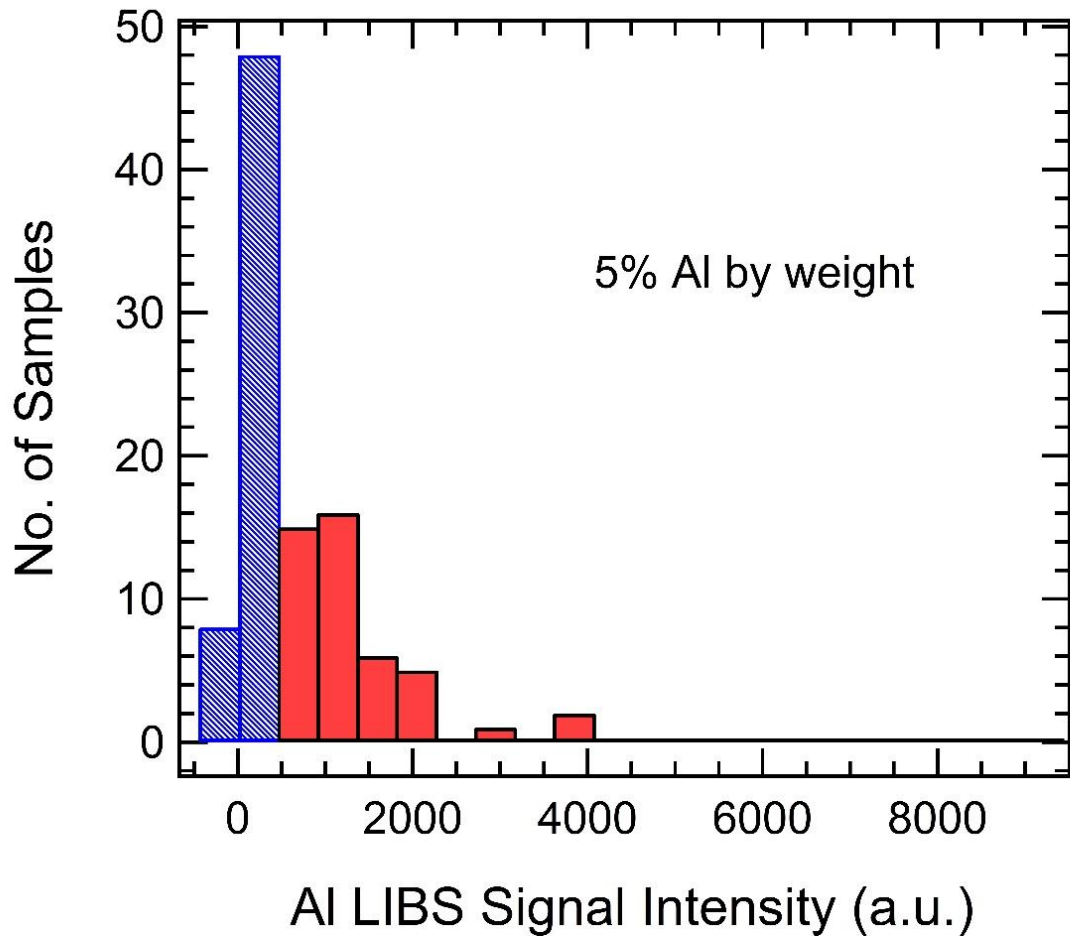
Figure 19. Histogram showing the number of samples with sufficient intensity counts shown in red and below detection limit (i.e. noise) shown in blue for 100 laser pulses during a 5% propellant strand burn.
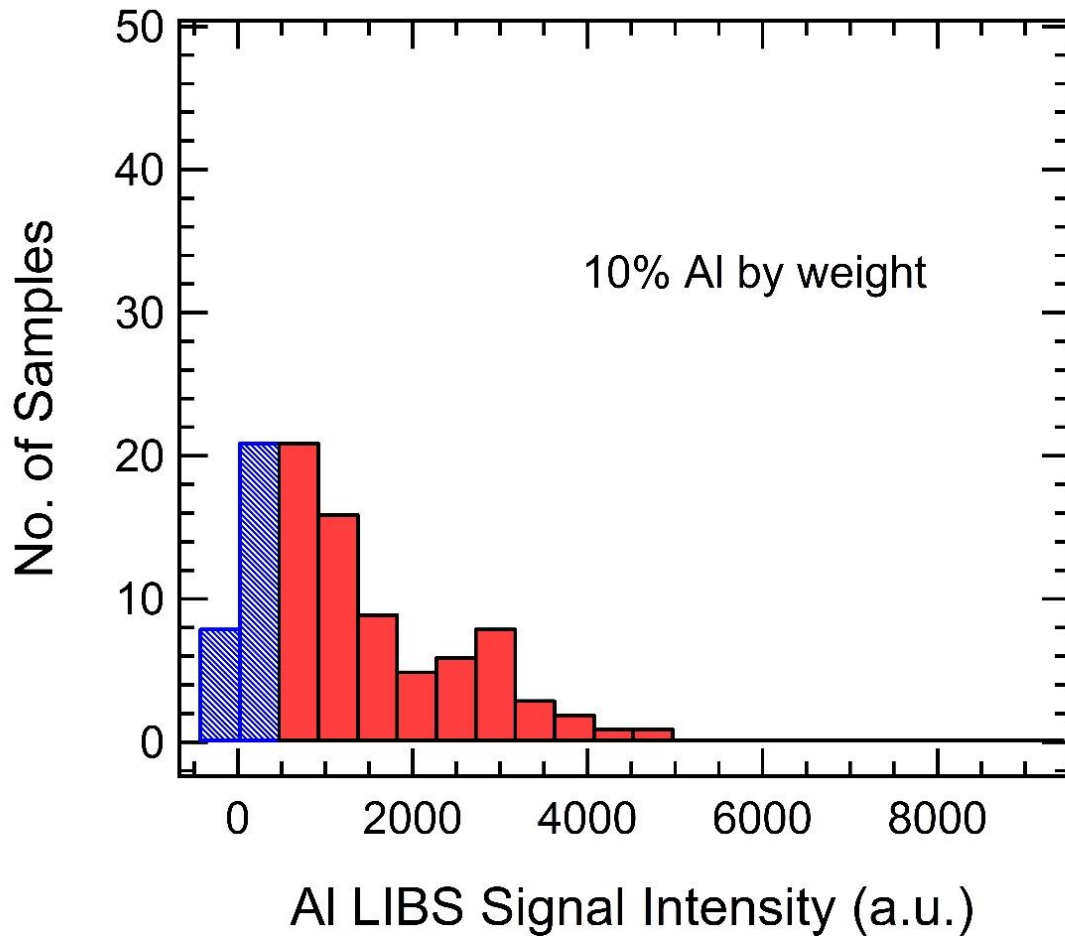
Figure 20. Histogram showing the number of samples with sufficient intensity counts shown in red and below detection limit (i.e. noise) shown in blue for 100 laser pulses during a 10% propellant strand burn.
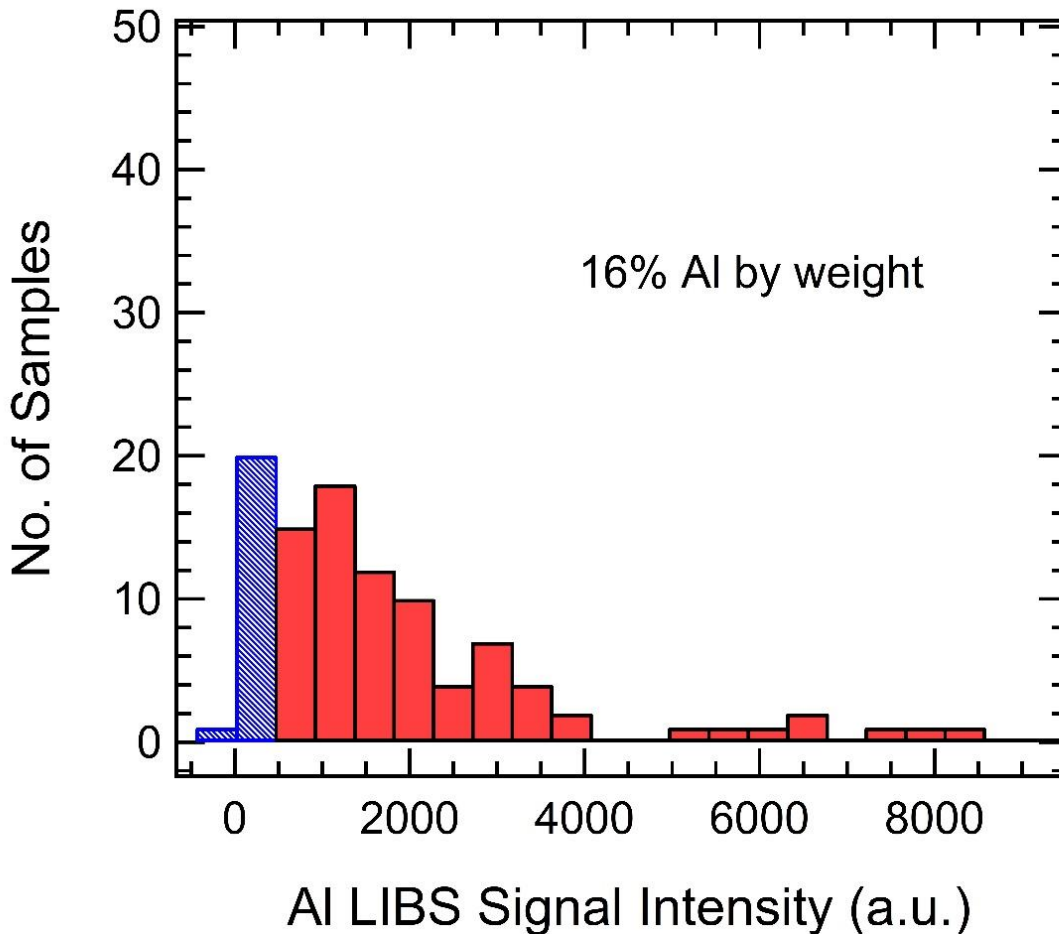
Figure 21. Histogram showing the number of samples with sufficient intensity counts shown in red and below detection limit (i.e. noise) shown in blue for 100 laser pulses during a 16% propellant strand burn.

Taking the average intensities for 5 samples, which corresponds to 500 laser shots, for each of the 5%, 10%, and 16% Al strands and plotting them versus their respective mass percentages, as shown in Figure 22, there is generally an upward trend. This once again shows that as the mass percentage of Al increases in the propellant, the LIBS signal is seen a higher percent of the time, i.e. detection percentage increases, though not in a linear fashion. The average percentages of time seeing signal for the 10% and 16%

samples are actually within a few tenths of a percent of each other (79.0% versus 79.6%

respectively), while the 5% is lower at 48.4%. This is likely due to the system starting to

behave more like a homogeneous mixture in the 10% and 16% samples. Also, comparing

this plot in Figure 22 to Figure 17, the standard deviation is much lower, therefore the

single shot method of taking data gives a more meaningful result from which conclusions

can be drawn from with more confidence.
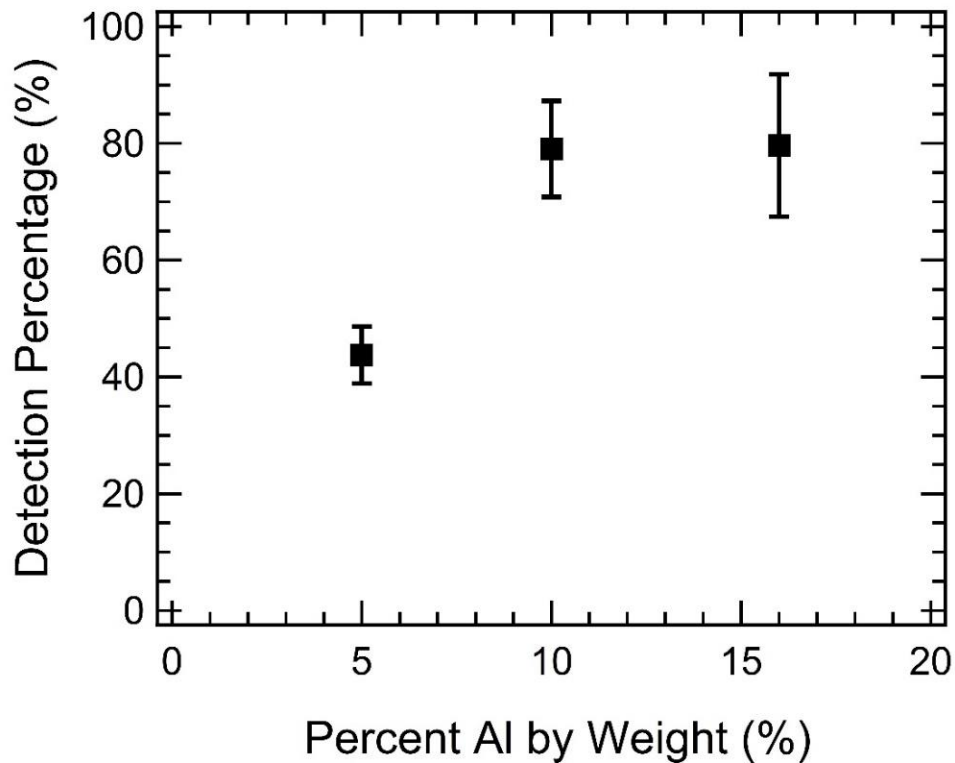
Figure 22. Plot of percentage of time seeing LIBS signal versus the aluminum concentration in the propellant strands. Error bars shown are the sample standard deviation calculated from the 500 acquisitions, each containing 1 on-chip accumulation.

For the convenience of the reader, all the propellant strands tested in the nanosecond scheme are listed in Table 3. As a reminder, only the 5%, 10%, and 16% Al by mass samples were able to be detected in the gas phase exhaust region of the HTPB/AP solid propellant strands. The original hypothesis at the end of the nanosecond testing was that the reason the other propellant strands of Cu, Pb, PbSt, and HgCl were not detected was because they simply did not have as many metallic particles flying off the propellant strand due to differences in atomic mass, which is shown in the left column of Table 3. While this may be a partial reason the LIBS signal was not detected, a 20% Cu was tested afterwards to see if the hypothesis would hold. According to the original hypothesis, since 20% Cu lies above even 10% Al in the relative to 16% Al column, it should be able to be detected. This actually turned out to not be true. A LIBS signal of Cu was not able to be detected in the flame using the 20% Cu sample. This observation is further discussed in the following section, where high-repetition-rate LIBS experiments were performed using a fs-laser system.

Table 3. Summary of all propellants strands tested using the ns LIBS scheme. Given in the last column are the portions of metallic particles relative to 16% Al—calculated based on the atomic mass of each metal—allowing for a better comparison between different samples.

Additive	Particle Size	% Additive (by mass)	% Metal (by mass)	Particles Relative to 16% Al
Al	μm	16	16	1
Al	μm/nm	16	16	1
Al	μm	10	10	0.63
Al	μm	5	5	0.31
Al	μm	1.5	1.5	0.09
Pb	μm	16	16	0.13
$(C_{17}H_{35}COO)_2Pb$	μm	16	4.28	0.01
Cu	nm	2	2	0.05
Cu	nm	5	5	0.13
Hg_2Cl_2	μm	16	13.6	0.05
Cu	μm	20	20	0.67

4.2. Femtosecond LIBS Detection Scheme

After the nanosecond scheme testing concluded, the femtosecond testing began. Femtosecond LIBS has advantages over nanosecond LIBS in that it requires a shorter delay time, if a delay time is required at all, due to the plasma not interacting with the laser pulse. Femtosecond lasers also typically have a higher repetition rate. For example, in these schemes, the nanosecond fires 10 times a second and needs a gate delay of 300 ns, while the femtosecond fires 1000 times a second and was gated at 100 ns after the pulse but can go lower. Since the nanosecond only detected aluminum, the experimenters were hopeful these advantages of femtosecond LIBS would help detect the other additives of copper, lead, lead stearate, and mercury chloride.

The first test conducted was with the 16% by mass aluminum propellant samples. The gate was delayed by 100 ns, which was set with a quick plate experiment to find where the continuum background noise dropped to approximately zero. The other collection settings can be found in the experimental section. Figure 23 shows a time series of the two aluminum propellant strands burned. Each frame number point has a spectrum associated with it. Each spectrum is an accumulation of 200 laser shots on the CCD before reading off. Although the laser runs at 1 kHz, the ICCD with the collection settings could only operate at 4.88 frames per second, which is shown by the time stamp on the top x-axis. The samples both had approximately 20- to 25-second burn durations, depending on their initial cut length, which varies slightly from sample to sample. The intensity plotted is pulled from the peak intensity of the 396.15 nm line. The fluctuations seen in this signal are not the same as the fluctuations in Figure 18, which was the nanosecond concentration

study showing 5 full duration burns for 5 16%-aluminum propellant strands. The fluctuations in Figure 18 came from aluminum particles floating in and out of the probe volume. Since the laser only fired 10 times a second, particles were only hit every now and then (~80% of the time for the 16% sample). The fluctuations in the femtosecond data are most likely not from missing particles, since the laser is operating 100 more times a second. Since the laser has a much higher repetition rate, the likelihood of hitting particles increases massively. The fluctuations in Figure 23 are likely from the varying amount of aluminum vertically in the cross section of the propellant strands resulting from mixing. Although the overall concentration of the propellant strand is 16% aluminum, there is likely some variation in the actual concentration of the aluminum vertically as the strand burns. Also worth noting is that the signal fluctuation does not seem to have a pattern. It increases and decreases randomly. This shows that the height above the propellant strand that the laser probe is, since the height is fixed and the propellant strand burns down increasing the distance from the surface of the propellant strand to the plasma, has no significant effect as long as the laser focal spot is in the plume.
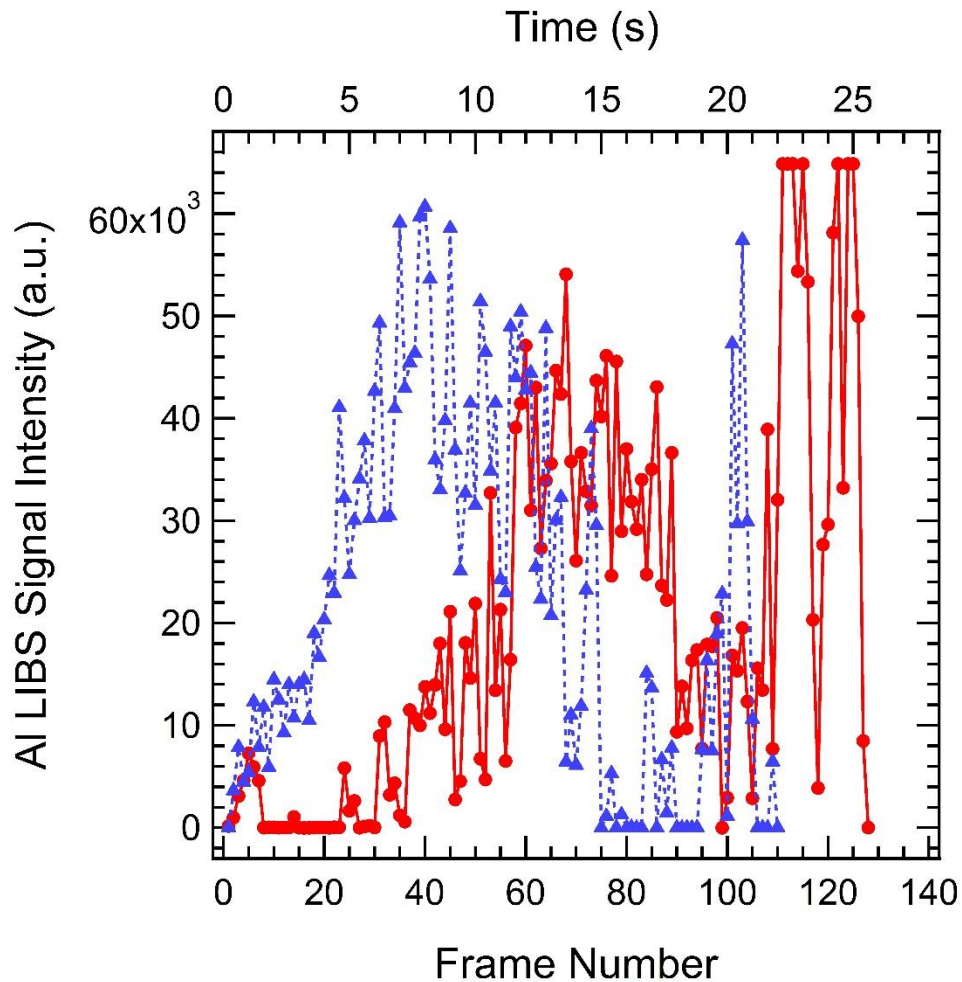
Figure 23. Time series showing two aluminum strand burns. The peak intensity plotted is extracted from the 396.15-nm line. Each data point contains 200 on-CCD accumulations or laser pulses. The points are distinct frames, not a continuous signal. The lines have been added for clarification of the trend.

Figure 24 shows an aluminum spectrum pulled from the 103rd frame of the strand plotted in blue in Figure 23. It is important to note that a bandpass filter of 335-610nm from Thorlabs was used in front of the collection optic for the aluminum testing, so the only apparent peaks are at 394 and 396 nm with the 309nm line being eliminated and the 358nm line being diminished. In Figure 24, it is also apparent that the time delay of 100

ns is sufficient, as there is no large continuum background from 410 to 470 nm as seen in the plasma decay study. While aluminum was detected with the femtosecond scheme, this is not a new result from the nanosecond scheme. Nevertheless, there are advantages of using a higher repetition rate, which leads to a better chance of detecting the metallic particles of aluminum. The real advantages are apparent when looking at the other metallic additives of copper, lead, lead stearate, and mercury chloride, which are discussed in the following sections.
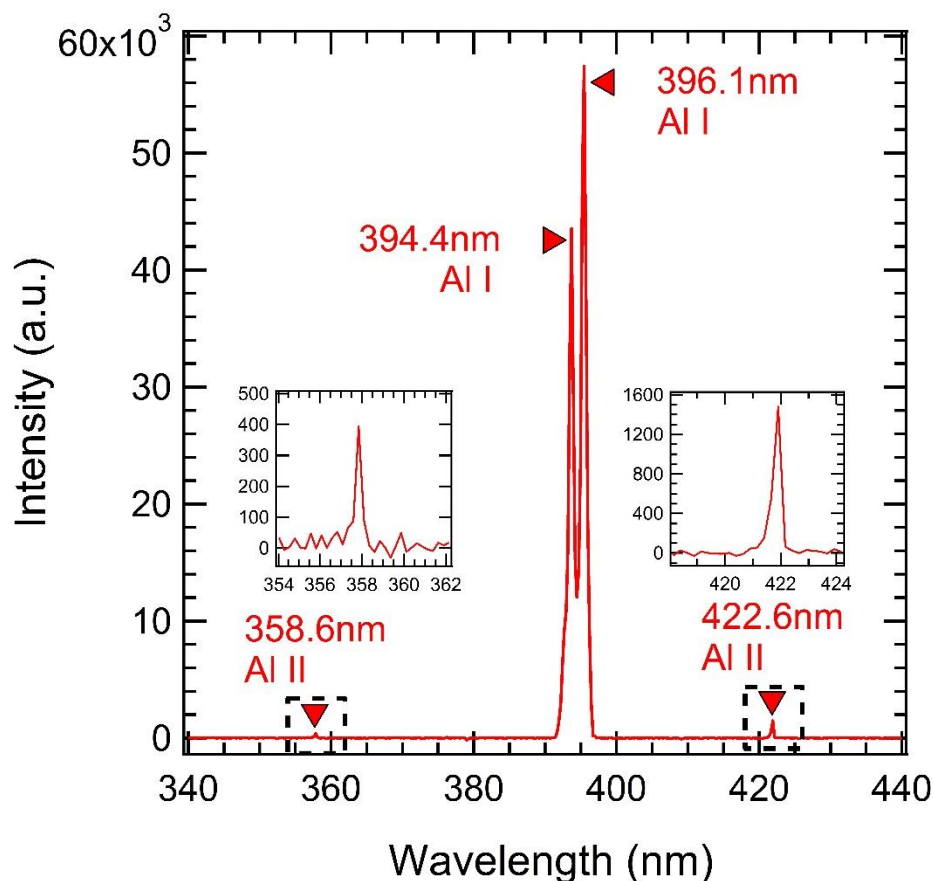
Figure 24. **A sample Al spectrum taken from frame 103 of the strand plotted in blue in Fig. 23 above. The regions corresponding to lower intensity peaks have been replotted in expanded vertical scale in the insets for clarity. The peak values listed are from the NIST database. Experimental wavelengths have been red shifted 0.7 nm to match with NIST database.**

Moving from the aluminum to the copper samples, three mass concentrations of copper present in the propellant strands were tested: 20%, 5%, and 2%. The 20% and 5% contained copper particles with a mean diameter of 24 µm, while the 2% samples had particles with a mean diameter of 7.5 nm. All three concentrations were detected, which can be seen in the copper-doped propellant burn time series in Figure 25. This shows that the particle sizing, whether micron or nanometer, doesn't necessarily affect detecting the LIBS signal since it was able to detect both the micrometer and nanometer particles. It is worth noting though, that the nanometer particles will sometimes agglomerate on the surface before being ejected, leading to particles of approximately micron size. Figure 25 shows the 4 copper strands burned, one of 20%, one of 5%, and two of the 2% copper. Once again, fluctuations are seen in the signal intensity, which this time is pulled from the 324.75 nm line of copper. Again, each frame represents a spectrum that has 200 laser shots accumulated on the CCD chip before reading off. The strands all have about a 20 second burn duration. Once again, there seems to be no real trend in these fluctuations, no tailing off near the end of the burn, etc. It also seems that the intensity scales with the percentage of copper present in the propellants. The lines have been offset for clarity, but the highest percentage of copper at 20% seems to have the highest intensity, with 5% below that, and the 2% copper samples having the lowest intensity. While more samples would need to be tested to confirm this trend, it aligns with what was seen in the nanosecond scheme with the aluminum single shot samples.

Figure 25. Time series for all copper strands tested at various concentrations of 2%, 5%, and 20%. The peak intensity plotted is extracted from the 324.75 nm line. Each data point represents 200 on-CCD accumulations or laser shots. The points are distinct frames, not a continuous signal. The lines have been added for clarification of the trend.
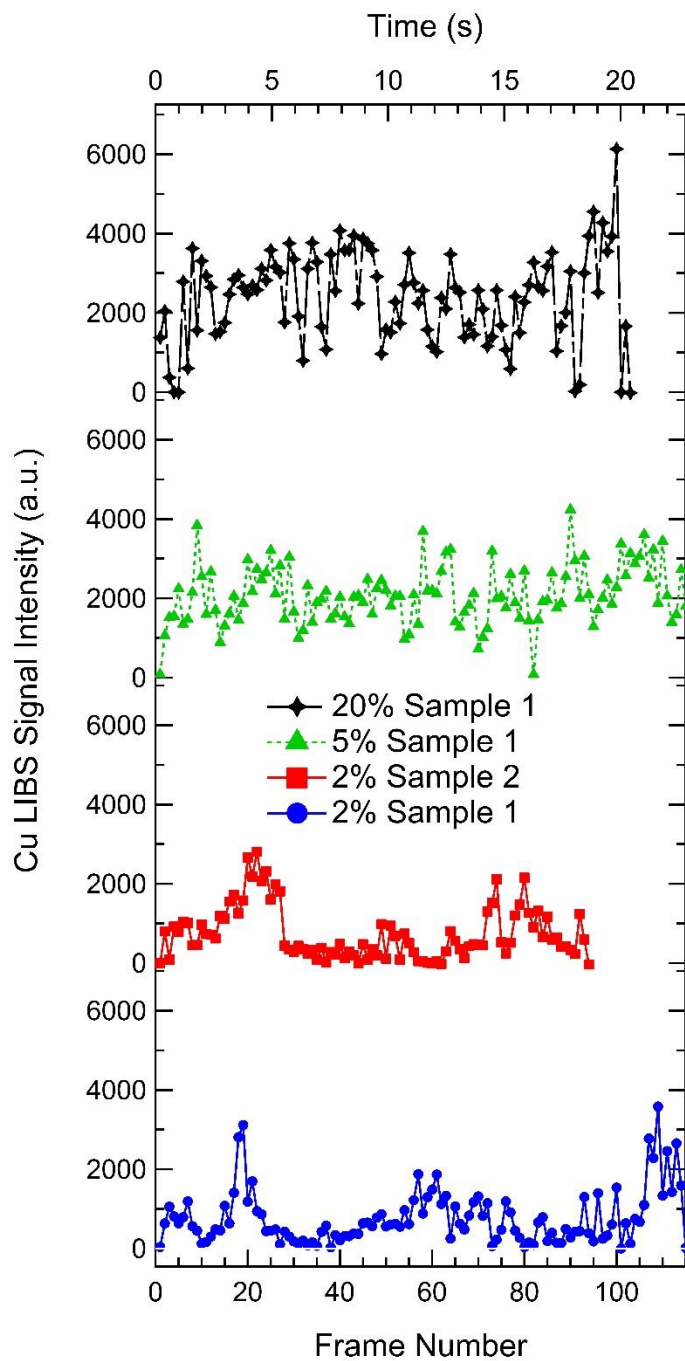
61

Figure 26 shows the copper spectrum from the 100th frame of the 20% copper sample, which corresponds to the highest intensity detected. The bandpass filter had been removed for this test so the major copper peaks at 324 and 327 nm could be seen. Furthermore, the center wavelength was changed from 375 nm in the aluminum samples to 250 nm, along with some other collection settings, which can be found in the experimental section. The intensity count of the copper is the lowest of all additives tested, although, comparing with the aluminum isn't an apples-to-apples comparison due to these changes. In fact, the changes would be expected to increase the measured intensity count since the gain was increased from 4 to 10 and the gate width was increased from 1 μs to 3 μs. The rest of the additives' intensities can be compared directly though, as the collection settings remained constant from copper onward to the lead, lead stearate, and mercury chloride.
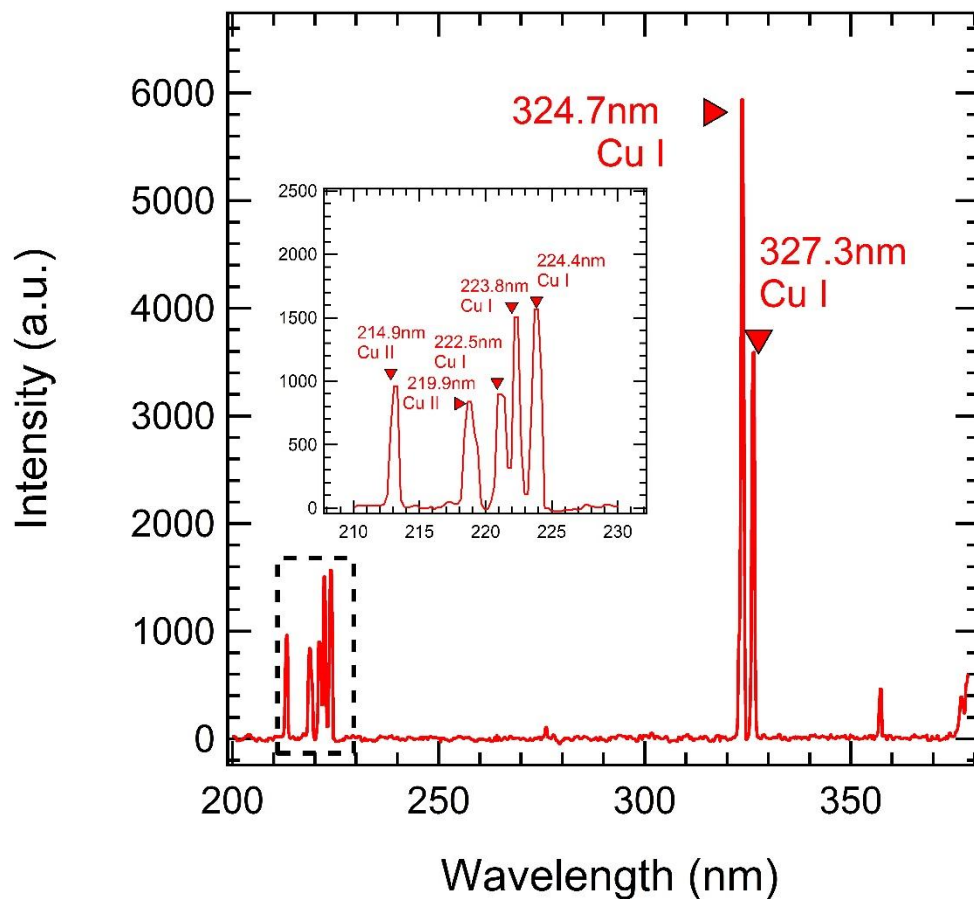
Figure 26. A sample Cu spectrum taken from frame 100 of the 20% copper strand burn plotted in black in Fig. 25 above. The region around 220 nm has been replotted in expanded vertical and horizontal scale in the inset for clarity. The peak values listed are from the NIST database. Experimental wavelengths have been red shifted 0.7 nm to match with NIST database.

The lead samples were the next to be tested for detection in the gas phase exhaust plume of the propellants. Figure 27 shows the time series of the two 16% lead samples burned, each lasting approximately 15-20 seconds depending on initial length. The intensity plotted comes from the 405.78 nm peak of lead, and, once again, each point represents a spectrum, each with 200 laser shots. Once again, fluctuations in the signal seem to be random. Since there are 200 laser shots, it seems as if the fluctuations must

come from the varying vertical concentration of added metallic particles as the strand

burns down.
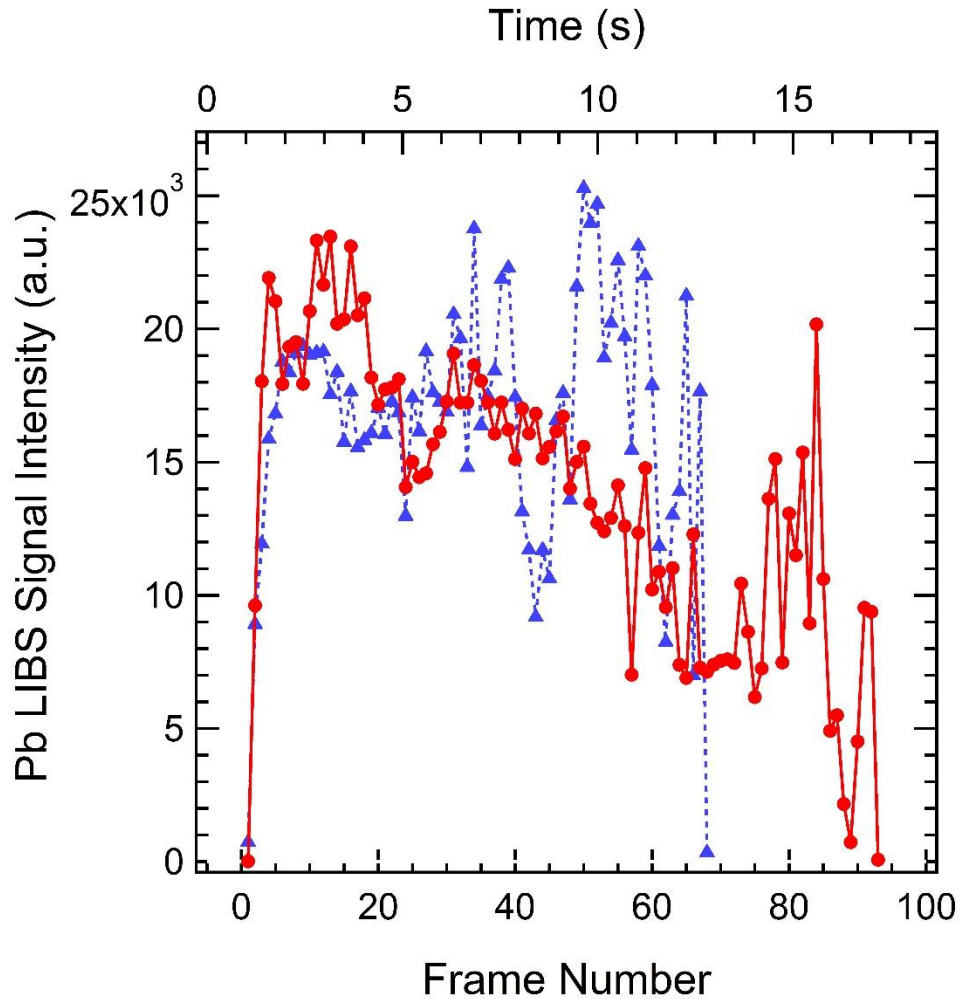
Figure 27. Time series from two lead propellant strand burns. The peak intensity plotted is pulled from the 405.78 nm line. The points are distinct frames, not a continuous signal. The lines have been added for clarification of the trend. Each data point represents 200 on-CCD accumulations or laser shots.

The lead spectrum from the 50th frame of the propellant strand burn plotted in blue in Figure 27 is plotted in Figure 28, with a new center wavelength of 280 nm. In the spectrum, the 405-nm peak is apparent, with some other smaller lead peaks. Here, it can

be shown that the lead signal, along with the rest of the additives, is much higher than that

of the copper, being approximately 4 to 5 times more intense.
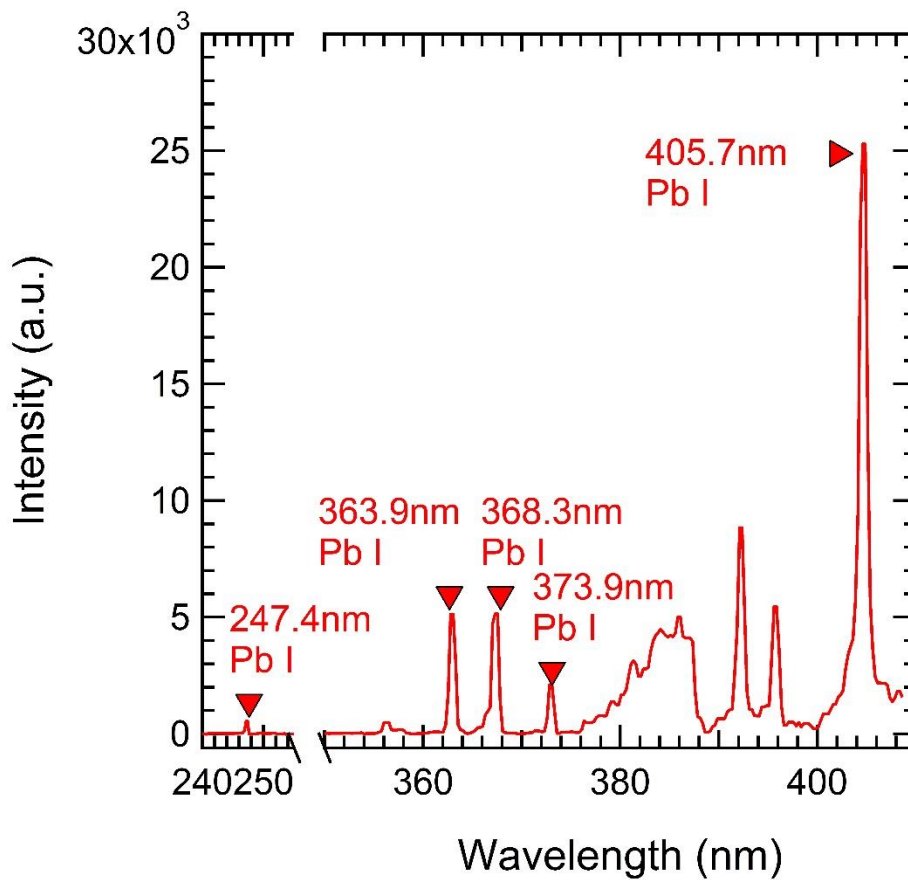
Figure 28. Sample spectrum of Pb taken from frame 50 of the strand plotted in blue above. The peak values listed are from the NIST database. Experimental data has been red shifted 0.7 nm to match.

The next propellant tested was the lead stearate, for which the time series of two

test runs is plotted in Figure 29. It is worth noting that the lead stearate, while having the

same mass concentration as the lead at 16%, has a much lower portion of actual lead. This

is due to the stearate being a long, heavy hydrocarbon chain. The overall molecular mass

of lead stearate is 741.2 g/mol, with only 207.2 g/mol being lead. Therefore, the actual

concentration of lead present in the propellant strands is only about a fourth of the lead. When compared to the 16% aluminum propellant, it is only about 0.9% as many metallic particles due to the great difference in mass. Because of this massive change, the original hypothesis was that lead stearate would be the hardest additive to detect. This was contrary to what was observed. Although only having a fourth of the lead content compared to the pure lead additive, the lead stearate actually had a much more intense signal than the lead, as well as HgCl and Cu samples. In the original burn, which is the blue line plotted in Figure 29, the ICCD camera was saturated, so the gain had to be reduced from 10 to 6 for the second run. Also, another strange occurrence happened with lead stearate: the sample extinguished itself in the middle of the burn. Due to this extinguishing, only one strand was burned. If the total time of the burn was added from the two lines in Figure 29, it would come to about 35 seconds, which is twice as long as any other propellant. From this, it can be deducted that PbSt can be classified as a fire retardant.
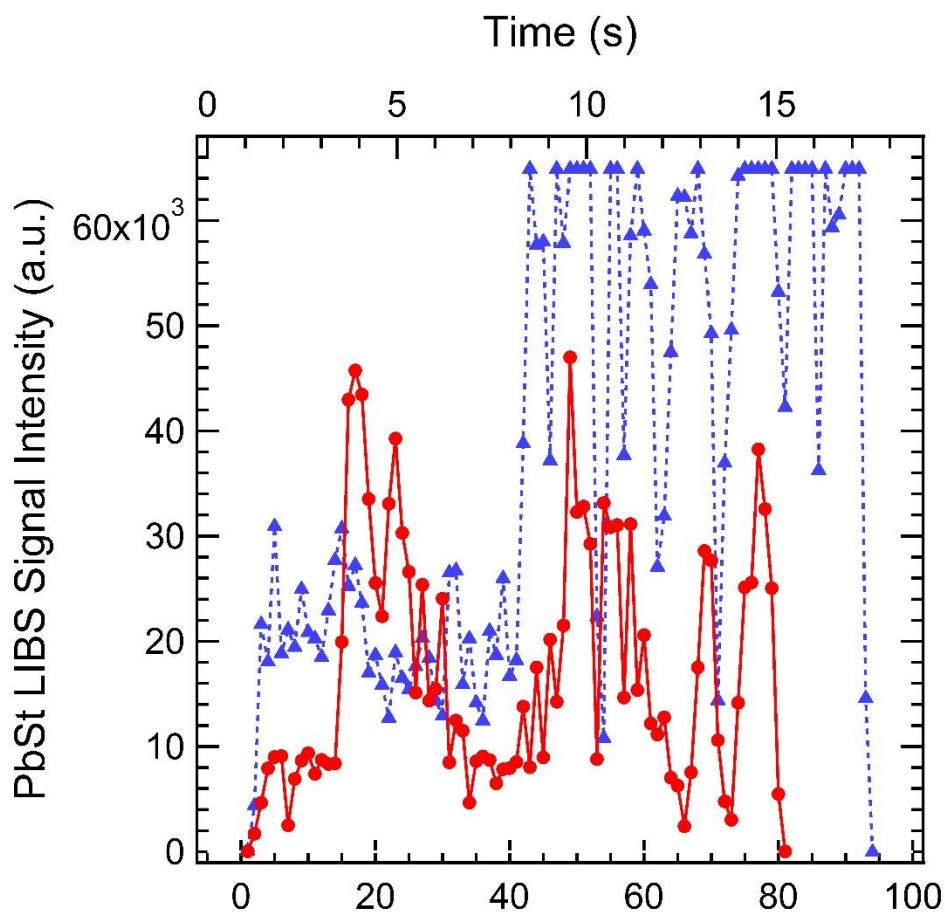
Figure 29. Time series of ns-LIBS signal of Pb extracted from two lead stearate propellant strands. The peak intensity plotted is extracted from the 405.78 nm line. Each data point represents 200 on-CCD accumulations or laser shots. The first strand, plotted in blue, had the same settings as the other burns, but it partially saturated the ICCD camera. Therefore, on the second burn, plotted in red, the gain was reduced from 10 to 6. The points are distinct frames, not a continuous signal. The lines have been added for clarification of the trend.

Figure 30, which shows a spectrum of lead stearate, further shows that the intensity increases from the pure lead 16% propellant. The 405-nm peak is about 1.5 times as intense, while having a lower gain of 6 compared to the gain of 10 in the original pure lead

sample. Many more peaks are apparent in the lead stearate spectrum due to this increase in intensity. The exact mechanism for this increase in intensity is still uncertain, but it can be deducted that lead stearate is easier to detect compared to lead in the femtosecond scheme.
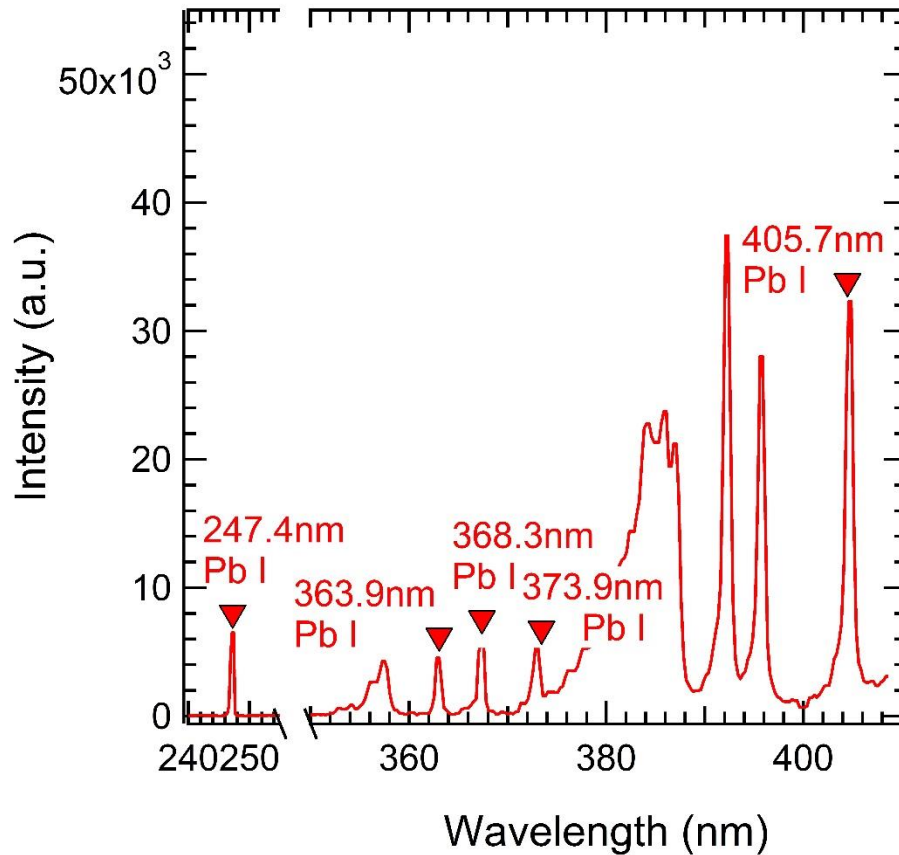
Figure 30. A sample spectrum from PbSt propellant strand burn. This specific spectrum is from the second strand's 50th frame. The peak values listed are from the NIST database. Experimental data has been red shifted 0.7 nm to match with NIST values.

The last type of propellant strand tested was the one with 16% mercury chloride added. The time series of the two propellant strands burned can be seen in Figure 31. Once

again, the fluctuations seem to be random, with no real trend. The intensity plotted is from the 435.83-nm line of mercury.
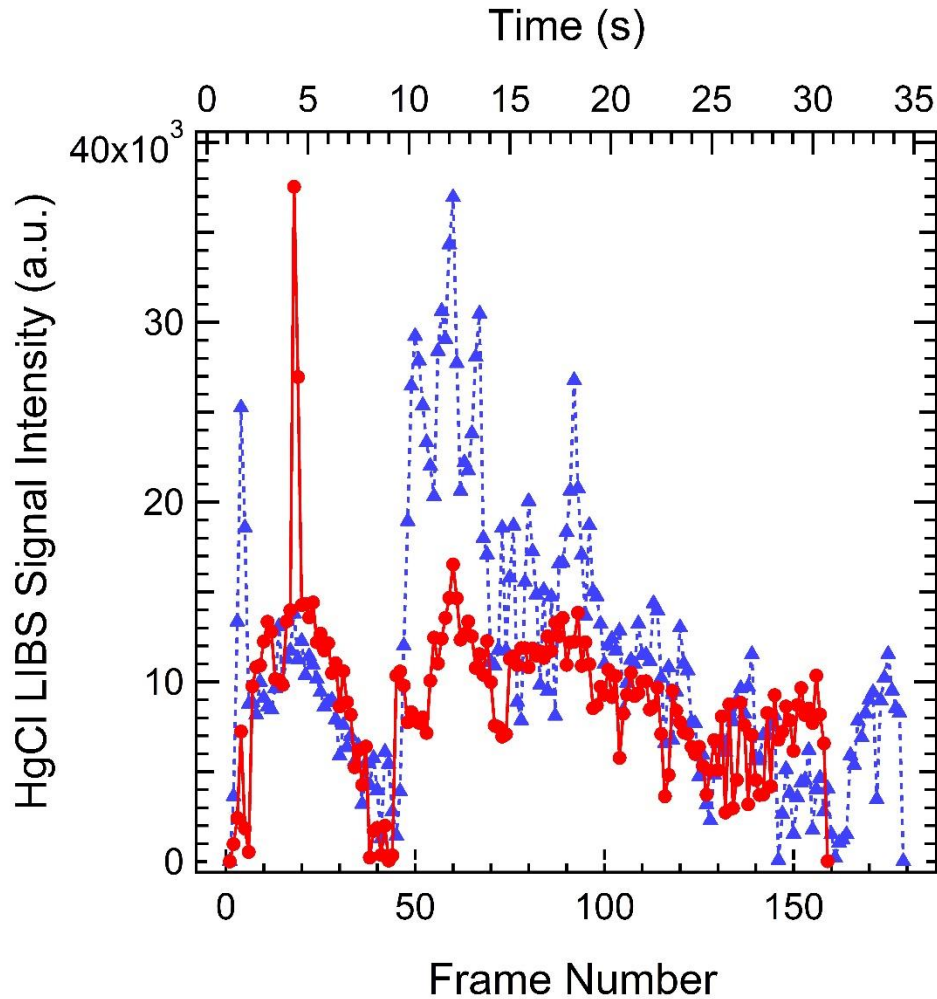
Figure 31. Time series of two HgCl propellant strand burns. The peak intensity plotted is pulled from the 435.83-nm line. Each data point represents 200 on-CCD accumulations or laser shots. The points are distinct frames, not a continuous signal. The lines have been added for clarification of the trend.

Figure 32 shows the HgCl spectrum pulled from the 18th frame of the propellant strand plotted in blue above. The 435.83-nm line of mercury is apparent along with some other minor mercury peaks, such as the peak at 365 nm.
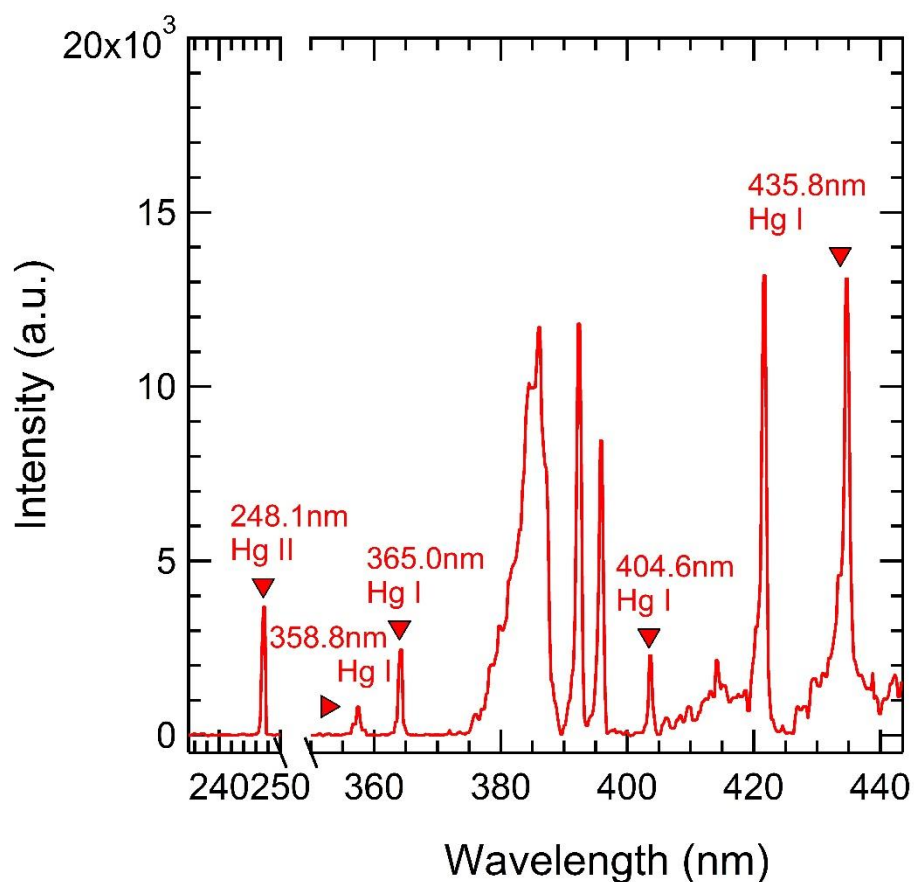
Figure 32. A sample spectrum of HgCl extracted from the 18th frame of the strand plotted in blue Fig. 31 above. The peak values listed are from the NIST database. Experimental data has been red shifted 0.7 nm to match.

Now that all the metallic additives were successfully detected in the gas-phase exhaust region of these solid propellant strands with the femtosecond scheme, an aluminum concentration test similar to that conducted in the nanosecond setup was performed. Instead of collecting 200 on CCD accumulations, only 1 accumulation per spectrum was used, along with other collection settings discussed in the experimental section. This allows for a statistical analysis of whether the LIBS signal is being detected. It is worth noting that although the laser operates at 1 kHz, the ICCD camera with the

specified collection settings was only able to record at 167 frames per second for this study, which is represented in the plots below. The samples burned were 5%, 10%, and 16% aluminum samples, for which the full duration burn, single shot data can be seen in Figure 33, Figure 34, and Figure 35, respectively. Initially looking at these plots, it appears that 10% and 16% have more shots with a LIBS signal than the 5%, which falls in line with the nanosecond scheme concentration study.
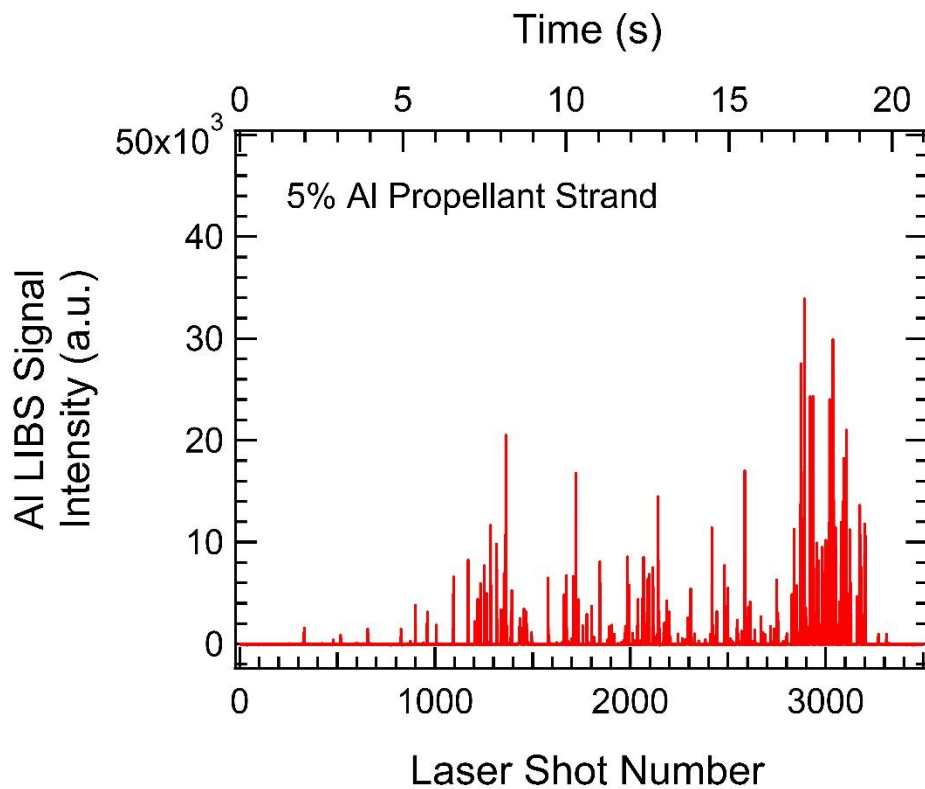
Figure 33. Single-laser-shot data of Al LIBS signal for the entire duration the burn, recorded in 5% Al propellant strand shown as a function of the laser shot number. The Al LIBS signal is extracted from the peak intensity of the 396-nm line.
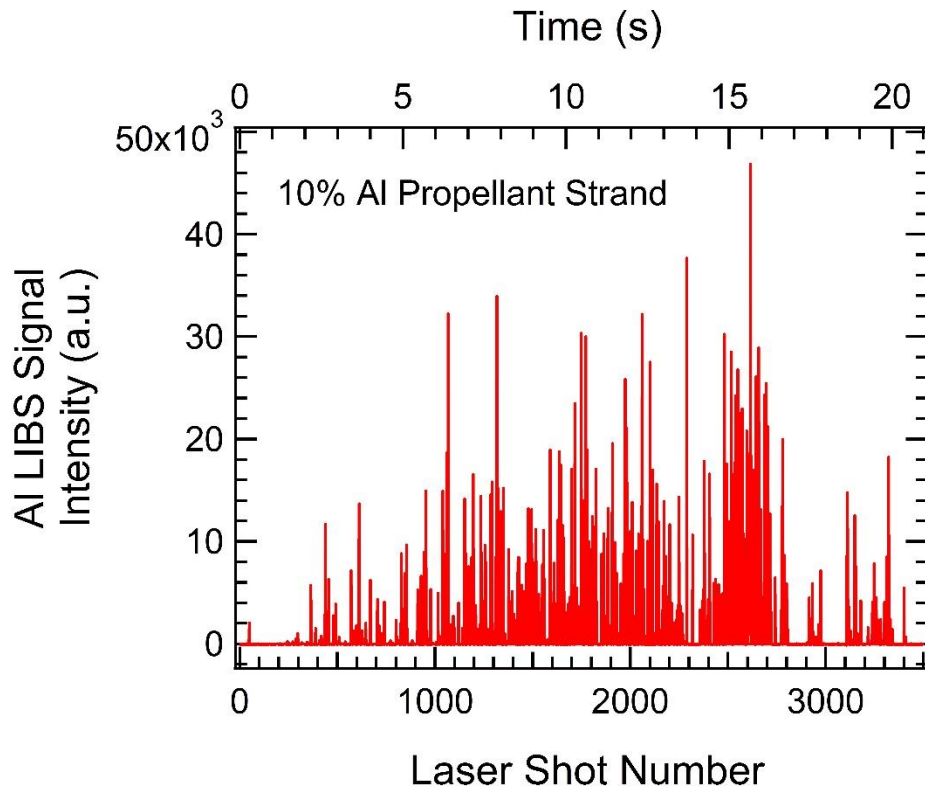
Figure 34. Single-laser-shot data of Al LIBS signal for the entire duration the burn, recorded in 10% Al propellant strand shown as a function of the laser shot number. The Al LIBS signal is extracted from the peak intensity of the 396-nm line.

72
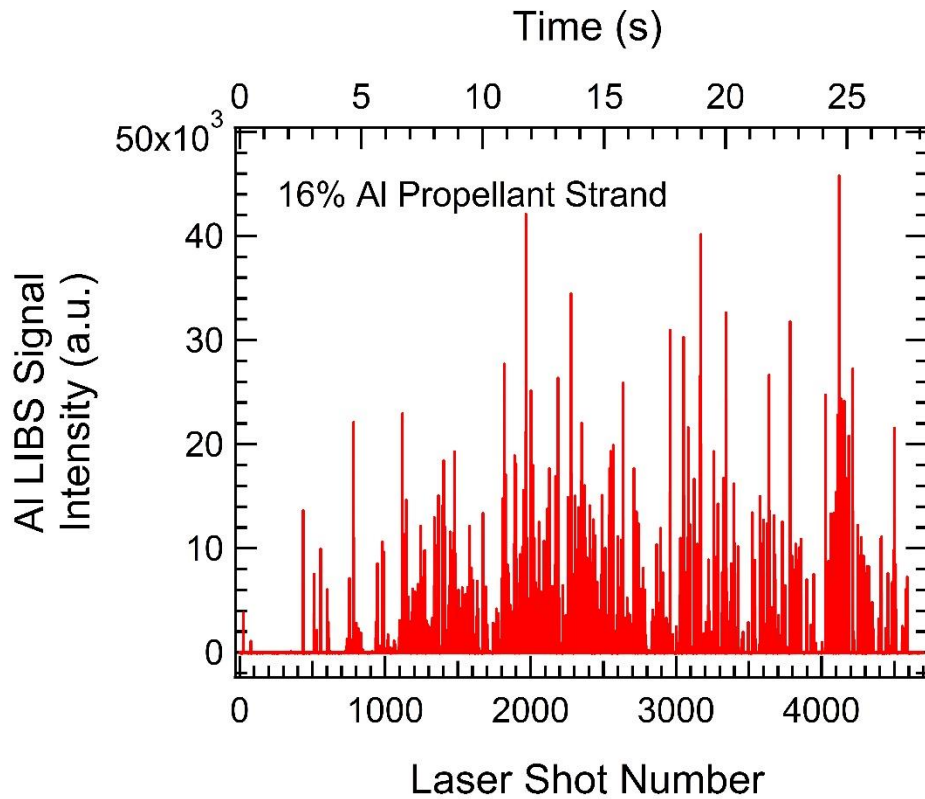
Figure 35. Single-laser-shot data of Al LIBS signal for the entire duration the burn, recorded in 10% Al propellant strand shown as a function of the laser shot number. The Al LIBS signal is extracted from the peak intensity of the 396-nm line.

If we take portions of these burns, specifically 500 laser shots, the trend becomes a little more apparent. These can be seen in Figure 36, Figure 37, and Figure 38, for 5%, 10%, and 16% respectively.
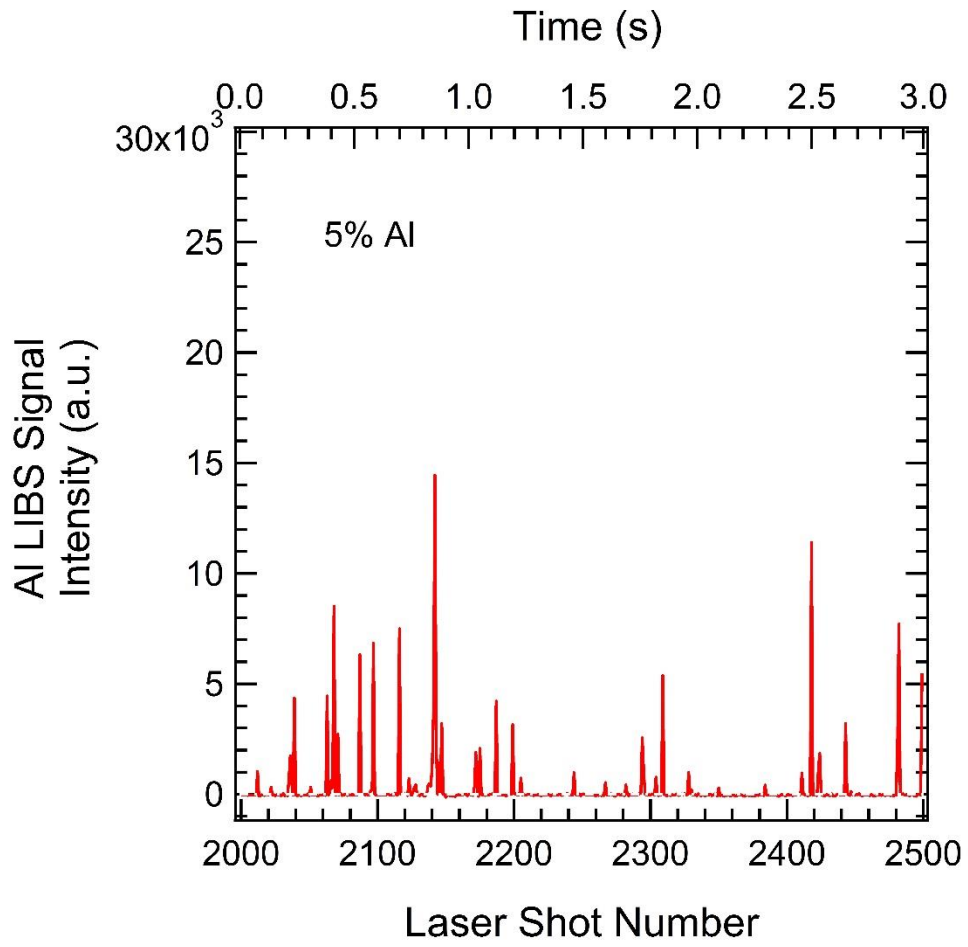
Figure 36. The data corresponding to 500 laser shots (shot range 2000 –2500) for the burn of 5% Al strand shown in Fig. 33.
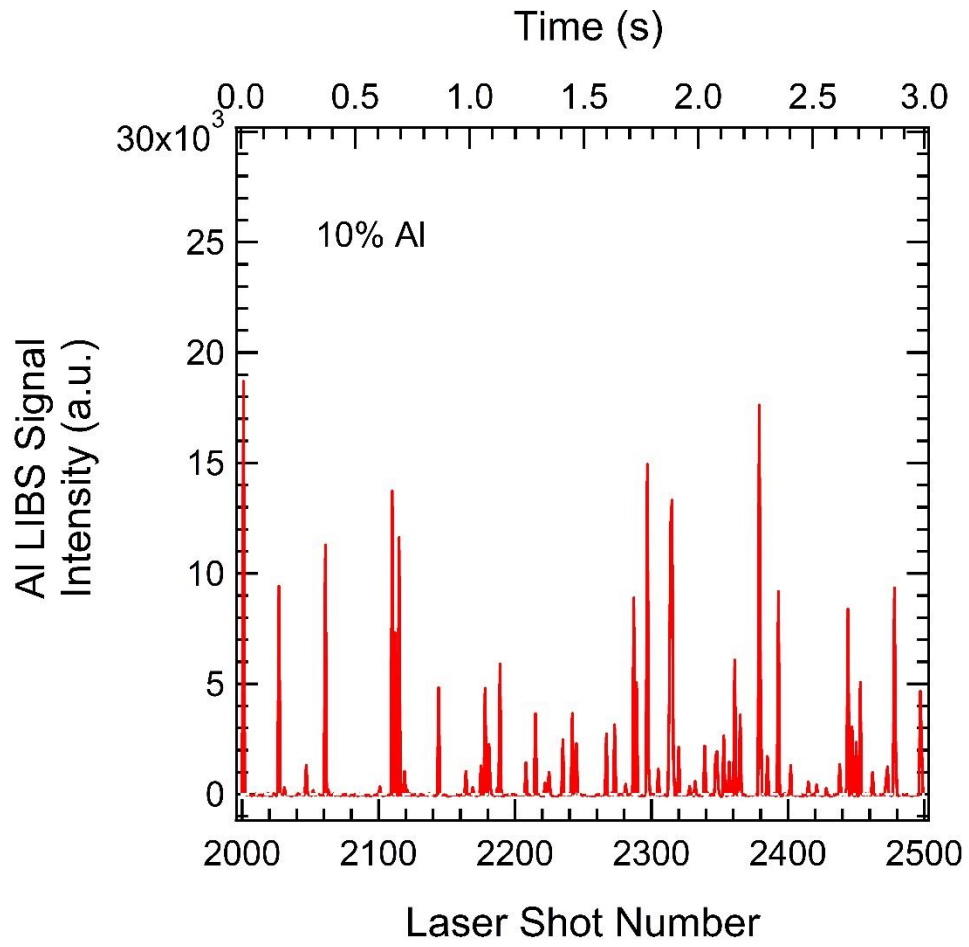
Figure 37. The data corresponding to 500 laser shots (shot range 2000 –2500) for the burn of 10% Al strand shown in Fig. 34.
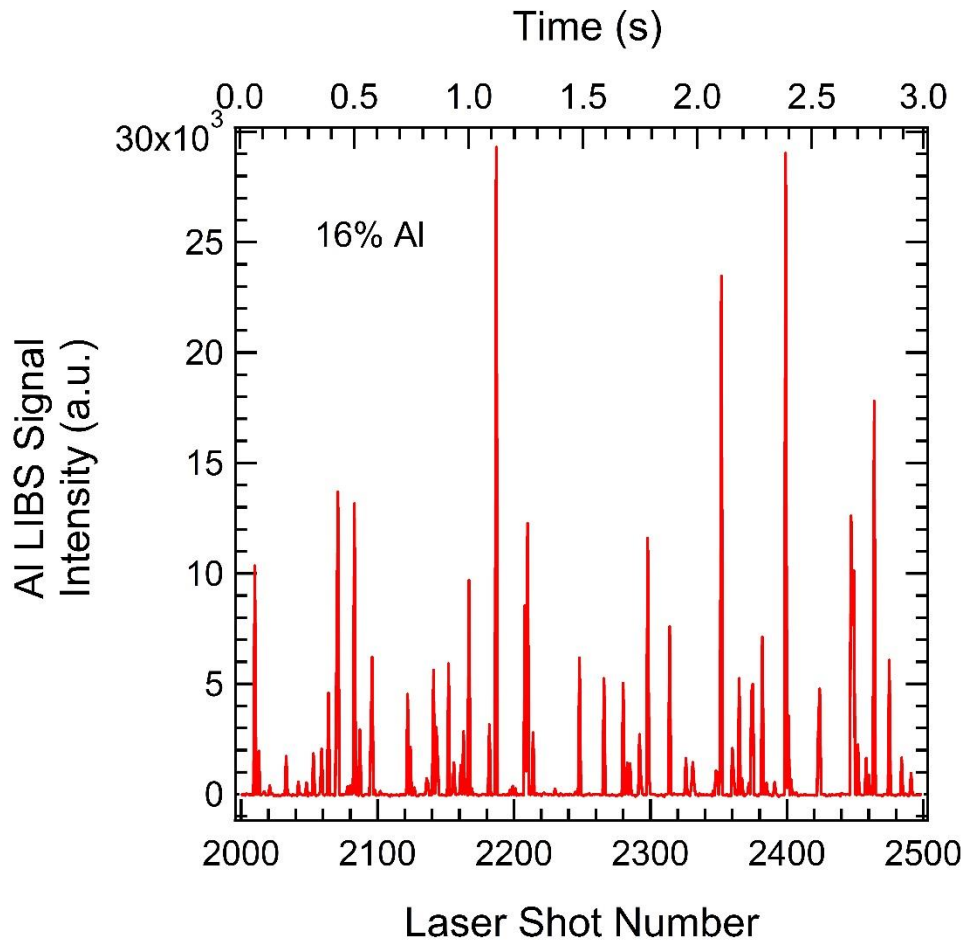
Figure 38. The data corresponding to 500 laser shots (shot range 2000 –2500) for the burn of 16% Al strand shown in Fig. 35.

If we generate histograms from these 500 shots, as was done in the nanosecond scheme, and then calculate the percentage of time seeing LIBS signal, the trend can be seen. With the histograms, though, in the femtosecond scheme, the trend can't be seen as readily in the figures as in the nanosecond due to a high counts of seeing no LIBS signal, so the graph vertical has been split so that the trend is easier to see. In other words, the blue column dominates the figure, which makes it hard to see the rest of the columns with

lower than 10 counts in them. These histograms for 5%, 10%, and 16% Al can be seen in

Figure 39, Figure 40, and Figure 41, respectively.
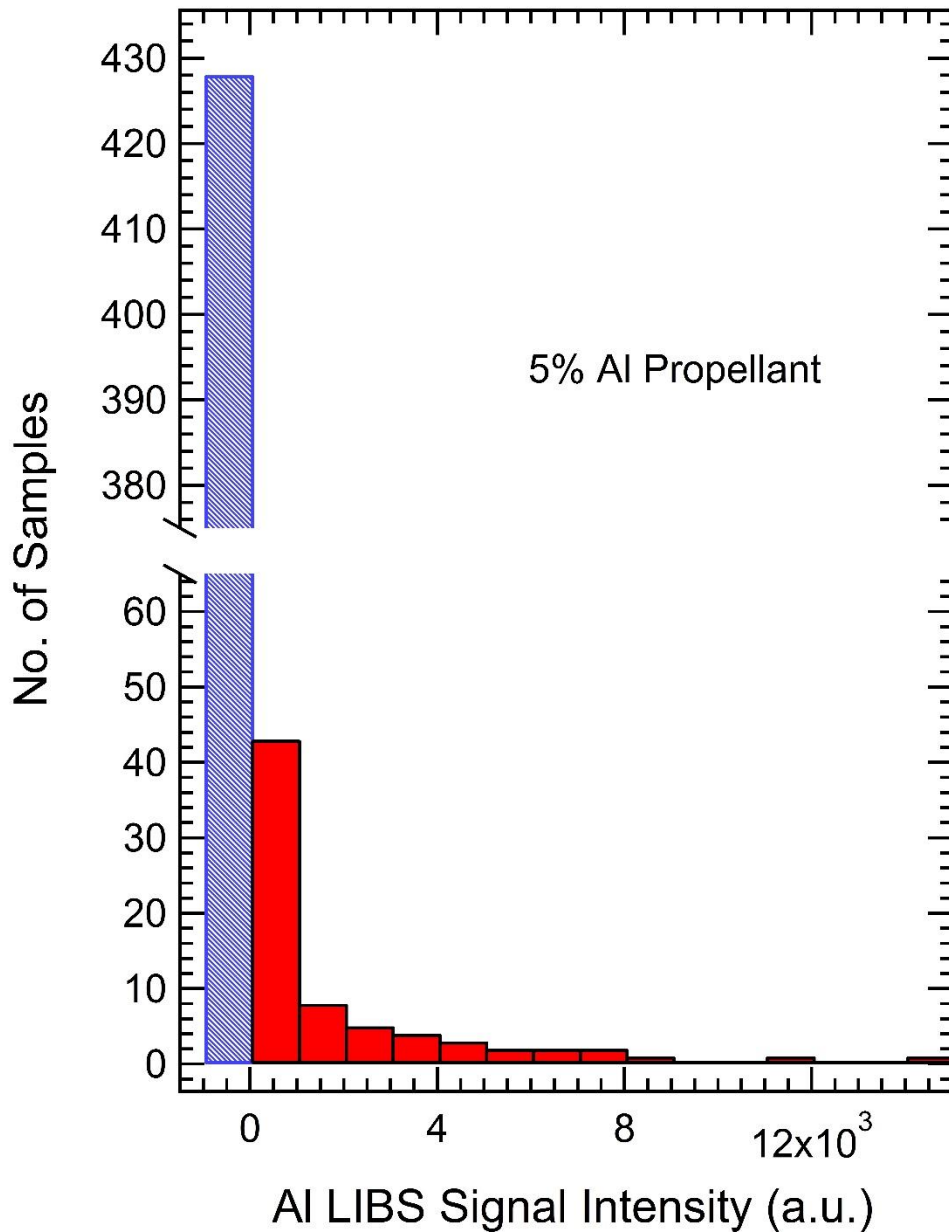
Figure 39. Histogram generated for 500 single shots with fs-LIBS of a 5% Al doped propellant burn. The Al LIBS signal is pulled from the peak intensity of the 396nm line.
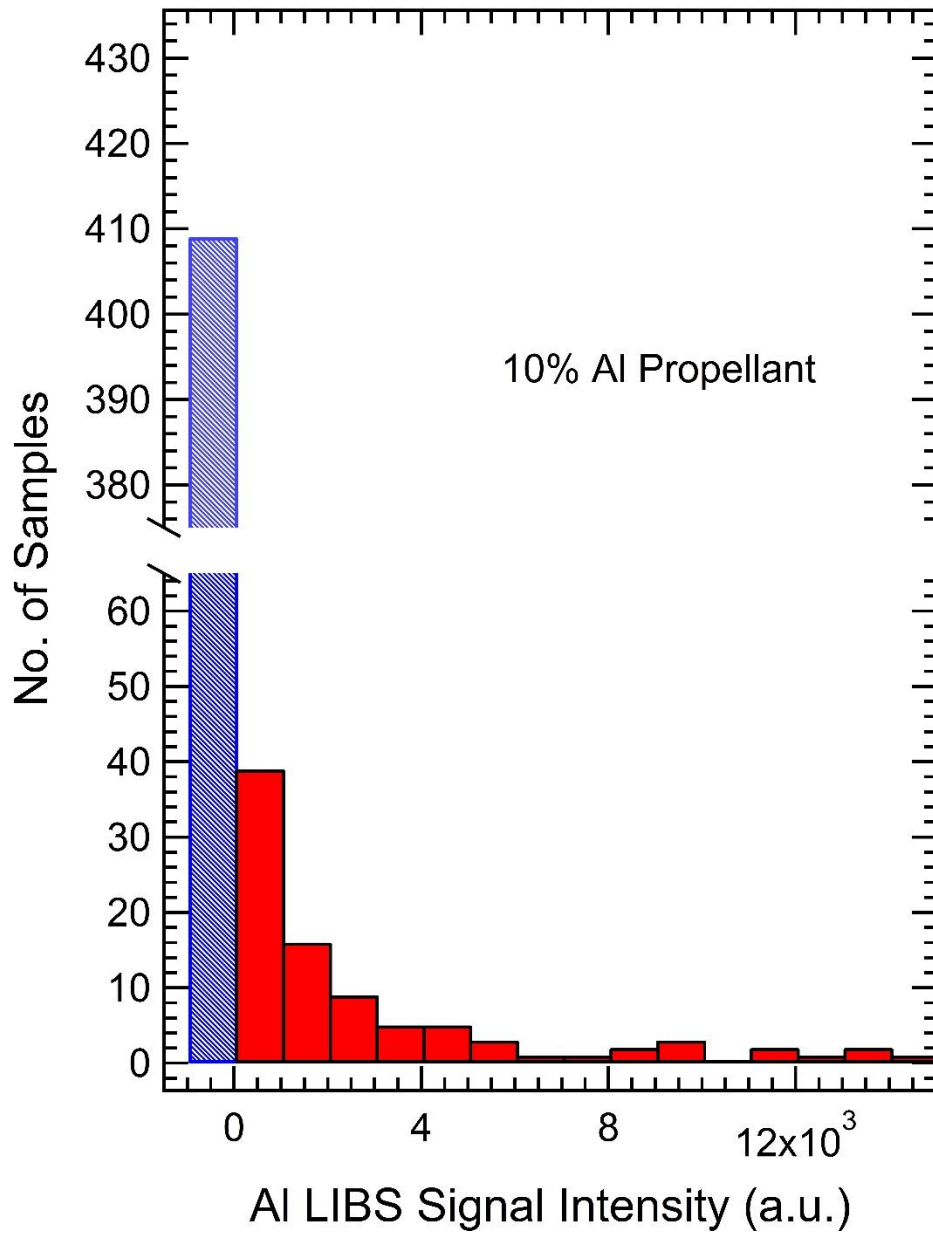
Figure 40. Histogram generated for 500 single shots with fs-LIBS of a 10% Al propellant burn. The Al LIBS signal is pulled from the peak intensity of the 396nm line.
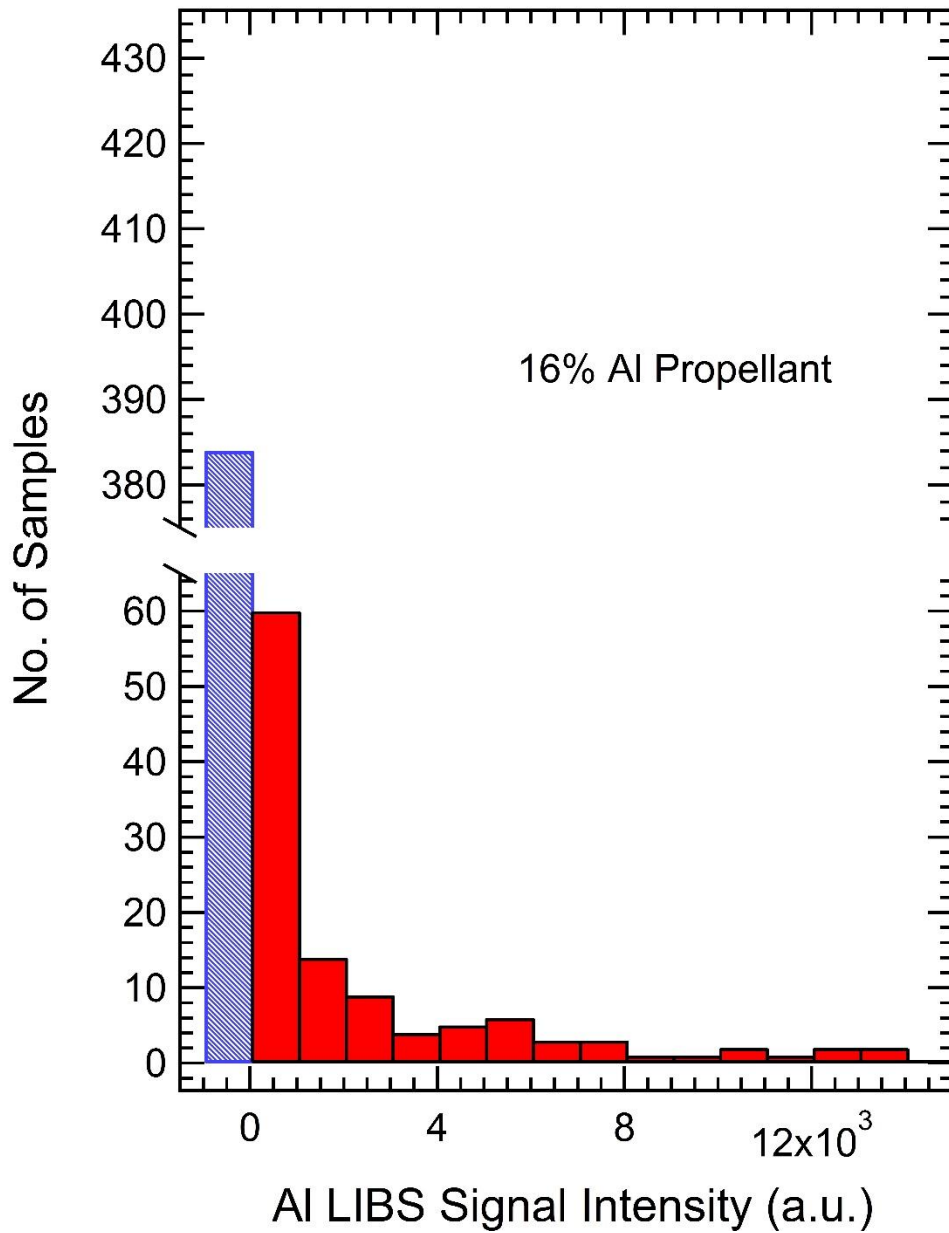
Figure 41. Histogram generated for 500 single shots with fs-LIBS of a 16% Al propellant burn. The Al LIBS signal is pulled from the peak intensity of the 396nm line.

The percentage of time seeing LIBS signal with the single shot data versus the mass percentage of aluminum present in the solid propellants can be seen in Figure 42.

Unlike the nanosecond scheme, the femtosecond scheme shows a linear trend all the way throughout between percent of time seeing signal and mass percent of Al.
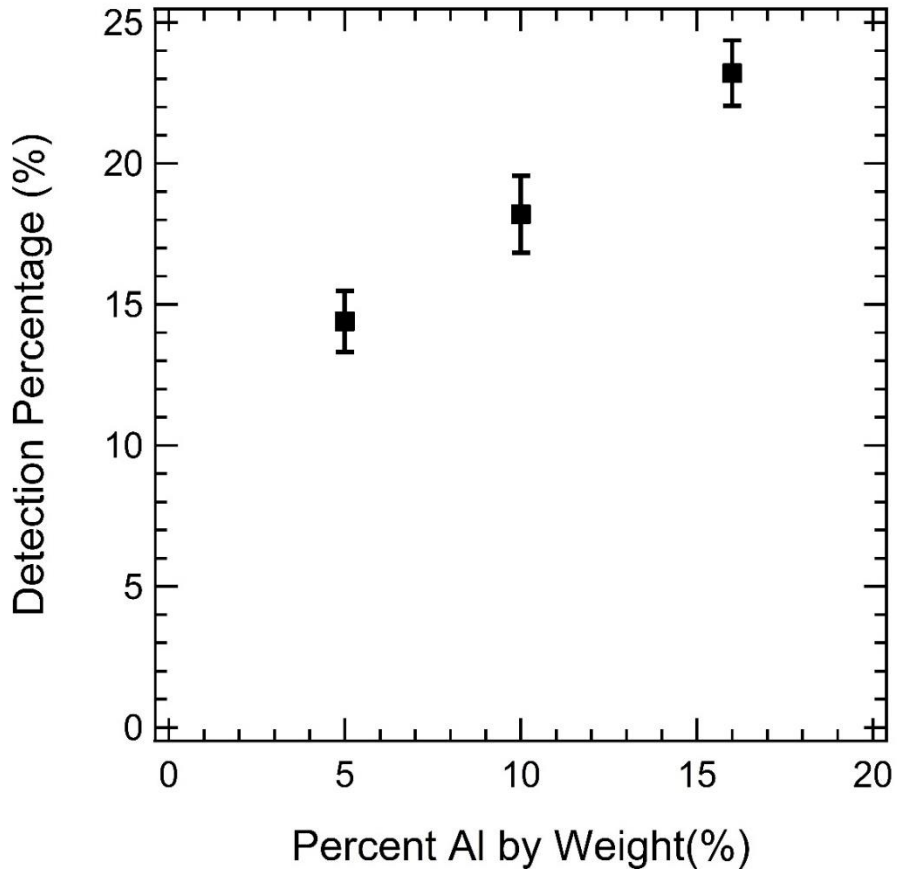
Figure 42. Percent of time observing LIBS signal in the femtosecond scheme plotted against the Al mass percentage present in the initial solid propellant strands.

To summarize all testing in the nanosecond and femtosecond schemes, Table 4 has been compiled to show the successful or unsuccessful detection of each propellant strand tested.

Table 4. Summary of all propellant strand types tested in both the nanosecond and femtosecond schemes indicating a detection capability of each scheme in the gas phase exhaust region of the HTPB/AP solid propellant strands.

Additive	% Additive (by mass)	Detected in ns-scheme (Y/N)	Detected in fs-scheme (Y/N)
Al	16	Y	Y
Al	10	Y	Y
Al	5	Y	Y
Pb	16	N	Y
$(C_{17}H_{35}COO)_2Pb$	16	N	Y
Cu	2	N	Y
Cu	5	N	Y
Cu	20	N	Y
Hg_2Cl_2	16	N	Y

5. CONCLUSION AND RECOMMENDATIONS FOR FUTURE WORK

5.1. Conclusions

The experimentally-recorded spectral lines from the solid metal plates compares well with the NIST database, so the present LIBS apparatus is considered to be calibrated and detecting individual metal species accurately. The laser energy dependence study in the nanosecond scheme suggests that a laser pulse energy of 100 mJ/pulse is an acceptable level, and in the femtosecond scheme, a 4 mJ/pulse energy level is acceptable. Plasma decay scans show that an optimal detection gate is one that is delayed approximately 300 ns with respect to the laser pulse for the nanosecond scheme and 100 ns for the femtosecond scheme, which, when using these gate delays, results in an emission signal without any continuum background noise. In the nanosecond scheme, the LIBS signal from aluminum in the gas phase exhaust region is detected at various concentrations down to 5% by mass in the AP/HTPB propellant strands, while the femtosecond scheme is able to detect all metallic additives in all concentrations investigated. A linear relationship is evident between the mass percentage of metal and LIBS signal in the femtosecond scheme, while there seems to be a point in the nanosecond scheme where the system begins to act homogeneous.

5.2. Recommendations for Future Work

Future studies can be focused on increasing the detection limit, finding the lowest mass percentage of each propellant where a signal can still be detected, i.e. lowest concentration in the gas phase, modeling the difference between nanosecond and

femtosecond work and why femtosecond is detecting while nanosecond is not, expanding to more compounds in the gas phase, and characterizing the particle flow field using a scheme such as digital in-line holography (DIH) so that experimental LIBS signals can be better interpreted statistically.

While all of this work is important for reaching the ultimate goal of getting this LIBS scheme into the field for detecting metallic particles in the air, the most exciting, promising, and something our group has already begun to investigate is the DIH experiment. Holography is a powerful tool that records a photographic rendering of a light field and can be used to display a fully 3-D image of the holographed subject. In traditional holography, two light sources are needed, which interfere with each other. These interference patterns are then collected on a special holographic film. When the original light source is reapplied, the hologram is produced. This traditional method has been transformed into a digital form, where a CCD or CMOS cameras can be used to record the interference patterns. The patterns can then be digitally reconstructed to produce the hologram. This digital holography is a powerful tool that has emerged in the area of holographic particle image velocimetry (HPIV), which allows obtaining a time and 3D-space-resolved flow field data, even for turbulent flow [71, 72]. DIH is an alternative technique to traditional digital holography that uses only one light source, which generates the interference pattern with the actual particles in the flow field, which are typically similar to microspheres. DIH resolution of particles is limited only by the wavelength of the light used [73]. Guildenbecher et al. have demonstrated using this technique of DIH for high speed (20 kHz) for transient tracking and sizing of particles in flow fields very

similar to those in our experiments [74]. Specifically, they used aluminized HTPB/AP solid propellant strands and studied the motion and size of particles flying off the surface of the propellant using a continuous 532 nm laser. They were able to produce high speed video of this particle field by stitching together multiple still images, an example of which is seen below in Figure 43.
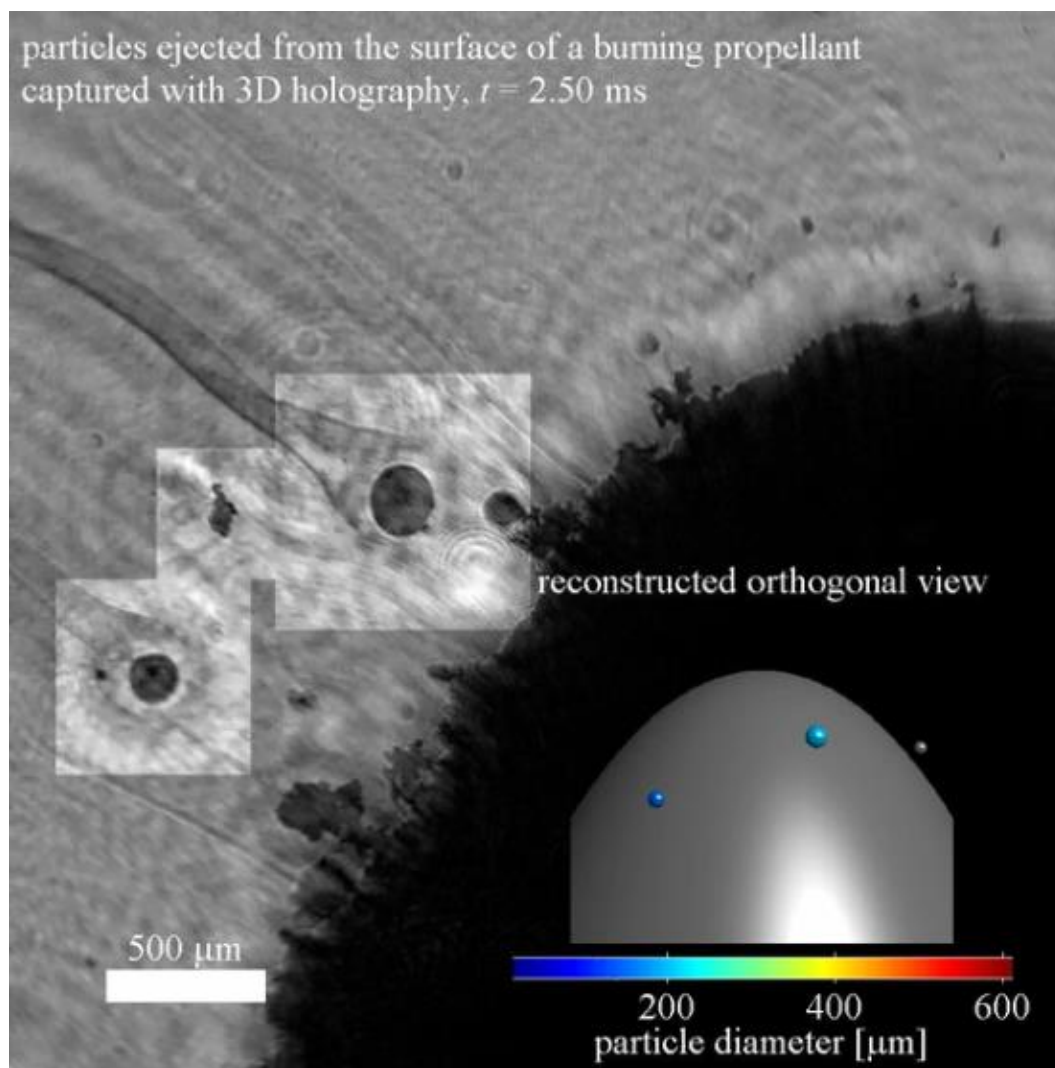
Figure 43. DIH image of burning aluminum particles from the combustion of a solid rocket propellant [74].

Guildenbecher et al. have shown that DIH can be a powerful tool, but they have not explored what the actual particles are made of, whether aluminum, binder material, or AP crystals. If we can run DIH experiments simultaneously to LIBS, we will be able to investigate in real time exactly what particles we are striking and what those particles consist of.

REFERENCES

1. C. Carmicino and A. R. Sorge, "Experimental Investigation into the Effect of Solid-Fuel Additives on Hybrid Rocket Performance," J. Propul. Power **31**, 699-713 (2015).

2. S. Chaturvedi and P. N. Dave, "Solid propellants: AP/HTPB composite propellants," Arabian Journal of Chemistry (2015).

3. L. Meda, G. Marra, L. Galfetti, F. Severini, and L. De Luca, "Nano-aluminum as energetic material for rocket propellants," Mater. Sci. Eng. C-Biomimetic Supramol. Syst. **27**, 1393-1396 (2007).

4. M. A. Stephens, Petersen, E. L., Carro, R., Reid, D. L., and Seal, S., "Multi-Parameter Study of Nanoscale TiO2 and CeO2 Additives in Composite AP/HTPB Solid Propellants," Propellants, Explosives, Pyrotechnics **Vol. 35**, pp. 143-152 (2010).

5. P. E. Schwarze, J. Ovrevik, M. Lag, M. Refsnes, P. Nafstad, R. B. Hetland, and E. Dybing, "Particulate matter properties and health effects: consistency of epidemiological and toxicological studies," Hum. Exp. Toxicol. **25**, 559-579 (2006).

6. C. Sioutas, R. J. Delfino, and M. Singh, "Exposure assessment for atmospheric ultrafine particles (UFPs) and implications in epidemiologic research," Environ. Health Perspect. **113**, 947-955 (2005).

7. S. Y. Chan and N. H. Cheung, "Analysis of solids by laser ablation and resonance-enhanced laser-induced plasma spectroscopy," Anal. Chem. **72**, 2087-2092 (2000).

8. R. Cremers D. A., L. J. , "Handbook of Laser-Induced Breakdown Spectroscopy," (2013).

9. D. W. Hahn, "Laser-induced breakdown spectroscopy for sizing and elemental analysis of discrete aerosol particles," Appl. Phys. Lett. **72**, 2960-2962 (1998).

10. G. A. Lithgow, A. L. Robinson, and S. G. Buckley, "Ambient measurements of metal-containing PM2.5 in an urban environment using laser-induced breakdown spectroscopy," Atmos. Environ. **38**, 3319-3328 (2004).

11.   W. D. Kulatilaka, Jiang, N., Roy, S., and Gord, J. R., "High-Repetition-Rate Imaging of Atomic Oxygen In Flames," 8th U. S. National Combustion Meeting, University of Utah (2013).

12.   W. D. Kulatilaka, J. R. Gord, V. R. Katta, and S. Roy, "Photolytic-interference-free, femtosecond two-photon fluorescence imaging of atomic hydrogen," Opt. Lett. **37**, 3051-3053 (2012).

13.   W. D. Kulatilaka, J. R. Gord, and S. Roy, "Femtosecond two-photon LIF imaging of atomic species using a frequency-quadrupled Ti:sapphire laser," Appl. Phys. B-Lasers Opt. **116**, 7-13 (2014).

14.   D. A. Rusak, B. C. Castle, B. W. Smith, and J. D. Winefordner, "Fundamentals and applications of laser-induced breakdown spectroscopy," Crit. Rev. Anal. Chem. **27**, 257-290 (1997).

15.   D. W. Hahn and M. M. Lunden, "Detection and analysis of aerosol particles by laser-induced breakdown spectroscopy," Aerosol Sci. Technol. **33**, 30-48 (2000).

16.   V. Hohreiter, J. E. Carranza, and D. W. Hahn, "Temporal analysis of laser-induced plasma properties as related to laser-induced breakdown spectroscopy," Spectroc. Acta Pt. B-Atom. Spectr. **59**, 327-333 (2004).

17.   V. Hohreiter and D. W. Hahn, "Calibration effects for laser-induced breakdown spectroscopy of gaseous sample streams: Analyte response of gas-phase species versus solid-phase species," Anal. Chem. **77**, 1118-1124 (2005).

18.   L. J. Radziemski, T. R. Loree, D. A. Cremers, and N. M. Hoffman, "Time-Resolved Laser-Induced Breakdown Spectrometry Of Aerosols," Anal. Chem. **55**, 1246-1252 (1983).

19.   Y. Y. Zhang, S. Q. Li, Y. H. Ren, Q. Yao, and S. D. Tse, "A new diagnostic for volume fraction measurement of metal-oxide nanoparticles in flames using phase-selective laser-induced breakdown spectroscopy," Proc. Combust. Inst. **35**, 3681-3688 (2015).

20.   J. E. Carranza and D. W. Hahn, "Assessment of the upper particle size limit for quantitative analysis of aerosols using laser-induced breakdown spectroscopy," Anal. Chem. **74**, 5450-5454 (2002).

21.   K. Iida, C. Y. Wu, and D. W. Hahn, "In situ analysis of the interaction of manganese vapor and silica microspheres in a laboratory-scale combustor," Combust. Sci. Technol. **176**, 453-480 (2004).

22.   A. Molina, P. M. Walsh, C. R. Shaddix, S. M. Sickafoose, and L. G. Blevins, "Laser-induced breakdown spectroscopy of alkali metals in high-temperature gas," Appl. Optics **45**, 4411-4423 (2006).

23.   D. K. Ottesen, J. C. F. Wang, and L. J. Radziemski, "Real-Time Laser Spark Spectroscopy Of Particulates In Combustion Environments," Appl. Spectrosc. **43**, 967-976 (1989).

24.   J. A. Stearns, S. E. McElman, and J. A. Dodd, "Identification of vapor-phase chemical warfare agent simulants and rocket fuels using laser-induced breakdown spectroscopy," Appl. Optics **49**, C8-C15 (2010).

25.   B. C. Windom, P. K. Diwakar, and D. W. Hahn, "Dual-pulse laser induced breakdown spectroscopy for analysis of gaseous and aerosol systems: Plasma-analyte interactions," Spectroc. Acta Pt. B-Atom. Spectr. **61**, 788-796 (2006).

26.   F. Matroodi and S. H. Tavassoli, "Experimental investigation on concurrent laser-induced breakdown spectroscopy Raman spectroscopy," Appl. Optics **54**, 400-407 (2015).

27.   A. W. Miziolek, Palleschi, V., "Laser Induced Breakdown Spectroscopy," (2006).

28.   J. A. Aguilera, C. Aragon, and J. Campos, "Determination Of Carbon Content In Steel Using Laser-Induced Breakdown Spectroscopy," Appl. Spectrosc. **46**, 1382-1387 (1992).

29.   F. Colao, V. Lazic, R. Fantoni, and S. Pershin, "A comparison of single and double pulse laser-induced breakdown spectroscopy of aluminum samples," Spectroc. Acta Pt. B-Atom. Spectr. **57**, 1167-1179 (2002).

30.   C. Colon, G. Hatem, E. Verdugo, P. Ruiz, and J. Campos, "Measurement Of The Stark-Broadening And Shift Parameters For Several Ultraviolet Lines Of Singly Ionized Aluminum," J. Appl. Phys. **73**, 4752-4758 (1993).

31.   D. A. Cremers, L. J. Radziemski, and T. R. Loree, "Spectrochemical Analysis Of Liquids Using The Laser Spark," Appl. Spectrosc. **38**, 721-729 (1984).

32.   P. Fichet, P. Mauchien, J. F. Wagner, and C. Moulin, "Quantitative elemental determination in water and oil by laser induced breakdown spectroscopy," Anal. Chim. Acta **429**, 269-278 (2001).

33.   A. M. Gonzalez, M. Ortiz, and J. Campos, "Transition-Probabilities For Lines Arising From The 3d4 4p Configuration Of Cr(Ii)," Can. J. Phys. **72**, 57-60 (1994).

34. K. J. Grant, G. L. Paul, and J. A. Oneill, "Time-Resolved Laser-Induced Breakdown Spectroscopy Of Iron-Ore," Appl. Spectrosc. **44**, 1711-1714 (1990).

35. W. Q. Lei, V. Motto-Ros, M. Boueri, Q. L. Ma, D. C. Zhang, L. J. Zheng, H. P. Zeng, and J. Yu, "Time-resolved characterization of laser-induced plasma from fresh potatoes," Spectroc. Acta Pt. B-Atom. Spectr. **64**, 891-898 (2009).

36. I. Monch, R. Sattmamn, and R. Noll, *High speed identification of polymers by laser-induced breakdown spectroscopy*, Sensors, Sensor Systems, and Sensor Data Processing (Spie - Int Soc Optical Engineering, Bellingham, 1997), Vol. 3100, pp. 64-74.

37. G. W. Rieger, A. Taschuk, Y. Y. Tsui, and R. Fedosejevs, "Comparative study of laser-induced plasma emission from microjoule picosecond and nanosecond KrF-laser pulses," Spectroc. Acta Pt. B-Atom. Spectr. **58**, 497-510 (2003).

38. P. Stavropoulos, C. Palagas, G. N. Angelopoulos, D. N. Papamantellos, and S. Couris, "Calibration measurements in laser-induced breakdown spectroscopy using nanosecond and picosecond lasers," Spectroc. Acta Pt. B-Atom. Spectr. **59**, 1885-1892 (2004).

39. R. L. Vander Wal, T. M. Ticich, J. R. West, and P. A. Householder, "Trace metal detection by laser-induced breakdown spectroscopy," Appl. Spectrosc. **53**, 1226-1236 (1999).

40. Y. Yuan, S. Q. Li, and Q. Yao, "Dynamic behavior of sodium release from pulverized coal combustion by phase-selective laser-induced breakdown spectroscopy," Proc. Combust. Inst. **35**, 2339-2346 (2015).

41. J. E. Carranza, B. T. Fisher, G. D. Yoder, and D. W. Hahn, "On-line analysis of ambient air aerosols using laser-induced breakdown spectroscopy," Spectroc. Acta Pt. B-Atom. Spectr. **56**, 851-864 (2001).

42. M. D. Cheng, "Real-time measurement of trace metals on fine particles by laser-induced plasma techniques," Fuel Process. Technol. **65**, 219-229 (2000).

43. M. Essien, L. J. Radziemski, and J. Sneddon, "Detection Of Cadmium, Lead And Zinc In Aerosols By Laser-Induced Breakdown Spectrometry," J. Anal. At. Spectrom. **3**, 985-988 (1988).

44. D. Mukherjee, A. Rai, and M. R. Zachariah, "Quantitative laser-induced breakdown spectroscopy for aerosols via internal calibration: Application to the oxidative coating of aluminum nanoparticles," J. Aerosol. Sci. **37**, 677-695 (2006).

45.   R. E. Neuhauser, U. Panne, and R. Niessner, "Laser-induced plasma spectroscopy (LIPS): a versatile tool for monitoring heavy metal aerosols," Anal. Chim. Acta **392**, 47-54 (1999).

46.   H. S. Zhang, F. Y. Yueh, and J. P. Singh, "Laser-induced breakdown spectrometry as a multimetal continuous-emission monitor," Appl. Optics **38**, 1459-1466 (1999).

47.   B. Nemet and L. Kozma, "Time-resolved optical emission spectrometry of Q-switched Nd:YAG laser-induced plasmas from copper targets in air at atmospheric pressure," Spectroc. Acta Pt. B-Atom. Spectr. **50**, 1869-1888 (1995).

48.   M. Autin, A. Briand, P. Mauchien, and J. M. Mermet, "Characterization By Emission-Spectrometry Of A Laser-Produced Plasma From A Copper Target In Air At Atmospheric-Pressure," Spectroc. Acta Pt. B-Atom. Spectr. **48**, 851-862 (1993).

49.   O. Barthelemy, J. Margot, M. Chaker, M. Sabsabi, F. Vidal, T. W. Johnston, S. Laville, and B. Le Drogoff, "Influence of the laser parameters on the space and time characteristics of an aluminum laser-induced plasma," Spectroc. Acta Pt. B-Atom. Spectr. **60**, 905-914 (2005).

50.   M. Sabsabi and P. Cielo, "Quantitative-Analysis Of Aluminum-Alloys By Laser-Induced Breakdown Spectroscopy And Plasma Characterization," Appl. Spectrosc. **49**, 499-507 (1995).

51.   J. M. Vadillo, M. Milan, and J. J. Laserna, "Space and time-resolved laser-induced breakdown spectroscopy using charge-coupled device detection," Fresenius J. Anal. Chem. **355**, 10-15 (1996).

52.   S. M. Angel, D. N. Stratis, K. L. Eland, T. S. Lai, M. A. Berg, and D. M. Gold, "LIBS using dual- and ultra-short laser pulses," Fresenius J. Anal. Chem. **369**, 320-327 (2001).

53.   B. Le Drogoff, M. Chaker, J. Margot, M. Sabsabi, P. Barthelemy, T. W. Johnston, S. Laville, and F. Vidal, "Influence of the laser pulse duration on spectrochemical analysis of solids by laser-induced plasma spectroscopy," Appl. Spectrosc. **58**, 122-129 (2004).

54.   B. Le Drogoff, J. Margot, M. Chaker, M. Sabsabi, O. Barthelemy, T. W. Johnston, S. Laville, F. Vidal, and Y. von Kaenel, "Temporal characterization of femtosecond laser pulses induced plasma for spectrochemical analysis of aluminum alloys," Spectroc. Acta Pt. B-Atom. Spectr. **56**, 987-1002 (2001).

55.   J. P. Singh, Thakur, S. N., "Laser Induced Breakdown Spectroscopy," (2007).

56. G. S. Senes, "Laser-Induced Breakdown Spectroscopy (LIBS) applied to terrestrial andextraterrestrial analogue geomaterials with emphasis to minerals and rocks," Earth-Science Reviews, 231-267 (2014).

57. J. L. Gottfried, F. C. De Lucia, C. A. Munson, and A. W. Miziolek, "Laser-induced breakdown spectroscopy for detection of explosives residues: a review of recent advances, challenges, and future prospects," Anal. Bioanal. Chem. **395**, 283-300 (2009).

58. A. W. Miziolek, F. DeLucia, C. Munson, and J. Gottfried, "A New Standoff Cb Detection Technology Based On The Fusion Of Libs And Raman," (2008).

59. J. Moros, J. A. Lorenzo, P. Lucena, L. M. Tobaria, and J. J. Laserna, "Simultaneous Raman Spectroscopy-Laser-induced Breakdown Spectroscopy for Instant Standoff Analysis of Explosives Using a Mobile Integrated Sensor Platform," Anal. Chem. **82**, 1389-1400 (2010).

60. F. Matroodi and S. H. Tavassoli, "Simultaneous Raman and laser-induced breakdown spectroscopy by a single setup," Appl. Phys. B-Lasers Opt. **117**, 1081-1089 (2014).

61. K. L. Eland, D. N. Stratis, T. S. Lai, M. A. Berg, S. R. Goode, and S. M. Angel, "Some comparisons of LIBS measurements using nanosecond and picosecond laser pulses," Appl. Spectrosc. **55**, 279-285 (2001).

62. P. Fichet, D. Menut, R. Brennetot, E. Vors, and A. Rivoallan, "Analysis by laser-induced breakdown spectroscopy of complex solids, liquids, and powders with an echelle spectrometer," Appl. Optics **42**, 6029-6035 (2003).

63. G. A. Theriault and S. H. Lieberman, *Field deployment of a LIBS probe for rapid delineation of metals in soils*, Advanced Technologies for Environmental Monitoring and Remediation (Spie - Int Soc Optical Engineering, Bellingham, 1996), Vol. 2835, pp. 83-88.

64. M. Stepputat and R. Noll, "On-line detection of heavy metals and brominated flame retardants in technical polymers with laser-induced breakdown spectrometry," Appl. Optics **42**, 6210-6220 (2003).

65. R. L. Gleason and D. W. Hahn, "The effects of oxygen on the detection of mercury using laser-induced breakdown spectroscopy," Spectroc. Acta Pt. B-Atom. Spectr. **56**, 419-430 (2001).

66. M. Stephens, Sammet, T., Carro, R., LePage, A., and Petersen, E., "Comparison of Hand and Mechanically Mixed AP/HTPB Solid Composite Propellants," AIAA Paper 2007-5765 (2007).

67. D. L. Reid, R. Draper, D. Richardson, A. Demko, T. Allen, E. L. Petersen, and S. Seal, "In situ synthesis of polyurethane-TiO2 nanocomposite and performance in solid propellants," J. Mater. Chem. A **2**, 2313-2322 (2014).

68. "NIST Atomic Energy Levels Data Center.," NIST Atomic Spectra Database, Physics Laboratory: National Institute of Standards and Technology. (1999).

69. S. Roy, N. Jiang, H. U. Stauffer, J. B. Schmidt, W. D. Kulatilaka, T. R. Meyer, C. E. Bunker, and J. R. Gord, "Spatially and temporally resolved temperature and shock-speed measurements behind a laser-induced blast wave of energetic nanoparticles," J. Appl. Phys. **113**, 7 (2013).

70. L. A. Alvarez-Trujillo, A. Ferrero, J. J. Laserna, and D. W. Hahn, "Alternative Statistical Methods for Spectral Data Processing: Applications to Laser-Induced Breakdown Spectroscopy of Gaseous and Aerosol Systems," Appl. Spectrosc. **62**, 1144-1152 (2008).

71. J. Katz and J. Sheng, "Applications of Holography in Fluid Mechanics and Particle Dynamics," in *Annual Review of Fluid Mechanics* (Annual Reviews, Palo Alto, 2010), pp. 531-555.

72. H. Meng, G. Pan, Y. Pu, and S. H. Woodward, "Holographic particle image velocimetry: from film to digital recording," Meas. Sci. Technol. **15**, 673-685 (2004).

73. W. Xu, M. H. Jericho, I. A. Meinertzhagen, and H. J. Kreuzer, "Digital in-line holography of microspheres," Appl. Optics **41**, 5367-5375 (2002).

74. D. R. Guildenbecher, M. A. Cooper, and P. E. Sojka, "High-speed (20 kHz) digital in-line holography for transient particle tracking and sizing in multiphase flows," Appl. Optics **55**, 2892-2903 (2016).

APPENDIX A

A. Data Analysis Code

Data of spectra was either taken in OceanView, Ocean Optics proprietary software, or in Lightfield, Princeton Instruments software. From OceanView, spectra can be saved into .TXT files. Matlab then transforms these .TXT files into .MAT files. Lightfield saves data in .SPE files. Using Lightfield, these .SPE files can be converted to .CSV files. Each frame, or spectra, in the .SPE file was made to put out one .CSV file. Matlab was used to pull information from each of these .CSV files and put it into a single Matlab .MAT file. Matlab was then used to manipulate this .MAT file to do whatever data analysis was needed. There were multiple versions of these two codes made, but the two most recent, which were used for the propellant sticks, have been pasted below for the convenience of the reader.

A.1: Lightfield CSV to Matlab file

```matlab
close all; clear all; clc;

%% User inputs
foldername=('Data/Lightfield/2016_12_14/Al_5%_3_CSV'); %input
the name of the folder containing .txt files from oceanview
save_as=('al_5%_3_r'); %input the file name you would like for
the output file
% the file will be saved in the same folder as the one you
called the files
% from

%%folder stuff
p=fileparts(pwd);
myfolder=fullfile([p '/' foldername]);
MyFiles = dir([myfolder '/*.csv']);
Size_MyFiles = size(MyFiles);

%extracting the data
```

```matlab
s=struct;
for k=1:Size_MyFiles
    file_to_open=[myfolder '/' char(MyFiles(k).name)];
    fid=fopen(file_to_open);
    filechar=char(file_to_open);
    disp(['Processing file',filechar,'\n']);
    data=csvread(char(file_to_open));
    wl=data(:,1);
    i=data(:,2);

    s(k).name=file_to_open;
    s(k).wavelength=wl(1:1024);
    s(k).intensity=i(1:1024);
end

%% file save info
file_to_save=save_as;
save([myfolder '/' file_to_save '.mat'],'s')


% to call data again later use (some
variable)=importdata(whatever file
% name you chose) and you will get a structure that has all of
the
% filenames with their corresponding wavelength and intensity
values
```

```matlab
%Kevin Campbell, Nicholas Niemiec, Morgan O'Neil Originally
created:
%08-02-2016 Edited: 01-30-2017
%plots spectrum data and finds peaks
%it is also set up for simple filtering
clear all; clc; close all

%% user inputs

%file name
filename=('al_5%_2_r.mat');%input the file path the desired file
foldername=('Data/Lightfield/2016_12_14/Al_5%_2_CSV'); %input
all folders seperated by /

%Input desired peaks
wl_peakdesired = 395.35; %nm electron emission peak

%Amount of laser shots averaged
% averaging_amount=1;

%plotting instructions
name=('Al Propellant Stick'); % input what you want the title of
the plot to be
files_skip=(1000); %this tells the script to plot every nth
file. e.g. if you input 4 files 1,5,9,13.... will be plotted
start_from=(52); %input the file you like to start plotting from
last_plot=(0); %insert the last file you would like plotted, if
you input zero it will go to the end of the folder
save_plots=(0); %set wheter or not you want the plots to be
saved input 1 to save 0 to discard

%steps input
Step_1 = [1:1:500];  % input the steps that were used for the
laser shots
units=('Laser Shot'); %insert units that the  steps are in

%peak finding parameters
find_peaks=(0); %input 1 if you want the script to find and plot
peaks, input 0 otherwise
prominence=(2000); %specify the prominence required for a peak
to be counted. higher number is stricter

%filtering parameters
filter=(1); %tells the script whether or not you want the output
plots to be filtered
order=(3); %input the order of filter you would like to use
```

95

```matlab
%% end user inputs

%%file stuff
p=fileparts(pwd);
myfile=fullfile([p '/' foldername '/' filename]);
data=importdata(myfile);

%selecting plot range stuff
[~,number_of_files]=size(data);
if last_plot==0
    last_plot=number_of_files;
end


%setting up steps
Step_matrix = [Step_1];
Size_Step_matrix = size(Step_matrix);

sizedata = size(data);
n=sizedata(2);

Final_matrix = zeros(n,2);
Peak = zeros(n,1);

if save_plots==1
p=fileparts(pwd);
mkdir([p '/' foldername],[name ' figures'])
end
 for k=start_from:files_skip:last_plot

%      % peak finder
%
[pks,locs]=findpeaks(data(k).intensity,data(k).wavelength,'MinPe
akProminence',prominence);
%      %filtering

    if filter==true
    data(k).intensity=medfilt1(data(k).intensity,order);
    end

    %plotting
    figure(k);
    hold on
    plot(data(k).wavelength,data(k).intensity);
%      axis([200 500 0 1*10^4])
    xlabel('Wavelength nm','fontSize',15)
    ylabel('Intensity Counts','fontSize',15)
    title([name ' '  units ' ' num2str(Step_matrix(k))])
```

```matlab
    if find_peaks==true
        for n=1:length(pks)
            txt=num2str(locs(n));
            text(locs(n),pks(n),txt)
        end
     end
    hold off
%      %saving code
%      if save_plots==1
%          myfolder=fullfile([p '/' foldername '/' name '
figures']);
%          savefig([myfolder '/' name ' ' num2str(Step_matrix(k))
])
%      end

 end

%type in locs to see the location of different peaks
figure(k+1)
hold on
for k=1:1:number_of_files
    plot(data(k).wavelength,data(k).intensity);
%     axis([200 500 0 6*10^4])
    xlabel('Wavelength nm','fontSize',15)
    ylabel('Intensity Counts','fontSize',15)
    title(name)
end
hold off

%Doing running average
for k = 1:n

Size_matrix = size(data(k).wavelength);


for kk = 1:1:Size_matrix(1)
   [~, index1] = min(abs(data(k).wavelength(:)-wl_peakdesired));
   Peak(k) = data(k).intensity(index1);
end

Final_matrix(k,:) = [Step_matrix(k) Peak(k)];
end
%
% Average_Final_Matrix=zeros(n-averaging_amount,2);
% Average_Intensity = zeros(n-averaging_amount,1);
%
% k=1;
%
% for k=1:n
```

```matlab
%
% Pulled_Intensity = Final_matrix(k:k+1,2);
% Average_Intensity(k) =
1/(averaging_amount+1)*sum(Pulled_Intensity);
%
% Average_Final_Matrix(k,:) = [Step_matrix(k)
Average_Intensity(k)];
% end


% f = fit(Final_matrix(:,1), Final_matrix(:,2), 'pchip');
hl1=plot(Final_matrix(:,1), Final_matrix(:,2));
xlabel('Laser Shot','fontSize',15)
ylabel('Intensity Counts','fontSize',15)

edges= [-1000 0:1200:40000 40000];
histogram(Final_matrix(:,2),edges)
xlabel('Intensity','fontSize',15)
ylabel('Counts','fontSize',15)
```

B. Specifications of Experimental Components

B.1: Spectra Physics Quanta Ray Lab 130, Nd:YAG Laser

Quanta-Ray® Lab Series

The Quanta-Ray® Lab series represent the intermediate range of oscillator-only lasers with output energies up to 1 J at 1064 nm. The Lab laser stands above its competitors because of its dual Nd:YAG rod and dual pump chamber oscillator configuration. This proprietary design provides intra-oscillator compensation for thermally-induced birefringence in the Nd:YAG rod, greatly reducing beam depolarization. This results in higher repetition rates, higher average powers and superior output beam quality than any other oscillator-only Nd:YAG laser on the market.

Quanta-Ray Lab Series Specifications

Product[1]	Lab-130-			Lab-150-			Lab-170-			Lab-190-			
Repetition Rate	10 Hz	30 Hz	50 Hz	10 Hz	30 Hz	50 Hz	10 Hz	30 Hz	50 Hz	10 Hz[4]	30 Hz	50 Hz	100 Hz
Energy (mJ/p)[2]													
1064 nm	450 mJ	275 mJ	200 mJ	650 mJ	500 mJ	300 mJ	850 mJ	700 mJ	550 mJ	1000 mJ	800 mJ	600 mJ	325 mJ
532 nm	200 mJ	100 mJ	70 mJ	300 mJ	200 mJ	100 mJ	450 mJ	325 mJ	210 mJ	500 mJ	400 mJ	250 mJ	120 mJ
355 nm[23]	90 mJ	40 mJ	30 mJ	150 mJ	100 mJ	40 mJ	220 mJ	175 mJ	100 mJ	250 mJ	200 mJ	100 mJ	50 mJ
EEO-355 nm[5, 23]	--	--	--	--	--	--	240 mJ	--	--	300 mJ	--	--	--
266 nm	55 mJ	25 mJ	15 mJ	75 mJ	35 mJ	25 mJ	100 mJ	65 mJ	30 mJ	120 mJ	65 mJ	25 mJ	20 mJ

Performance Specifications

Wavelength	Pulse Width[5]	Short Term Energy Stability[6]	Long Term Power Drift[7]
1064 nm	8–12 ns	±2%	<3%
532 nm	1–2 ns <1064 nm	±3%	<5%
355 nm	2–3 ns <1064 nm	±4%	<6%
266 nm	3–4 ns <1064 nm	±8%	<10%

Beam Specifications

Spatial Mode Profile[8]	Standard Fit	ESM Fit[9]
Near Field (1 m)	>70%	Contact Spectra-Physics
Far Field (∞)	>95%	Contact Spectra-Physics
Modulation[10]	<40%	Contact Spectra-Physics
Beam Diameter[11]	<10 mm	
Beam Pointing Stability[12]	<±50 µrad	
Beam Divergence[13]	<0.5 mrad	
Lamp Lifetimes[14]	30 million pulses	
Linewidth		
Standard	<1.0 cm⁻¹	
Injection Seeded[15]	<0.003 cm⁻¹	
Timing Jitter[16]	<0.5 ns	

Notes for specifications are on page 5.

Quanta-Ray Lab Laser Dimensions

Side View

Front View

Dimensions are in inches (cm)
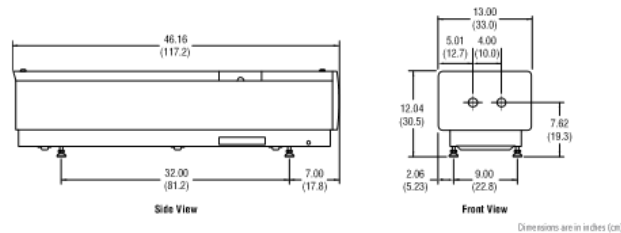
Solstice® Ace™

Specifications[1, 10]

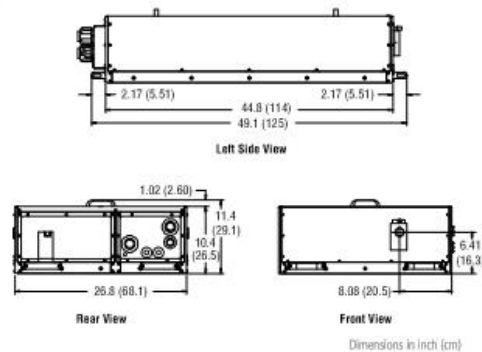| Output Characteristics		Solstice Ace		
Pulse Width[2, 3]		<35 fs – <120 fs		
Repetition Rate[4]		1 kHz	5 kHz	10 kHz
Average Power	Ascend 60:	>7.0 W	>8.0 W	>7.0 W
	Ascend 40:	>5.0 W	>6.0 W	>5.0 W
Pulse Energy	Ascend 60:	>7.0 mJ	>1.6 mJ	>0.7 mJ
	Ascend 40:	>5.0 mJ	>1.2 mJ	>0.5 mJ
Pre-Pulse Contrast Ratio[5]		1000:1		
Post-Pulse Contrast Ratio[6]		100:1		
Operating Temperature Range		±5°C		
Energy Stability		<0.5% rms over 24 hours		
Beam Pointing Stability		<5 µrad (rms)[7]		
Wavelength[8, 9]		780–820 nm[9]		
Spatial Mode		TEM$_{00}$ (M^2 <1.25, both axes)		
Beam Diameter (1/e^2)		10–11 mm (nominal)		
Polarization		Linear, Horizontal		

1. Due to our continuous product improvements, specifications are subject to change without notice.
2. A Gaussian pulse shape (0.7 deconvolution factor) is used to determine pulse width (FWHM) from autocorrelation signal as measured with a Newport PulseScout® autocorrelator.
3. Pulse width must be specified at time of purchase.
4. The desired optimum repetition rate can be specified at the time of purchase or additional optics sets can be used to reconfigure the amplifier. Any system can be operated (with the same energy per pulse) at reduced repetition rates through internal divide-down electronics.
5. Defined as the ratio between peak intensity of output pulse to peak intensity of any pre-pulse that occurs >1 ns before the output pulse.
6. Defined as the ratio between peak intensity of output pulse to peak intensity of any post-pulse that occurs >1 ns after the output pulse.
7. At constant temperature. Variable temperature specification <20 µrad/°C, peak-to-peak.
8. For wavelength extension through SHG, THG, FHG or OPA, please contact Spectra-Physics.
9. Performance specifications apply at peak of gain curve. Tuning range for <35 fs version: 795 - 805 nm.
10. The Solstice Ace is a Class IV – High-Power Laser, whose beam is, by definition, a safety and fire hazard. Take precautions to prevent exposure to direct and reflected beams. Diffuse as well as specular reflections can cause severe skin or eye damage.

Solstice Ace Beam Quality[1]
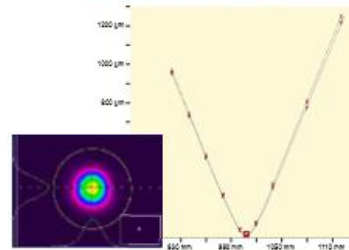
1. Typically measured performance.

Solstice Ace Dimensions

Left Side View

Rear View

Front View

Dimensions in Inch (cm)

B.3: Ocean Optics Flame S Spectrometer

Flame Technical Specifications

This document contains the technical specifications for the FLAME-S and FLAME-T. For more information on the Flame spectrometers, including installation, configurations, operation with OceanView, troubleshooting tips, and firmware protocol commands, please see the *Flame User Manual*. For more information on Ocean Optics products, please visit our website at www.oceanoptics.com.

Specifications Table

Specification	FLAME-S	FLAME-T
Optical and Spectroscopic		
Integration Time	1 ms – 65 seconds	3.8 ms to 10 seconds
Dynamic Range for single acquisition[1]	1300:1	
Dynamic Range of system[2]	2×10^8	3.4×10^8
Signal-to-Noise (single acquisition)	250:1	300:1
Resolution (FWHM)	0.1 – 10.0 nm (configuration dependent)	
Stray Light	<0.05% at 600 nm <0.10% at 435 nm	
Scan rate (max)[3]	400 Hz	260 Hz
Spectrometer Channels	One	
Thermal Stability	0.02 nm/°C for 650 nm range, 0.06 pixels/°C	
Triggering	4 modes	
Triggering Jitter	21 nanoseconds	
Detector		
Type	Sony ILX511B CCD	Toshiba TCD1304AP CCD
Detector range	190-1100 nm	
Pixels	2048 pixels	3648 pixels

101

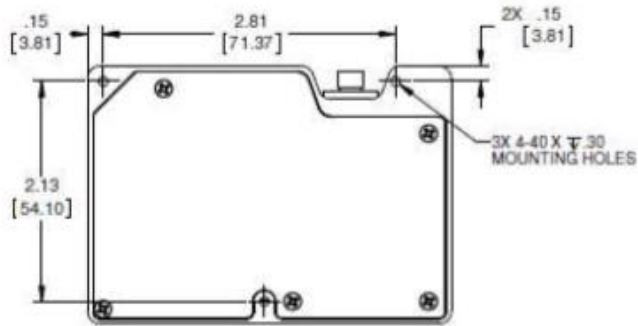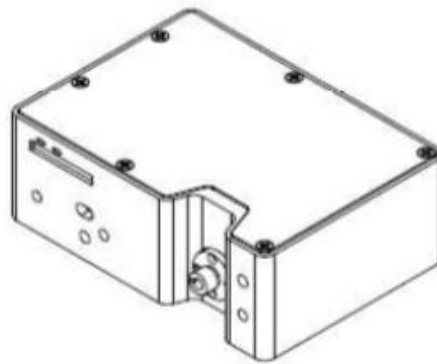| Specification	FLAME-S	FLAME-T
Pixel size	14 µm x 200 µm	8 µm x 200 µm
Electronic shutter	No	Yes
Pixel well depth	~62,500 electrons	~100,000 electrons
Readout noise (single dark spectrum)	50 counts RMS, 300 counts peak-to-peak	
Corrected linearity	>99.8%	
Filters (optional)	2nd and 3rd order rejection, long pass	
Electrical		
Power requirement (spectrometer functions)	250 mA at +5 VDC	
Supply voltage	4.75 – 5.25 V	
Power-up time	~2s	
Connectors	Micro-USB and JAE DD4 (DD4RA40JA1) 40-pin connector	
Micro-USB Absolute Maximum Ratings: V_{CC}	+ 5.5 VDC	
DD4 Absolute Maximum Ratings: V_{CC} (Pin 40) Voltage on any pin (other than input power)	+ 5.5 VDC +4VDC	
Interface: USB RS-232	USB 2.0, 480 Mbps 2-wire RS-232	
Mechanical		
Spectrometer Design	Asymmetric crossed Czerny-Turner	
Input Fiber Connector	SMA 905 or FC	
Gratings	15 different gratings	
Entrance Slit	5, 10, 25, 50, 100, or 200 µm slits. (Slits are optional. In the absence of a slit, the fiber acts as the entrance slit.)	
Physical Dimensions	88.9 mm x 63.5 mm x 31.9 mm	
Weight	265 g	

102

Specification	FLAME-S	FLAME-T
Environmental		

Temperature:
    Storage
    Operation
	-30° to +70° C
	0 to 50° C	

Humidity	0% - 90% noncondensing	
Compliance[4]		
Electrical	CE, FCC, CISPR 11:2010, EMC 2004/108/EC and EN 61326-1:2013	
Material	RoHS	
Shock	IEC 60068-2-64	
Vibration	IEC 60068-2-31	
Manufacturing	ISO:9001	

[1] Dynamic range for a single acquisition is a measure of the ratio of full signal to noise.

[2] Dynamic range of the system is the range of the detectable light level and can be thought of as the maximum detectable light level at the minimum integration time divided by the minimum detectable light level at the maximum integration time.

[3] Scan rate is dependent on the operating computer and not the spectrometer. These figures assume a non real-time operating system.

[4] Contact info@oceanoptics.com to obtain copies of certifications

Mechanical Diagram
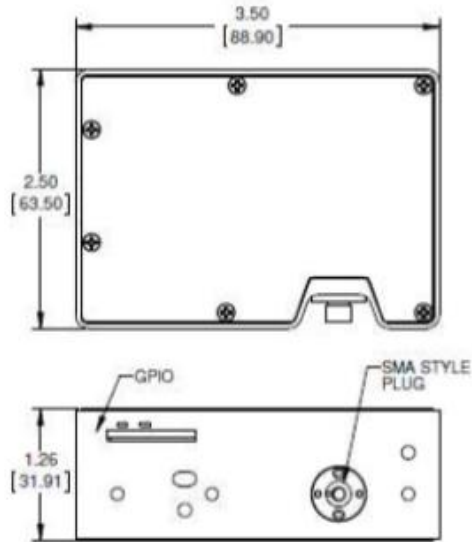
GENERAL NOTES:
(UNLESS NOTED OTHERWISE)

1. All dimensions subject to change without notice.

2. For STEP file see: 225-00000-00_CD.step

Flame Outer Dimensions

104

B.4: Princeton Instruments IsoPlane 320 Spectrometer

Princeton Instruments
SPECTROSCOPY GROUP

Specifications

	IsoPlane SCT 320
Focal length	320 mm
Aperture ratio	f/4.6
Usable wavelength range	190 nm to mid-IR with available mirror coatings, gratings, and detectors (to ~150 nm with optional purge capability)
CCD resolution (20 μm pixels)*	0.08 nm at all points on the focal plane
PMT resolution (10 μm slit)*	0.05 nm at all points on the focal plane
Stray light	$< 2 \times 10^{-5}$
Grating mount / size	Interchangeable triple-grating turrets with on-axis grating rotation: 68 x 68 mm gratings
Focal plane size	27 mm wide x 14 mm high
Astigmatism	Zero (0) at all wavelengths
Spatial resolution (MTF)	≥15 line pairs/mm @ 50% modulation, measured at focal plane center ≥ 8 line pairs/mm @ 50% modulation, measured over 27 x 8 mm focal plane
Slits	Entrance and Exit slits: - Standard manual (10 μm – 3 mm) - Optional motorized (10 μm – 3 mm and 10 μm – 12 mm versions) Kinematic entrance slit available for imaging and microspectroscopy.
Wavelength accuracy*	Mechanical: ± 0.2 nm | With IntelliCal: ± 0.01 nm
Wavelength repeatability*	Mechanical: ± 0.015 nm | With IntelliCal: ± 0.0015 nm
Drive step size*	0.002 nm
Size and weight	20.4" (518 mm) length x 17.7" (450 mm) width x 8.5" (216 mm) height 55 lbs (25 kg) weight
Optical axis height	5.0" to 5.875"
Computer interface	USB and RS232

* With 1200 groove/mm grating @ 435 nm
Specifications subject to change without notice.

Use the Grating Dispersion Calculator on our website:
www.princetoninstruments.com/spectroscopy/calculator/ for information on IsoPlane 320 performance with various gratings and Princeton Instruments cameras.

B.5: Princeton Instruments PI MAX 4 ICCD

Princeton Instruments
IMAGING GROUP

SPECIFICATIONS

CCD

Image sensor	Kodak KAI-1003 scientific grade interline CCD
CCD format	1024 x 1024 imaging pixels; 12.8 x 12.8 μm pixels; 13.1 x 13.1 (18.5 mm diagonal)
System read noise (typical) @ 4 MHz digitization @ 16 MHz digitization @ 32 MHz digitization	 16 e- rms 40 e- rms 70 e- rms
Pixel full well	130 ke-
Dark current @ -25° C (typical)	< 2 e-/p/sec
CCD temperature @ + 23° C room temperature @ + 20° C ambient	 -20° C (Air), -30° C (Liquid assist), Guaranteed -25° C (Air), -35° C (Liquid assist)
Vertical shift rate	2.5 μs/row (variable via software)

INTENSIFIER

Intensifiers available	18 mm - Gen II, Gen III filmless (Contact Princeton Instruments for 25 mm intensifiers)						
Method of coupling to the CCD	1:1 fiber optic						
Intensifier type	Gen II				Gen III *Filmless*		
	UV	SB	RB	SR	HBf	HQf	HRf
Wavelength range	See QE curves, pages 4 & 5						
Min. Gate Width (Optical FWHM)* Picosecond Gate Fast Gate Slow Gate	< 500 ps (for Fast Gate tubes only) ~ 2 ns (typical), 3 ns (guaranteed) For SB only: < 200 ns, < 8 ns (w/MCP gating)				< 500 ps (for Fast Gate tubes only) ~ 2 nsec (typical), 3 nsec (guaranteed) -NA-		
DIF mode inter frame time	450 ns (min); P46 phosphor decay time - 500ns (to 10%), 2 μsec (to 1%)						
Repetition rate: Sustained	1 MHz; 100 kHz with Picosecond gating; 8 kHz with MCP gating; 6.25 kHz with MCP bracket pulsing						
Resolution limit	40 to 64 lp/mm				57 to 64 lp/mm		
Equivalent Background Illumination (EBI) Photo e-/pixel/sec @ room temp (with photocathode cooling)	0.05 - 0.2 (0.005 - 0.02)				0.02 (0.002)		
Phosphor	P43 (P46, P47 optional)						
Operating environment	+5° C to +30° C non-condensing						
Storage environment	-25° C to +55° C						
Certification	CE						

* Measured with 18 mm intensifier. Contact your local sales representative for more information.
All specifications subject to change.

FRAME RATES

Binning	1024 x 1024	512 x 512	256 x 256
1 x 1	26	48	85
2 x 2	56	90	140
4 x 4	95	142	199

NOTE: Frames per second at 32MHz

Page 2 of 8
PI-MAX4:1024i   Rev. N3

106